The University of Tokushima
Dissertation for Doctoral Degree

Theoretical and Application Researches on Gas Breakdown and Spark Evolution by Laser Irradiation

Applicant: Xiaobo Zhang

Supervisor: Prof. Yoshihiro Deguchi

Discipline: Mechanical Engineering

Category: Engineering

June 2014

Theoretical and Application Researches on Gas Breakdown and Spark Evolution by Laser Irradiation

Xiaobo Zhang

A THESIS SUBMITTED
FOR THE DEGREE OF DOCTOR OF ENGINEERING
GRADUATE SCHOOL OF ADVANCED TECHNOLOGY AND SCIENCE
THE UNIVERSITY OF TOKUSHIMA

June 2014

ABSTRACT

Laser-induced gas plasma has gained substantial interest during the past decade due to its potential industrial applications, such as laser-induced breakdown spectroscopy, laser ignition, laser propulsion, etc. This thesis is mainly concerned the simulation of laser energy deposition, the resultant fluid dynamic evolution in gas by the energy spot as well as gas plasma used in laser-induced breakdown spectroscopy technology for element trace.

Chapter 1 states the brief introduction to laser-induced gas plasma as well as its related industrial application technologies. The previous numerical and experimental researches are also summarized to show the purpose of study in this thesis.

Chapter 2 theoretically describes processes of plasma generation by laser irradiation as well as the resultant hydrodynamic evolution: initial release of feed electrons by multiphoton ionization, ionization of gas in the focal region of the laser beam by cascade ionization, absorption of laser energy by gaseous plasma, rapid expansion of the plasma and detonation formation within laser pulse, and the propagation of pressure wave into the surrounding gas after laser pulse.

In chapter 3, propagation of pressure wave caused by laser energy disposition in argon are numerical studied. A model about Nd:YAG laser energy deposition in argon has been developed for this purpose. It is designed to predict the fluid dynamic effects of the energy deposition process in quiescent argon. The key physical processes are captured, including evolution of energy spot shape and structure, ionization and recombination chemical reactions, evolution of the pressure wave front and the subsequent fluid movement.

To simulate the propagation of the laser beam in time, the Maxwell equations and the finite difference time domain method are adopted. The discretization process of Maxwell equations, disposal of boundary conditions and the incident wave in FDTD are discussed in detailed in chapter 4. At last the Gaussian beam, which is usually used for a specified form of the laser beam, is simulated by FDTD.

In chapter 5, the gas kinetic theory and the continuous Boltzmann equation are firstly introduced. To solve the continuous Boltzmann equation, the lattice Boltzmann method (LBM) is adopted. The build-up processes of D2Q9 as well as the universal numerical procedure of LBM are discussed in detailed. After the background knowledge, gas plasma produced by laser irradiation is modeled by Boltzmann equations.

In chapter 6, interaction of laser and existing plasma as well as generation of gas plasma by laser irradiation is simulated by a hybrid model. Maxwell equations, which are used to model the propagation of laser, are calculated by the finite difference time domain method. Employing coefficients of distribution functions, processes of multiphoton ionization, electron impact ionization and three-body recombination are included in Boltzmann equations. Using D2Q9 model

in LBM, number densities of particles in plasma can be obtained after solving Boltzmann equations. For the energy transformation in plasma, the finite volume method is applied to calculate the macroscopic energy equations directly coming from the continuous Boltzmann equations.

As one important application of gas plasma produced by laser irradiation, laser-induced breakdown spectroscopy technology for iodine detection is studied in chapter 7. Iodine in buffer gases of N_2 and air was detected using nanosecond and picosecond breakdowns of CH_3I at reduced pressure. The measurement results of iodine demonstrated that low-pressure LIBS is the favorable method for trace species measurement in analytical application. The plasma generation process can be controlled by the gas pressure and laser pulse width for the larger ionization and excitation processes of iodine, which is discussed by the intensity ratio of iodine emission at 183 nm to nitrogen emission at 174.3 nm. The detection limit of iodine measurement in N_2 was 60 ppb in nanosecond breakdown at 700 Pa. Iodine in the buffer gas of air was also detected using nanosecond and picosecond breakdowns to discuss the effect of oxygen.

Chapter 8 is the summary and conclusion of this thesis as well as some suggestions for future research.

CONTENTS

LIST OF SYMBOLS

ABCs	Absorbing boundary conditions
BGK	Bhatnagar-gross-krook
$\boldsymbol{B}$	Magnetic induction intensity (T)
CCD	Charge-coupled device
$C_{\alpha,\mathrm{p}}$	Specific heat of species α at constant pressure ($\mathrm{J\cdot mol^{-1}\cdot K^{-1}}$)
D_α	Diffusivity of species α ($\mathrm{m^2\cdot s^{-1}}$)
$\boldsymbol{E}$	Electric field intensity ($\mathrm{V\cdot m^{-1}}$)
E_α	Molar mass of species α ($\mathrm{J\cdot mol^{-1}}$)
E_α^{ele}	Molar electronic energy of species α ($\mathrm{J\cdot mol^{-1}}$)
$E_\alpha^{\mathrm{trans}}$	Molar translational energy of species α ($\mathrm{J\cdot mol^{-1}}$)
FDTD	Finite difference time domain
FVM	Finite volume method
FWHM	Full width half maximum
F_α	External force in the direction of α (N)
$\boldsymbol{F}_\alpha$	Total force of species α (N)
H	Total enthalpy ($\mathrm{J\cdot kg^{-1}}$)
$\boldsymbol{H}$	Magnetic field intensity($\mathrm{A\cdot m^{-1}}$)
I	Laser intensity ($\mathrm{W\cdot m^{-2}}$)
ICCD	Intensified charge-coupled device
I_α	Total emission intensity of species α ($\mathrm{J\cdot s^{-1}}$)
I_j	Molar ionization potential ($\mathrm{J\cdot mol^{-1}}$)
$\boldsymbol{J}$	Current density ($\mathrm{A\cdot m^{-2}}$)
$J_{\alpha j}$	Diffusion flux of species α in the direction of j ($\mathrm{kg\cdot m^{-2}\cdot s^{-1}}$)
$K_{\alpha,\mathrm{j}}$	Statistic weight
LBM	Lattice Boltzmann method
LIBS	Laser-induced breakdown spectroscopy
LTE	Local thermodynamic equilibrium
MPI	Electron impact ionization
M_α	Molecular weight of species α ($\mathrm{kg\cdot mol^{-1}}$)
N	Number of needed photons of multiphoton ionization
N_A	Avogadro's number, $N_\mathrm{A} = 6.022\times10^{-23}$ $\mathrm{mol^{-1}}$;
N_rec	Number of three-body recombination ($\mathrm{m^{-3}}$)
PML	Perfectly matched layer
R	Gas constant ($\mathrm{J\cdot mol^{-1}\cdot K^{-1}}$)
R_g	Gas constant ($\mathrm{J\cdot kg^{-1}\cdot K^{-1}}$)

$R_{\alpha,\mathrm{m}}$	Mass production rate of species α ($\mathrm{kg\cdot m^{-3}\cdot s^{-1}}$)
$R_{\alpha,\mathrm{f}}$	Change rate of the distribution function ($\mathrm{s^{-1}}$)
$\hat{R}_{\alpha,\mathrm{r}}$	Molar production rate of species α in reaction r ($\mathrm{mol\cdot m^{-3}\cdot s^{-1}}$)
Sc	Schmitt number
S_{h}	Energy source term ($\mathrm{J\cdot m^{-3}\cdot s^{-1}}$)
S_{m}	Mass source term ($\mathrm{kg\cdot m^{-3}\cdot s^{-1}}$)
T	Temperature (K)
W_{MPI}	Rate of multiphoton ionization ($\mathrm{m^{-3}\cdot s^{-1}}$)
Y_{α}	Mass fraction of species α
$\boldsymbol{a}$	Accelerator ($\mathrm{m\cdot s^{-2}}$)
c	Lattice velocity in the lattice Boltzmann method ($\mathrm{m\cdot s^{-1}}$)
c_{α}	Thermal velocity of species α ($\mathrm{m\cdot s^{-1}}$)
c_0	Sound speed ($\mathrm{m\cdot s^{-1}}$)
$\boldsymbol{e}_{\alpha}$	The discrete velocity in the direction of α ($\mathrm{m\cdot s^{-1}}$)
f_a	The distribution function of species α
f_{α}^{eq}	The equilibrium distribution function of species α
$g_{\alpha,\mathrm{j}}$	Statistic weight
h	Plank's constant, $h = 6.626\times10^{-34}$ J·s ; static enthalpy ($\mathrm{J\cdot kg^{-1}}$)
h_{α}	Static enthalpy of species α ($\mathrm{J\cdot kg^{-1}}$)
h_{α}^{0}	Production enthalpy of species α ($\mathrm{J\cdot mol^{-1}}$)
k_{B}	Boltzmann's constant, $k = 1.381\times10^{-23}$ $\mathrm{J\cdot K^{-1}}$
k_{r}	Rate of reaction γ ($\mathrm{m^3\cdot mol^{-1}\cdot s^{-1}}$ or $\mathrm{m^6\cdot mol^{-2}\cdot s^{-1}}$)
m_{α}	Molecular weight of species α (kg)
n_{α}	Number density of species α ($\mathrm{m^{-3}}$)
$\boldsymbol{q}_{\alpha}$	Heat flux of species α ($\mathrm{J\cdot m^{-2}\cdot s^{-1}}$)
$\boldsymbol{r}$	Location vector
$\boldsymbol{u}_a$	Velocity of species α ($\mathrm{m\cdot s^{-1}}$)
$\boldsymbol{v}$	Particle microscopic velocity ($\mathrm{m\cdot s^{-1}}$)
$\langle v_{\alpha} \rangle$	The average thermal speed of species α ($\mathrm{m\cdot s^{-1}}$)
Θ	Enabled temperature of reactions (K)
ε	Permittivity ($\mathrm{F\cdot m^{-1}}$)
ε_{α}	Total energy of species α ($\mathrm{J\cdot m^{-3}}$)
$\varepsilon_{\alpha,\mathrm{j}}$	Energy at the electronic level j of species α (J)
$\varepsilon_{\mathrm{ion}}$	Ionization potential (J)
θ	Lattice sound speed in the lattice Boltzmann method ($\mathrm{m\cdot s^{-1}}$)
κ	Conductivity ($\mathrm{W\cdot m^{-1}\cdot K^{-1}}$)

λ	Laser wavelength (nm)
μ	Permeability ($H \cdot m^{-1}$)
v	Laser frequency(Hz)
ρ	Mass density ($kg \cdot m^{-3}$); charge density ($C \cdot m^{-3}$)
σ_{ec}	Cross section of electron impact ionization (m^2)
σ_{MPI}	Absorption cross section of photons (m^2)
τ	Relaxation time of particle collision (s)
τ_{ij}	Stress tensor (Pa)
$\tilde{\tau}$	Dimensionless collision time

CHAPTER 1. PREFACE

1.1 Background and Significance of Study

When laser is focused onto surfaces of solid/liquid or into gas, part of laser energy is reflected, part of laser energy is penetrated and part of laser energy is absorbed. The absorbed laser energy is transferred or transformed by excitation or vibration of electrons and atoms. In these processes, there are physical, chemical or biological effects occurred in the medium. If these effects are controlled well, they can derive many new industrial application technologies. Study of these processes is called laser matter interaction.

Currently physical, chemical and biological effects of laser matter interaction have already been used in many technologies, such as laser hardening, laser alloy, laser remelting, laser cladding, laser cutting, laser welding, laser propulsion, laser spectroscopy, laser ignition, laser operation, etc. Generally the relationship of laser intensity and corresponding applications can be summarized as Table 1.

Table 1 Relationship between laser intensity and corresponding applications.

Laser intensity ($W \cdot cm^{-2}$)	$10^3 \sim 10^4$	$10^4 \sim 10^6$	$10^6 \sim 10^8$	$> 10^8$
Effects	phase transition	molten	gasification	plasma
Applications	laser hardening	laser welding, laser re-melting	laser cutting, laser punching	laser cladding, laser propulsion

Among these effects and application technologies of laser matter interaction, this research mainly concerns interaction of laser and plasma produced by gas breakdown. When a laser beam with enough high intensity is focused into gas, the atoms/molecules may be ionized forming plasma. Supported by laser energy, plasma temperature increases sharply. Degree of ionization and absorption of laser energy by plasma mutually reinforce, and a laser-supported absorption wave is generated facing the laser beam by thermal conducting and radiation hydrodynamics. If these can be controlled well, their mechanical effects can be used for ignition, propulsion, fusion, analytical chemistry as well as supersonic and hypersonic flow control.

1.1.1. Process of interaction between laser and gas

Absorption of laser energy by medium derives from interaction of the monochromatic electromagnetic fields and internal charges and oscillators of medium. For solids and liquids, their

internal molecules have strong action each other. The absorption spectroscopy consists of several consecutive frequency bands. While for atomic gas, its absorption spectroscopy is just several lines corresponding to resonance frequencies of oscillators in atoms. For molecular gas, there are few absorption frequency bands.

Rotation of irreducible atoms in molecules form the rotational spectra line, it locates in the far-infrared region and is about greater than 25 μm. The mutual vibration frequencies of atoms in molecules are larger than rotation frequencies, so the vibration absorption line exists near to 1 μm. Furthermore, electrons can have transitions within the structure of the molecular bond. And the corresponding absorption line locates in ultraviolet region and is about 0.1 μm. According to the above wavelength magnitudes, the absorption spectrum of electrons can embody rotation and vibration spectrums. When pressure or density of gas increases, the interaction of atoms and molecules become strengthener, so there are wider absorption bands.

When the medium is in the plasma state, the free electrons can absorb laser energy in abundance by collision with atoms and ions, which is called inverse bremsstrahlung absorption. In this process, Degree of ionization and absorption of laser energy by plasma mutually reinforce. However if the plasma oscillator frequency is almost equal to laser frequency, laser beam cannot propagate into the plasma any more. Because the oscillator frequency is positively correlated with electron density of the plasma, the electron density corresponding to laser frequency is called as critical electron density.

To the research purposes of this dissertation, if the mechanical effects can be adopted for industrial applications, some conditions are necessary. Firstly the laser intensity is enough high so that gas molecules/atoms can be ionized forming plasma. Secondly plasma can get laser energy further for enough temperature and pressure growth so that shock wave can be produced within plasma expansion process.

For the pulsed laser beam, if the photon density in the focus zone is enough high, one gas atom/molecule can simultaneously absorb a number of photons. If the absorbed energy is higher than the ionization potential, the gas atom/molecule is ionized which is called multiphoton ionization (MPI) and is the mean of generation of the originally free electrons of plasma. The electrons then can absorb more photons via the inverse bremsstrahlung process. If the electrons gain sufficient energy, they ionized other gas atoms/molecules on impact, leading to an electron cascade and breakdown of the gas forming plasma. Gas breakdown by laser irradiation can be easily found by flash as well as sharp acoustic sound. Once plasma is produced, it can absorb laser energy intensively. The absorbed laser energy is transformed as internal kinetic energy of plasma, and part of plasma energy is transferred to gas atoms/molecules by heat radiation. At last absorption process of laser energy by plasma is coupled with movements of plasma and adjacent neutral gas. All these processes about gas and plasma heated and accelerated by laser energy is

generally called laser-supported absorption wave. In the generation of this wave, the following three mechanisms are critical.

The breakdown firstly happens in the focus spot of laser beam. While with the long relaxation time and being proportion to distance to focus spot, ionization causing breakdown can also happen within a certain distance from the focus spot to laser source. With laser energy absorbed by charged particles, the ionization degree can increase gradually so that plasma near the focus spot can completely get all laser energy. Conversely gas behind the plasma cannot get any energy. Combination of these two trends, the overall effect is that there is a “breakdown wave” moving from the laser spot to laser source in interaction between laser and gas/plasma.

When plasma gets energy from the laser system, an absorption region with high temperature and high pressure is produced. Because of the pressure gradient plasma in absorption zone expands outward forming a shock wave. Due to strong compression of the shock wave, the ambient gas with high temperature can be ionized. Furthermore the charged particles produced by compression near to laser beam can get laser energy so that they can make new ionization. When the ionization rate gradually comes to certain degree, gas in the compressed region is becoming more and more opaque to laser beam. At last the compressed gas region is converted to a new plasma absorption zone. These replacement and movement processes due to the shock wave are called laser-supported shock wave.

The plasma absorption zone produced firstly in the focus spot can have high temperature of tens of thousands degrees, so it can have radiation emission heating the ambient gas. The radiation can have the same effects of compression to gas ionization causing new plasma absorption zone formation and movement. This process is called radiation heating mechanism.

“Breakdown wave”, laser-supported shock wave and radiation heating mechanism usually work together in interaction between laser and gas. Usually laser-supported shock wave and radiation heating mechanism play a leading role for laser beam with moderate intensity and “breakdown wave” is the leading mechanism for interaction between gas and laser beam with high intensity.

1.1.2. Industrial applications of laser-induced gas plasma

Industrial application of laser-induced gas breakdown producing plasma can be classified into three categories. One is its thermal-mechanical effect used for propulsion or ignition of combustible mixture. The second one is in spectral measurement technology. The atomized species in plasma can release light of the corresponding wavelengths for composition analysis. Gas spark can be also used as source for X-ray generation, while which is not the considered topic in this dissertation.

1) Laser propulsion

Laser propulsion [1-3] is a form of beam-powered propulsion where the energy source is remote

laser system and separate from the reaction mass. This form of propulsion system differs from the conventional chemical rocket where both energy and reaction mass come from the solid or liquid propellants carried on board the vehicle. When the air is used as propellant for laser propulsion, the vehicle is usually called as light-craft. By leaving the vehicle's power source on the ground and by using ambient atmosphere as reaction mass for much of its ascent, a light-craft could potentially be capable of delivering a very large percentage of its launch mass to orbit. In light-craft, as shown as Fig. 1.1, the laser shines on a parabolic reflector on the underside of the vehicle that concentrates the light to produce a region of extremely high temperature. The air in this region becomes heated and expands violently in a laser-supported detonation, producing thrust. Beside of the larger percentage launch mass to orbit, laser propulsion vehicles would be safer than chemical rockets since they can't explode and don't drop off pieces as they fly.

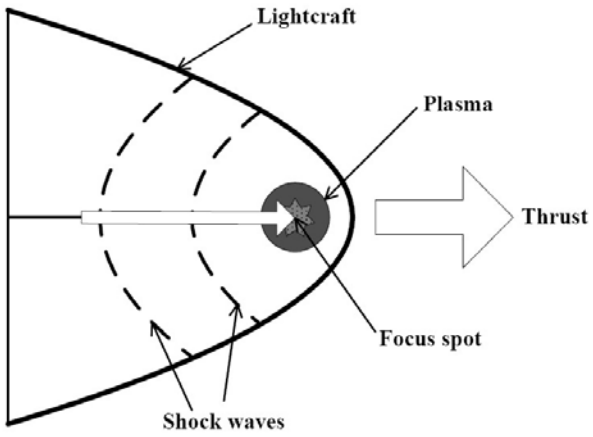

Fig. 1.1 Light-craft by laser propulsion.

2) Supersonic and hypersonic flow control

For objects flying at transonic or supersonic speed, laser energy deposition can be used for wave drag reduction as a mean of energy additions for modification of external flow field around a vehicle. Given an appropriate position, shape, and power of thermal source relative to external surface of the body, one can substantially decrease its aerodynamic drag and thereby reduced the value of the thrust required to maintain the steady flight [4, 5].

3) Laser spark ignition

Another important application of laser-induced gas breakdown is for combustible gas mixtures ignition [6], named laser-induced gas spark ignition. When laser is used for reactive mixtures ignition, the mechanism can be divided into four categories: laser thermal ignition, laser-induced photochemical ignition, laser-induced resonant breakdown ignition as well as laser-induced gas

spark ignition. In laser thermal ignition, the kinetic energy of target molecules in translational, rotational and vibrational form increases, then the molecular bond is broken and chemical ignition. Because laser thermal ignition needs a combustible mixture with strong absorption ability at the laser wavelength, it is usually adopted for igniting solids. In laser-induced photochemical ignition, firstly laser photons dissociate the target molecules into highly reactive radical species. If the production rates of radicals are greater than their recombination rates, they can initiate the usual chemical chain-branching reaction leading to ignition and full scale combustion. Obviously a close match between the laser wavelength and target molecules' absorption wavelength is indispensable in order for dissociation to occur. Photochemical ignition process is most effective at ultraviolet wavelength because the photon energy of visible and infrared laser systems is smaller than the dissociation energy of most gases. However ultraviolet lasers are very expensive. To ensure a sufficient amount of reactive radicals (10^{17} atoms/cm^3) within a sufficiently large volume, laser-induced photochemical ignition can be used to ignite mixtures at lower pressure and closer to the flammability limits. Laser-induced resonant breakdown ignition involves, firstly, a non-resonant multiphoton dissociation of molecules resulting to freed atoms, followed by a resonant photoionization of these atoms. This process generates sufficient seed electrons which can then readily absorb more energy by inverse bremsstrahlung effect leading to formation to plasmas leading to ignition. Theoretically, less input energy is required due to the resonant nature of this method. However the requisition of the specific wavelength laser system for dissociation and resonant breakdown limits the applicable occasions.

Laser-induced gas spark ignition begins with multiphoton ionization of few gas molecules which releases electrons that readily absorb more photons via the inverse bremsstrahlung process to increase their kinetic energy. Electrons liberated by this means collide with other molecules and ionize them, leading to an electron avalanche, and breakdown the gas. Multiphoton absorption processes are usually essential for the initial stage of breakdown. Spark produced this way is apparently a source of highly reactive chemical intermediates at a very high temperature and pressure. This spark emits light, heat, and shock wave to the surrounding medium. If the spark is intense enough, then the resultant ignition kernel is sufficiently strong to permit transition into full scale combustion. Using this approach, although this approach utilizes large amount of the laser energy, many benefits provided by the laser ignition have to compromise. Since the cavity is fixed and it is located at the wall, wall interaction is not eliminated, ignition location is not movable. Wall ignition is not favorable for large engines because the time for complete combustion is long. Fixed ignition location is not favorable for situations where mixture is not uniform. In this case, movable ignition location is preferred. In order to have center ignition, this technique requires higher laser energy to create gas breakdown. Higher laser energy leads to difficulty in laser deliver system.

4) Laser-induced breakdown spectroscopy

Laser-induced breakdown spark can be used for a light source for optical measurement technology named laser-induced breakdown spectroscopy (LIBS) [7]. When a laser beam is focused onto a small area, a hot spark is produced by multiphoton ionization and inverse bremsstrahlung absorption of laser energy. In the spark, materials are atomized and light is emitted corresponding to unique wavelengths for different elements. After the released light is collected and analyzed by spectrometer, chemical compositions of the materials can be obtained. Because of the remarkable features, such as high sensitivity, in-situ measurement capability and reliability for long time running, LIBS can be used for element analyzer and monitoring and controlling systems in fields of combustion, material processing as well as toxics inspection.

Besides, laser-induced sparks can be used as a source for producing high-intensity x-rays and extreme ultra-violet radiation in rare gases [8]. For these applications, laser-induced gas breakdown as well as spark evolution is the elemental process. While because of several geometric and time scales transition, the study on it is rich in challenge.

1.2 Overview of Experimental Studies on Laser-induced Gas Breakdown and Spark Evolution

For experimental study about laser-induced gas plasma, one laser beam is firstly is focused into simple gas, stoichiometric mixed gas or air. After the gas is breakdown producing plasma, Transient observation instruments are used to observe and record related phenomena. After analysis, some results about plasma generation, evolution as well as related industrial applications can be obtained.

Laser system used in experimental study can be divided into two classes. One is nanosecond pulsed laser, such as Nd:YAG solid-state laser. Such laser system has high intensity, and it can make gas breakdown producing plasma. But the total energy is low of one pulse, and the plasma generation and evolution processes are very transient. The other one is laser system with microsecond pulse length, such as CO_2 laser. The single pulse energy of this kind of laser is much more and plasma induced by its irradiation is relatively stable.

Instruments adopted in gas plasma are usually high speed camera, schlieren photograph, CCD (charge coupled device)/ICCD (intensified CCD) as well as optical pyrometer. The primary work is phenomena known research. In this kind of work, the plasma is photographed in major range of experimental setup. Plasma generation mechanism, expansion and evolution velocities can be known after analysis. The second kind of experimental work is about flow field record using high speed schlieren photograph technology. Here shapes, specific size of the plasma core as well as their variation are obtained. With development of fine and high-speed measurement technologies, the plasma temperature and related particle number density can be measured.

In 1972, using high-speed camera, Pirri [9] studied the plasma and detonation formation above a metallic surface with a high-power CO_2 laser. The detonation was produced within dozens of nanoseconds. An existing plasma front could absorbed most energy of laser beam and it moved to laser system supersonically. In 1994 Song [10] observed propagation of laser-supported detonation with CCD camera. The wave was able to move forward laser system with speed of 3.57×10^5 m/s in ambient air and this velocity have some relationship with surrounding gas density.

In 21st century, the phenomena research of laser-induced gas plasma generation and evolution are much more active. In 2000, Harilal [11] investigated air spark at atmospheric pressure by the frequency doubled Nd:YAG laser using fast photography. Two dimensional time-resolved spontaneous views of spark from 1 to 5500 ns were made by ICCD camera system. The plasma is firstly produced near the focus spot and expands spherically at internal times. But with absorbing more laser energy, the plasma grows more in the axial direction (laser propagation direction) than in the lateral direction. From images the estimated velocities of the plasma in the initial stages are 1.1×10^7 cm/s in the axial direction and 5×10^6 cm/s in the lateral direction. At time greater 10ns after breakdown, the dimension of the spark appears to be constant. However a complex feature begins to form in the time evolution frame. The surrounding gas moves inward toward the center of the hot spark, so a dumbbell shaped spark appears along the laser propagation direction. For the same laser system, the focal spot size and Rayleigh range increase as focal length increases. If the incident laser energy is higher than breakdown threshold the plasma can be produced at location before the pulse reaches the focal point. And spark can extend over a large volume towards the focusing lens. This backward movement of plasma kernel resulting from the building of a laser-supported radiation wave that travels against the laser beam. In the opposite side, plasma is screened by the front plasma and relaxes through de-excitation of ionized species. For incident laser beams of different energy levels, centers of the plasmas move along the axial. At low energies the kernel is located at the focus spot itself. But as laser energy increases the kernel move backwards. The higher the incident energy, the farther the initial plasma moves away from the focus spot.

Bindhu and Harilal [12, 13] studied laser propagation and energy absorption by argon and air spark at different pressures. The argon spark at low pressures (<100 Torr) has a nearly cylindrical shape. The spark is confined to the focal volume and there is less of an absorption front propagating towards the focusing lens. This indicates that multiphoton ionization is domain rather than the cascade-like process for spark evolution at high pressures. At high pressures, spark absorption of laser energy states immediately after breakdown and more than 50% of the laser energy is absorbed. This significant energy absorption by the plasma indicates that inverse bremsstrahlung is important in the subsequent heating and ionization of plasma. At low pressures, the spark has no backward movement. So the spark only absorbs a little laser energy. With laser energy increases above

breakdown threshold, the size of spark increase rather than its temperature and density because of spark absorption. Comparison of transmitted laser energy after sparks shows that the absorption depth is higher for argon than for air.

Using Rayleigh scattering and time-resolved emission spectroscopy, Huwel, Nassif and Longenecker [14, 15] recorded the spatial and temporal evolution of laser-generated argon and nitrogen sparks during the first tens of nanoseconds to complete dissipation. For argon spark, its shape transforms from reverse-dumbbell to an elongated ellipsoid around 5μs to an oblate shape after approximately 10μs and to a toroidal shape after approximately 20-40μs. The basic mechanism of toroidal shape of spark is the counter-propagating vortexes along the laser propagation direction. Within laser pulse, the shock wave caused by the rapid energy deposition quickly travels into the surrounding gas. At the spark center, it leaves behind an over-expanded region of lower pressure, relative to the ambient gas, into which two opposing gas flows penetrate—coming from the surrounding region along the axis of the spark laser. These counter-propagating, colliding gas flows create a pair of cylindrically symmetric vortices, which then act in concert to move the hot gas remnants radially outward and into a toroidal shape. Using LIBS technology, Glumac [16] obtained the spatial and temporal evolution of laser spark in air with 20 ns to 1 ms. The results about spark generation, movement as well as its shape evolution are similar with other scholars'. Chen [17] paid her attention to laser-induced spark adopted to ignition application. The results provided an understanding of the plasma kernel dynamics and the flame development of NH_3/O_2 mixture.

Measurement of plasma temperature and number density is vital to further understanding of laser-plasma interaction. In 1975, a perk temperature of 17000 K was found in center of air plasma by a continuously operating CO_2 laser by Keefer [18]. In 1998, Yalcin [19] used LIBS technology to measure plasma, electron number density as well as their evolution with time in scale of microsecond. The plasma temperature of N_2 plasma temperature at 0.35 and 1.4μs under atmosphere pressure were 21400 and 14900 K. electron number densities are 1.2×10^{18} and 1.9×10^{17} cm^{-3} respectively at 0.35 and 1.4μs. Using Rayleigh scatter, Nassif, Huwel and Longencker [14, 15] got two dimensional temperature distribution of N_2 spark core from 10 to 500 μs. At a delay time of 30 μs, the laser plasma remnant appears as a nearly spherically symmetric region with a center temperature of about 4500 K. After around 100 μs, the hot gas starts to change into a toroidal shape at about 2000 K. After approximately 5ms from breakdown, N_2 spark is cooled to ambient temperature.

Glumac [16] had measured evolution of air spark for longer time. For early times, between 50 ns and 1μs, images of the spark emission had been obtained to characterize the geometry. Also the temperature and electron number density were measured from the emission spectra between 490 and 520 nm where 46 N II lines are observed. The methodology of fitting the experimental data to

the modeled spectra to deduce the temperature and electron number density is described. For the initial temporal range, the temperature peaks at approximately 50,000 K and decays over the first 1 μs. The electron number density peaks at approximately 10^{19} cm^{-3}, decaying only slightly slower than t^{-1}. For the longer temporal evolution, from 20 to 1000 μs, planar temperature measurements were achieved using filtered Rayleigh scattering. The peak temperature starts at approximately 4100 K at 20 μs and decays to 580 K by 1 ms.

Bindhu and Harilal [12, 20] had measured the electron density and the temperature as functions of the axial distance from the focal point, the time from 50ns to 600ns after the onset of spark formation, and the laser energy. An initial electron temperature of 35,000 K and a density of 1×10^{19} cm^{-3} were observed at 2mm separation from the focal point and toward the focusing lens. The density diminishes rapidly with time and then levels off at later times. The electron temperature also drops with time but at a much slower rate than the density.

Joshi [21] presented time-resolved spectroscopic measurements of 1064-nm Nd:YAG laser-produced plasmas in air at pressures from 0.85 to 48.3 bar.

Beside the above work, some researchers paid their attention on critical parameters measurement. When laser beam is focused into gas medium, the breakdown can happen only when laser intensity is bigger than some critical value. The minimum intensity for breakdown is called breakdown threshold. Within laser pulse, plasma produced by breakdown absorb laser energy form laser-supported detonation wave (LSDW). In propagation of LSDW, its wave front is advancing with plasma supported by laser energy. When laser intensity drops to some levels, the wave front cannot get laser energy any longer. LSDW decays to laser-supported combustion wave. Usually the minimum intensity for LSDW propagation is called propagation threshold of LSDW. Breakdown threshold is much higher than propagation threshold of LSDW. In 1970, Smith [22] measured that the breakdown threshold of air by CO_2 laser was 10^9 W/cm^2. And the breakdown threshold increases with increase of laser frequency and drop of gas pressure. Takahashi [23] found breakdown threshold decreases when a solid target plate is placed near the focus spot. Zvorykin [24] investigated needed conditions for LSDW using laser systems with frequencies of 0.25, 5.6 and 10.6 μs respectively. The condition that width of plasma absorption core is smaller than one fifth of diameter of laser beam was found as necessary for LSDW propagation. And intensity of laser beam necessary for LSDW had relationship with gas pressure. Mori [25] had found the effect of laser focusing system to propagation threshold of LSDW. In quiet air LSDW was able to survival for 2.5 μs and plasma would separate with LSDW at approximately 3 μs.

From the above review, we know that the preliminary work is most plasma phenomena evolution, temperature and particle number density measurements after laser pulse. Research about laser-gas, laser-plasma interactions and laser-supported combustion/detonation/radiation wave propagations is very few. Such contents are really challenged now days because response speeds of measurement

instruments.

1.3 Overview of Numerical Work on Laser-induced Gas Breakdown and Spark Evolution

Physical processes in nature often cover several geometric and time scales. The about diameter of atoms is about 10^{-10} m. In the daily life, the size of concerned material is often in meter-scale. While in solar system, diameter of common planets can achieve to 10^{10} m. From atoms to planets, there is a 40-order of magnitude. Collisions among atoms can accomplish in 10^{-15} s, while time scale used for description of planet movements are 10^{15} s. Fig. 1.2 shows scale ranges of physical processes in science and engineering [26].

Numerical approaches for above physical processes can be divided into macroscopic, mesoscopic and microscopic levels. Fig. 1.3 collects the theory based, selection dependence and active methods of each level approach [26]. In the past decade, numerical methods in single scale have achieved great improvements. Ansys, CFX and Fluent depending on finite element/volume method can be used for spaceship, plane and submersible design. The lattice Boltzmann method (LBM) and discrete simulation of Monte Carlo method are mesoscopic methods. They adopt a concept of computational particles which are much larger than an actual molecule but act as a molecule (simulation molecule). Now they can be used for two or three dimensional fluid flow with chemical reactions within complex geometric domain [27, 28]. In microscopic approaches, such as molecule dynamics, every molecule is simulated according to the Newton's law of motion without any phenomenological description [29].

Different numerical methods have their own limitations. The major limitation of the macro-type numerical approach (the finite difference/volume/element methods) is the complete neglect of microscopic mechanism and hence the introduction of some empirical or ad hoc assumptions. On the other hand, the meso-scale or micro-scale methods, even though can reveal the details of a complex meso-scale or micro-scale process, they usually require enormous computer memory and computational times. Hence the size of their computational domain is heavily restricted.

Process of laser energy deposition in gas can be described by the following progressive events: initial release of electrons by multiphoton ionization, ionization of gas in the laser focal region by cascade release of electrons, absorption of laser energy by the gaseous plasma, rapid expansion of the plasma and laser-supported detonation wave formation and the propagation of the pressure wave into the surrounding gas. Numerical simulation is an important tool for laser-induced gas breakdown producing plasma as well as the subsequent growing and cooling evolution. Its results can have plasma generation and evolution description in details, which is necessary for quantitative analysis to plasma evolution. There are mainly two categories numerical methods concerning laser-induced gas breakdown and the following flow field evolution processes: hydrodynamic

models as well as kinetic models.

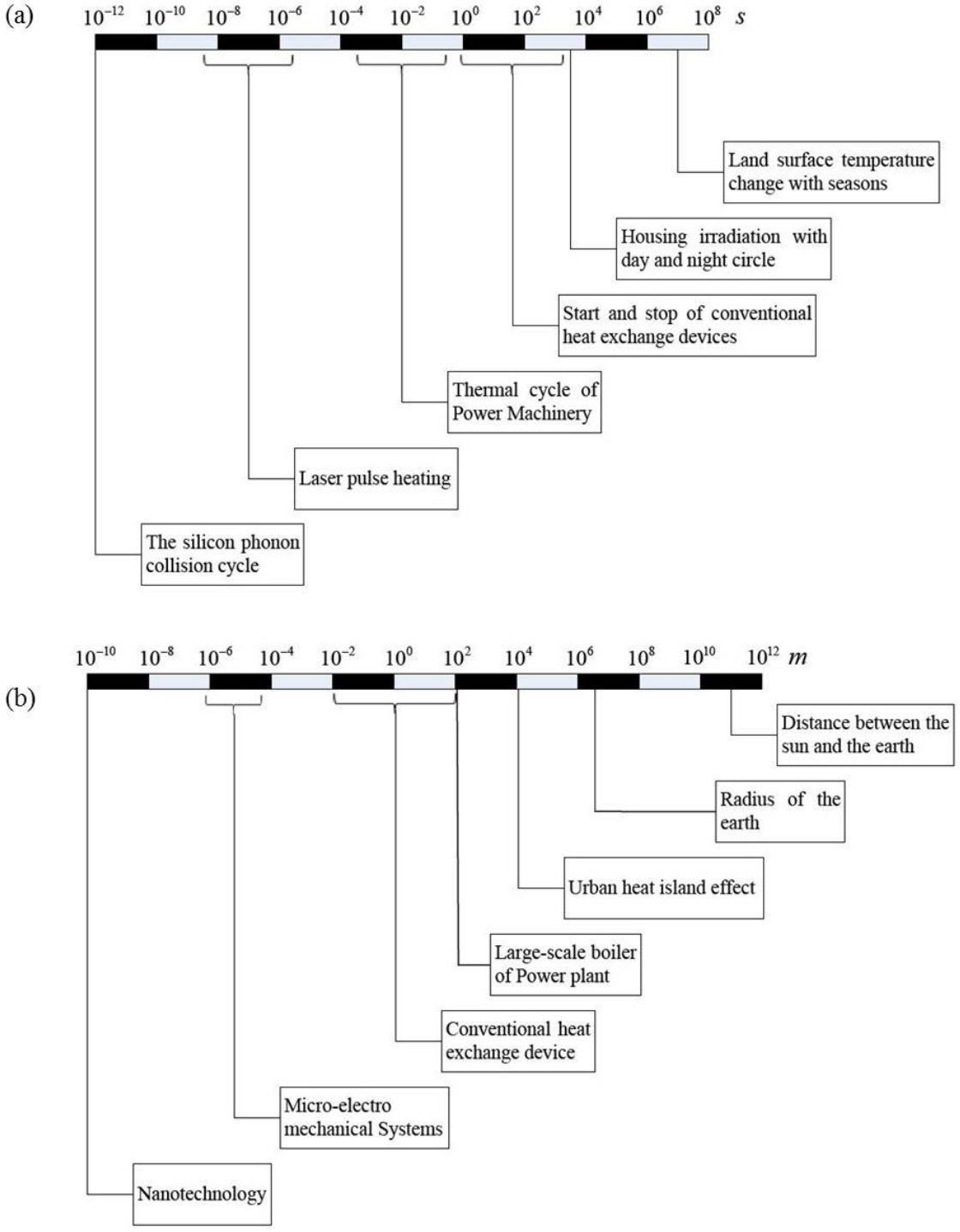

Fig. 1.2 Multi-scale phenomena in (a) time and (b) space.

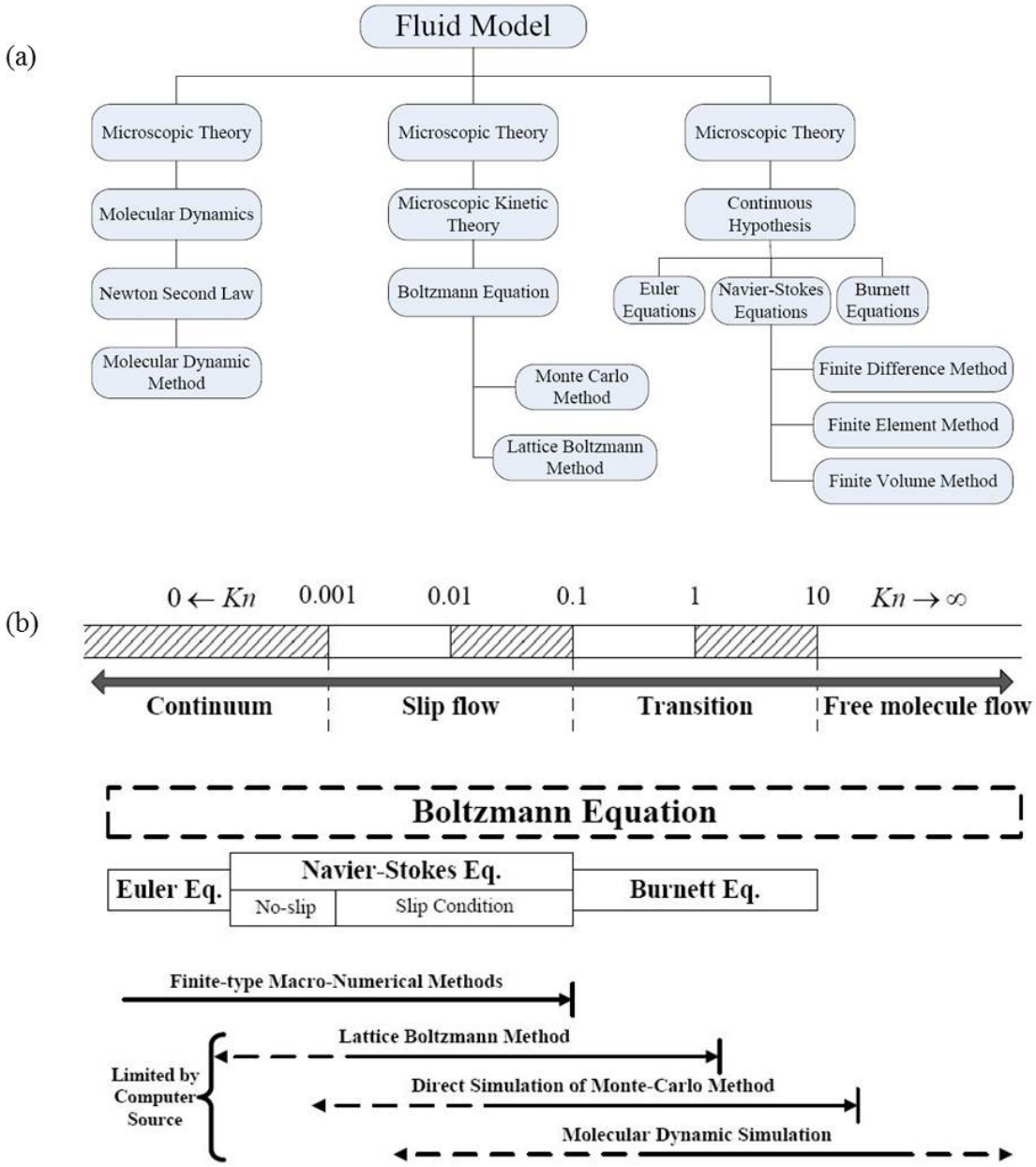

Fig. 1.3 Theoretical backgrounds and selection of different numerical methods (a) Numerical methods and the theoretical background in different scales, (b) Selection of numerical methods depending on Kn number.

In hydrodynamic models, according to disposal of laser energy deposition, numerical models used to laser-induced gas spark can be divided into two classes. The first scheme is to model the inverse bremsstrahlung absorption of plasma in laser energy deposition process. This kind of models can calculate plasma generation and shock wave evolution in details. In the other scheme, the energy deposition process is neglected and the plasma therefore was assumed to form instantaneously. Models built according to this idea are usually to simulate shock wave evolution as well as its

mechanical applications.

In 1975, effects on surface response of laser-supported detonation waves were performed with a cylindrically symmetric two-dimensional Eulerian hydrodynamic computer program by Nielasen [30]. Laser energy deposition and attenuation are accomplished through a free-free absorption coefficient calculated from the Saha-equilibrium ionization of the vapor and air, as well as an absorption coefficient which varies as a power of the vapor density. In 1977 Ferriter [31] studied formation of LSDW by means of a time-dependent, two-dimensional, two-temperature non-equilibrium Lagrangian hydrodynamics code. Oshima [32] investigated formation of laser-supported argon plasma detonation wave in 1991. The interaction of laser and argon atoms are simplified as elastic, inelastic collisions and bremsstrahlung and inverse bremsstrahlung absorptions. And dissipations by viscosity, thermal conduction and radiation were neglected. In 2001, Morales [33] numerically studied propulsion application by LSDW. Considering laser beam optics, inverse bremsstrahlung absorption, ionization/recombination reactions, radiation, heat conduction and convection, the computed laser-supported plasma position agreed well with the experimental results. An 11-species air chemical model with finite-rate chemical kinetics was adopted by Kandala [34] to simulate laser-induced energy deposition process. In this model, instead of multiphoton ionization process, seed electrons were used before simulation to initiate electron cascade ionization producing breakdown. The inverse bremsstrahlung absorption of laser energy was performed by employing of electron-neutral absorption coefficient. For the displacement of the absorption region, the reflectivity coefficient depending on ionization rate was adopted. But these coefficients had not been modeled well in theory, hence in this simulation there was an optimization process of their relationships with gas pressure and laser intensity depending on fitness between numerical and experimental results. In 2009, Duan [35] used Maxwell and Euler equations together to study the coupled electromagnetic and thermal-mechanical processes concerning with a focused high power laser explosion in gas medium. The electromagnetic fields of laser beam propagating through mixtures are simulated by directly solving Maxwell equations with the finite difference time domain (FDTD) method and free-reflective boundary conditions. Euler equations were solved by constrained interpolation profile method to obtained laser-supported combustion/detonation wave evolution process. While in his simulation constrained interpolation profile calculation was implemented in one dimensional region, so two dimensional calculation of Navier-Stokes is necessary for further detailed exploration of laser producing plasma. Akarapu [36] simulated laser-sustained plasma generation and evolution in flowing argon, the results indicated that a plasma formed by a TEM_{00} mode had a great length and volume and absorbed more energy than a plasma generated by a TEM_{01} model beam.

For the scheme that neglects laser deposition process in gas, the plasma was artificially added instantaneously. Dors and Parigger [37] used commercial software package, CFD-ACE to simulate

the post-breakdown air plasma evolution and expansion processes for 1ms. The initial laser spark temperature was generated for the nominal 10ns optical breakdown plasma. The laser-spark decay flow patterns were shown to develop from the asymmetric laser energy deposition profile to symmetrical with subtle deviations at optical axis. At 100μs a pair of vortex which moved towards the laser was shown. Under assumption of spherical distribution of laser energy in focus spot, Yan [38] used one-dimensional time-dependent Navier-Stokes to perform simulation of flow patterns evolution by laser energy. Mori [39] , assuming the initial plasma parameters distribution as spherical, simulated energy transfer form a laser pulse to a blast wave in reduced-pressure air atmospheres. The energy conversion efficiency was sensitive to the input laser energy and it decreased monotonically with decrease in the ambient pressure. When the energy deposition efficiency was 10%, the simplified model was able to give results consistent with experiments. Shiraishi [40] used one dimensional and quasi one dimensional wave to numerically studied laser-supported detonation wave propagation through argon for propulsion purpose. Corresponding to thermal non-equilibrium in spark, two-temperature model was adopted: electron temperature related to electronic mode is separated from the heavy particle temperature related to other modes. The considered microscopic processes included cascade ionization, bremsstrahlung and inverse bremsstrahlung absorption. Ghosh and Mahesh [41] used three different models based on different levels of physical complexity to simulated the shock formation, shock propagation and subsequent collapse of gas spark evolution in air. For the first model, the chemical reactions were neglected and the fluid properties in compressible Navier-stokes were assumed as constant. In the second model, the properties are assumed to vary with temperature only. In the third model, the effects of both temperature and pressure to fluid properties were considered. For each model the flow field is found to evolve in a qualitatively similar manner. At short times, vorticity in flow was found generated by baroclinic means. At longer times, vorticity is generated as a result of the reverse flow in the plasma core.

Kinetic model about plasma are usually used for plasma generation in the breakdown process. Longo [42] modeled electron and ion transport in non-equilibrium plasmas using Monte-Carlo method. Emphasis on the coupling of particle transport with the space charge fields and chemical kinetics, the one-dimensional, self-consistent model successfully simulated a parallel-plate radio-frequency discharge in pure hydrogen. Laser-induced breakdown in air and behind droplets was simulated using Monte-Carlo simulation by Müsing [43]. After comparison between numerical and experimental results, the Monte-Carlo simulation was able to successfully predict the minimum laser energy for breakdown as well as its variation with gas pressure, laser pulse length, focusing spot size of focusing lens. The main advantage of the Monte-Carlo method over alternative techniques, such as finite volume, finite difference and spectral methods, is the simplicity of implementation. This simplicity is particularly evident when the problem is multi-dimensional and

when the boundary conditions are complex. This important advantage is balanced by the necessity use a large number of simulated particles to reduce the numerical errors.

In 2008, Tartar [44] used a kinetic model to simulated cascade growth forming plasma in the electromagnetic field of a focused intense laser pulse. The model is built under the energy conservation of electron production consumption, electron energy increase, electron absorption of laser energy, electron dissipation by conduction to heavy particles and energy flow for excitation of electronic states. Under acting of laser beam with pulse width of 14ns, pulse energy of 26mJ, the exponential increase of electron growth stated after 5.5ns and the plasma state defined by about 1% of ionization was reach at 7ns. Within the subsequent laser pulse, electron number density decreased strongly by the fast expanding plasma. For electron temperature, it increased sharply by absorption of laser energy at the pulse states. In the following, the electron temperature was a result of a very fast almost stationary equilibrium of laser energy absorption and loses.

As the other scheme based on microscopic kinetic theory, in lattice Boltzmann method, the discrete Boltzmann equation is solved to simulate the flow with collision models such as Bhatnagar-Gross-Krook (BGK). By simulating streaming and collision processes across a limited number of particles, the intrinsic particle interactions evince a microcosm of viscous flow behavior applicable across the greater mass. Li [45, 46] employed a rescaling process to modified the existing LBM models and then simulated weakly ionization plasma evolution process. The rescaling process was based on two rules: (1) the physical viscosity is equal to the lattice viscosity, and (2) the characteristic flow velocity due to the extent force should not be altered by the scheme. Furthermore, Li [47, 48] synthesized the developed model with the finite difference time domain method and the finite volume method to simulate incompressible, resistive magnetohydrodynamic flow as well as laser interaction with weakly ionized helium plasmas. In simulation of interaction of laser and helium plasma, phenomena of ionization rate increase, electron temperature increase, electron temperature saturation, electron-ion and electron-neutral temperature balance were achieved.

1.4 Major Contents of This Dissertation

When a laser beam with high intensity is focused into gas, because of multiphoton ionization, few molecules can be ionized releasing free electrons in the focus spot. The electrons can readily obtain laser energy via inverse bremsstrahlung to increase their energy. If the gained energy is high enough to overcome the ionization potential, electrons are able to ionize new molecules producing new seeding electrons, which is named as electron impact ionization. The accumulating electrons continuously participate electron impact ionization causing electron cascade and leading breakdown of the gas, which produces the initial plasma in the focus spot of the laser beam. Within the remaining laser pulse, the plasma will absorb laser energy intensively and its temperature and

pressure increase sharply. Accompanying that the plasma grows towards the len in the opposite direction of the laser beam, and this movement is named as laser-supported detonation wave. When the laser pulse is ended, the hot plasma will expand in the form of a shock wave at liberty because of the sharp gradients of temperature and pressure. Laser-induced gas breakdown and the following spark evolution can be used for laser ignition, laser propulsion, laser-induced breakdown spectroscopy, and so on, hence it is of great importance in research and application.

The present study treated laser-induced gas breakdown and the resulting spark evolution as the following three progressive steps : propagation of the laser beam, interaction between laser and gas or plasma within the laser pulse, spark evolution after the laser pulse. And the content in this dissertation includes four parts: firstly the above three steps were respectively modeled and numerically studied, secondly inspired by numerical work, the gas pressure, laser pulse width, laser wavelength, laser pulse energy were adopted for the control of gas breakdown process in laser-induced breakdown spectroscopy to increase the signal to noise ratio of iodine measurement in gas.

To get the real-time electric and magnetic fields, the propagating laser beam was modeled by Maxwell equations and solved by the finite difference time domain method. After adoption of the staggered Yee mesh system, the discrete Maxwell equations were obtained. In order to simulate laser propagation process in infinite space in the limited computational region, the perfectly matched layer absorbing boundary conditions were introduced and used. Via the different incident wave sources, the simulation obtained distributions of the electromagnetic field, energy density as well as curves of variations of energy density, light intensity of the focus point with time.

For gas plasma generation and interaction between laser and plasma, a hybrid model was developed in present research. Propagation of the laser beam was model by Maxwell equations and solved by the finite difference time domain method. Evolution of particle species in plasma generation and growth processes was modeled by continuous Boltzmann-BGK equation and solved by the finite volume method. The macroscopic equations about energy exchange between laser and plasma were deduced from the Boltzmann-BGK equations and solved by the finite volume method. The three numerical methods were coupled in the same mesh system using the smallest time step to simulate interaction between laser and plasma as well as processes of gas plasma generation by laser irradiation. The simulation results showed the built hybrid model was able to calculate the thermo-mechanical effects of interaction between laser and gas or plasma.

The spark evolution by laser energy deposition in argon was described by a axisymmetric model and simulated using Fluent. Molar mass, specific heat capacity, conductivity, viscosity, acoustic speed, chemical reaction of the plasma mixture as well as specific heat capacities of substance in the mixture were treated as functions of temperature and added in compiled UDF for calls by Fluent. The calculation obtained field distributions of pressure, density, temperature as well as

velocity in real time. In the initial stage of spark evolution, the axial propagation of the shock wave was stronger than the radial and the wavefront was in ellipsoidal. With time elapses, the wavefront gradually changed to spherical. The pressure in the spark core decreased with propagation of the shock wave, but the molecule moved outward unceasingly because of inertia when the core pressure was equal to the ambient pressure. These movements caused the excessive expansion of the spark and made the inverse pressure gradient, which led the ambient gas moved inward the core of the spark along the laser axis. By extrusion of the injected gas, the spark kernel formed a toroidal shape and deviated gradually from the axis.

Detection character of iodine by low pressure and short pulse laser-induced breakdown spectroscopy was experimentally studied. The importance of multiphoton ionization and electron impact ionization in gas plasma generation process of LIBS can be controlled by gas pressure, pulse width, laser wavelength and pulse energy. When laser-induced breakdown spectroscopy was used for iodine measurement in nitrogen, the ratio of signal to noise of 1300 Pa, ns, 1064 nm LIBS was higher than that 30 kPa, ns, 1064 nm LIBS. For nitrogen at the same pressure, signal to noise ratio of 532 nm LIBS was higher than that of 1064 nm LIBS. Measurement results of the relative emission intensity of I-3(183 nm) to N-1(1743. nm) were used to illustrate the importance of multiphoton ionization and electron impact ionization in gas plasma process of LIBS. The lower pressure was able to strengthen the effect of multiphoton ionization, which improved signal to noise ratio of LIBS for iodine measurement in nitrogen. Shorter laser pulse reduced duration of electron impact ionization, which limited amount of energy of the laser beam absorbed by plasma so that the emission noise of LIBS measurement can be lightened, such as continuous black-body radiation, coexisting molecular emissions. 150 ps LIBS and 35 ps LIBS are also used for iodine measurement in nitrogen, the measurement results showed lower background emissions than that of ns LIBS including blackbody radiation and coexisting molecular emissions, and the relative intensity of emission line of I-3 to N-1 had much larger value. Compared with 150 ps LIBS, 35 ps LIBS had better measurement results. The concentration dependence of iodine signal intensity in nitrogen using ns 1064 nm, ns 532 nm and 35 ps 1064 nm breakdown was studied. The results suggested a linear increase in the intensity of the I-3 signal, and the detection limit of nanosecond breakdown at 700 Pa was 60 ppb. Low pressure and short pulse LIBS was also studied for iodine measurement in air, the detection limit became worse due to the high quenching rate of excited iodine in air even so the short pulse LIBS increased the ratio of signal to noise.

CHAPTER 2. THEORY OF LASER ENERGY DEPOSITION IN GAS

2.1 Introduction

Laser energy deposition in gas and the result fluid dynamic evolution processes can be described the following progressive steps: initial release of feed electrons by multiphoton ionization; ionization of gas in the focal region of the laser beam by cascade ionization; absorption of laser energy by gaseous plasma; rapid expansion of the plasma and detonation formation within laser pulse; and the propagation of pressure wave into the surrounding gas after laser pulse.

2.2 Multiphoton Ionization (MPI)

MPI can occur sporadically and its important role of multiphoton ionization to plasma generation is supplement of seeding electron for cascade ionization. In some cases, multiphoton ionization is the key factor of gas breakdown threshold [49-51]. When the gas density is very low (<100 Torr), multiphoton ionization is the leading process for breakdown occurrence because collisional effects are negligible.

Multiphoton ionization of atom/molecule A can be expressed as

$$A + N\ h\nu = A^+ + e^-, \tag{2.1}$$

where h is the Planck constant, ν is laser frequency, and $h\nu$ is energy for one photon; N is the minimum photon number for multiphoton ionization occurrence, it can be calculated by $N = \varepsilon_i / h\nu + 1$ and ε_i is ionization potential of atom/molecule A.

Many scholars concerned occurrence rate of multiphoton ionization process. Based on N-order perturbation theory the transition probability for N photon absorption can be simply expressed as

$$W_{MPI} = A_{MPI}^N I^N. \tag{2.2}$$

Assuming the photon absorption cross section for an atom to be excited from r-*th* to $(r+1)$-*th* state be the same for all $r = 0$ to $r = N-1$, where $r = N$ represents the stable ionized state, the following equation can be obtained [52].

$$A_{MPI}^N = \frac{\sigma^N}{\nu^{N-1}(N-1)!(h\nu)^N}, \tag{2.3}$$

where σ is the photon absorption cross section. The occurrence of multiphoton ionization needs the high enough laser irradiance. The presence of impurities, such as aerosol particles or low ionization-potential organic vapors, can significant facilitate the generation of the initial electrons. For a Nd:YAG laser beam at 1.604μm, the photon energy is about 1.16 eV, the number of photons required for ionization most gases is about 14, as reported by scholars, the critical number of

electrons for gas breakdown is about 10^{16} cm^{-3} [52]. Thus $F_{th} > 10^{30}$ photons$/\left(\text{cm}^2 \cdot s\right)$ is needed for gas breakdown. Besides, because the rate of multiphoton ionization has nothing with the existing electrons, the electron number density of electrons increase linearly with time under the constant laser intensity.

2.3 Cascade Ionization

The electron cascade is always the dominant mechanism for gas breakdown at moderate to high pressures where there are initial seeding electrons in existence. The electrons absorb laser photons by inverse bremsstrahlung process in which a free electron absorbs a photon within collision with the presence of a third body: a neutral heavy particle or an ion. If the electrons gain sufficient energy, they can ionize the other neutrals on impact, leading to an electron cascade and breakdown the gas.

$$A + e = A^+ + e^- + e^- \tag{2.4}$$

The number of ionization events per unit volume per unit time can be simplified as

$$N_{ec} = \sigma_{ec} \langle v_e \rangle n_e n_i \tag{2.5}$$

where σ_{ec} is the ionization cross section for electron impact, $\langle v_e \rangle$ is the mean thermal speed of electrons. The produced electrons can participate the following cascade ionization process, its concentration increases exponentially with time.

Fig. 2.1 shows curves of ionization cross sections of argon and helium atoms by electron impact. The cross section increase from the ionization threshold $\varepsilon_e = \varepsilon_{thres}$, reaches a maximum at the electron energy several times the threshold energy, and then slowly decreases. The maximum cross section of the order of $10^{-16} cm^2$. In not too dense gas ionization usually begins at much lower temperatures than that corresponding to the ionization potential $\varepsilon_{thres}/kT_e >> 1$. And only those electrons which corresponding to the tail of the Maxwell distribution function possess sufficient energy for ionization, the number for such electrons is exponentially small. Therefore the domain role in Eq. (2.5) played by those electrons whose energies slightly exceed the ionization potential. It has been shown both theoretically and experimentally that the electron impact ionization cross section can be given by [53]

$$\sigma_{ec} = \text{C}\left(\varepsilon_e - \varepsilon_{thres}\right)\left(\frac{\varepsilon_{thres}}{kT_e} + 2\right)\exp\left(-\frac{\varepsilon_{thres}}{kT_e}\right), \tag{2.6}$$

where C is an a constant and can be found in literature [54].

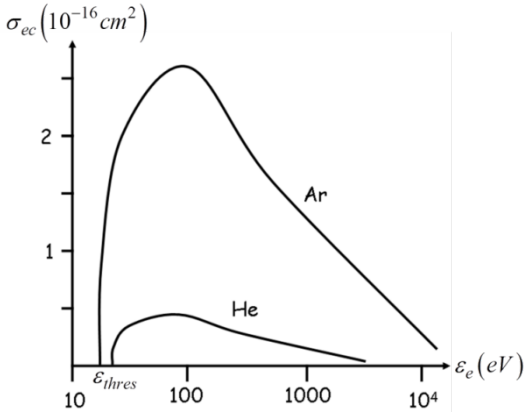

Fig. 2.1 Dependence on the electron energy of electron impact ionization cross section

2.4 Formation of Laser–Induced Detonation Wave

Once the cascade ionization is underway, gaseous plasma can absorb laser intensively and electron temperature increase sharply. Within collisions with electrons, heavy particle particles (ions and neutral) can get laser energy indirectly. Thus electrons act as the medium for transition of electromagnetic energy of the laser beam to thermal energy of heavy particles. By cascade ionization, the hot plasma core is firstly produced in narrowest region of the concerning laser beam because of high intensity.

However the absorption is not confined into the focal region. When the plasma kernel is produced by breakdown, electrons can be heated to about 10^5~10^6 K. Then it emits radiation and most of the radiation energy is in far ultraviolet. The surrounding cold gas layer, the absorption length is only a fraction of a millimeter, and although it is transparent to the laser beam, it absorbs the radiation from the hot plasma. When this layer is ionized and becomes strongly absorbing to the laser light. It is further heated to very high temperature and becomes a new layer of plasma in front of the initially formed plasma. As a result, the boundary of the plasma moves towards the laser. In this fashion, the absorption region is continuously displaced towards the lens, producing a wave of light absorption and gas heated named as LSDW. The propagation of LSDW within laser pulse makes the deposition of laser energy over a larger volume, which limits the peak charged particles and temperature. Another probable measure of the heating of the adjacent cold layer is compression due to the shock wave.

In this stage of interaction of laser and gas, the laser beam is the main source of LSDW. So development of the hot spark is much faster than that in the other directions, which make the plasma grows as a tear shape.

2.5 Propagation of Pressure Wave into Surrounding Gas

When the laser pulse ends, there are great temperature and pressure imbalance between the hot

spark and the surroundings. The coupling or separation of these two imbalance produce complex fluid dynamic phenomena.

In the pressure wave propagation into the surroundings, the cold layer can be heated similarly with LSDW. While this stage is a gradual cooling process, one important chemical reaction, named as three-body recombination, is prevailing. In the three-body recombination reaction, the recombination of electrons with ions takes place by binary collisions with the emission of a photon. And at the same a neutral atom/molecule must act as the third body.

It assumes that the electron is captured by the ion (with a positive charge Z) into a closed orbit and recombines if it passes past the ion with an impact radius r such that the potential energy of Coulomb attraction to the ion Ze^2/r^2 is greater than the average kinetic energy of the electron $3kT/2$. Then the impact radius can be calculated by $r = Ze^2/(3kT/2)$. Thus the number of such collisions per unit volume per unit time is $\pi r^2 \cdot \bar{\boldsymbol{v}}_e \cdot n_e \cdot n_i$ ($\bar{\boldsymbol{v}}_e$ is the average velocity of electrons, and n_e, n_i are electron, ion number density respectively). But in order for capture to take place when the electron passes past an ion, the electron must interact with another electron which can receive the potential energy which is released on capture. The probability of such an event is approximately $\pi(r/Z)^2 \cdot r \cdot n_e$. So the number of recombination per unit volume per unit time is

$$N_{rec} = \left[\pi r^2 \cdot \bar{\boldsymbol{v}}_e \cdot n_e \cdot n_i\right] \cdot \left[\pi (r/Z)^2 \cdot r \cdot n_e\right] = b_{rec} n_e n_i \,, \tag{2.7}$$

where $b_{rec} = \dfrac{\pi^2 r^5 \bar{\boldsymbol{v}}_e}{Z^2} n_e = \dfrac{2^6 \pi (2\pi)^{1/2}}{3^5} \dfrac{e^{10} Z^3}{m_e^{1/2} (kT_e)^9} n_e$.

It is remarkable that the rigorous theory developed by Gurevich [55] leads to the formula

$$b_{rec} = \frac{4\pi \cdot (2\pi)^{1/2}}{9} \frac{e^{10} Z^3}{m_e^{1/2} (kT_e)^9} \ln \Lambda_1 \cdot n_e \,.$$

Here $\ln \Lambda_1$ is a Coulomb logarithm of a particular kind, which can approximately be set equal to one. Then the simplified model differs from the rigorous model only by the numerical coefficient $27/16$. At last, the calculation equation of b_{rec} is

$$b_{rec} = \frac{9.54 \times 10^{-41}}{T^{9/2}} n_e \frac{\mathrm{cm}^3}{\mathrm{sec}} = \frac{5.89 \times 10^{-36}}{T_{eV}^{\ 9/2}} n_e \frac{\mathrm{cm}^3}{\mathrm{sec}} \,. \tag{2.8}$$

After the ionized region turns into an “energy spot” by recombination, the pressure imbalance will then lead to the propagation of a pressure wave away the energy spot. While laser beam pulse is already ended, the blast wave [56] propagate spherically.

CHAPTER 3. NUMERICAL SIMULATION OF ARGON SPARK EVOLUTION

The temporal and spatial evolution of argon spark by laser irradiation has been numerically studied. Mass, momentum and energy conservation equations as well as transport equation of species in spark constitute the two-dimensional axisymmetric model for spark evolution. By solution of these equations, evolutions of spark pressure, density and temperature fields are obtained. In propagation of the shock wave, the shape of wavefront changes from elliptic to spheric. Because of the excessive expansion of high temperature spark mixture, a collapse occurs at about 5 μs. Evolution of high-temperature kernel is firstly controlled by propagation of the shock wave. Because of the collapse in the core of argon spark, the external cold gas penetrates into the origin of spark, which makes the high-temperature kernel be divided into two parts: one locates in the axis of the laser beam, and the other is in a toroidal shape.

3.1 Introduction

When a high intensity laser beam is focused into air, atoms/molecule near the focus spot can be ionized producing plasma. This laser-produced gas plasma (LPAP) process can be described by the progressive steps: initial release of free electrons by multiphoton ionization, ionization of gas by electron impact ionization, absorption of laser energy by the initial plasma, wave formation by rapid expansion of the plasma and the propagation of the pressure wave into the surrounding gas. When compared with other plasmas, because the laser frequency is greater than that of LPAP, the beam can propagate into the interior of LPAP where it is absorbed intensively leading to high plasma temperature. LPAP can be used for laser propulsion [57], laser-induced breakdown spectroscopy [58], laser ignition [6] as well as supersonic flow control [59].

Morphological characteristics of laser-generated gas spark are firstly studied. Harilal measured the optical emission of frequency doubled Nd:YAG laser-generated air spark at atmospheric pressure [60, 61]. Two dimensional time-resolved spontaneous views of spark from 1 to 5500 ns showed that the plasma is firstly produced near the focus spot. While with absorbing more laser energy, the plasma grows faster along with the laser propagation direction. When the ambient pressure is changed to 50 torr the spark was confined to the focal volume, which showed that multiphoton ionization is domain at lower pressures rather than cascade-like process at atmospheric pressure. Using both Rayleigh scattering and time-resolved emission spectroscopy, Huwel recorded the spatial and temporal evolution of laser-generated argon and nitrogen sparks during the first tens of nanoseconds to complete dissipation [62, 63]. Shape of spark transforms from a reverse-dumbbell to an elongated ellipsoid around 5 μs and to an oblate shape after approximately 10 μs. However at

approximately 40 μs the hot region is collapsed forming a toroidal structure. At the same time, a jet like movement of hot gas was also observed backward the direction of the igniting laser. These two phenomena were found in pure elemental gas spark, so formation of the toroidal flame front and the jet-like movement is the direct result of laser energy deposition in gas. Using ICCD camera system, Glumac recorded the elaborated evolution of air spark within 1 ms at different pressures [64]. At pressure lower than 0.5 atm, the spark originates from a central point and propagates in a larger total area of the spark and a bimodal structure, which is one another evidence that multiphoton ionization is dominant at lower pressures. Chen and Wintner paid their attention to laser-induced spark adapted to ignition application. The results provided an understanding of the plasma kernel dynamics and the flame development of NH_3/O_2 mixture [65, 66].

Measurement of plasma temperature and number density of particle species in spark is vital to further understanding of laser-plasma interaction. Yalcin used LIBS technology to measure plasma temperature, electron number density in time scale of microsecond [67]. The electron number density of atmospheric-pressure N_2 plasma temperature at 0.35 and 1.4 μs were 1.2×10^{18} cm^{-3} and 1.9×10^{17} cm^{-3} respectively. Huwel got peak temperatures of laser-produced, atmospheric-pressure argon and nitrogen sparks at delay times from 10 to 10000 μs [63]. The spark had peak temperature of approximately 10000 K at delay time of 60 μs. And the cooling rates of similar magnitude ranging from approximately 100 K/μs at delay times between 50 and 100 μs to a final slow rate of only approximately 1 K/μs during the final stages around 4 ms. Glumac had measured the temperature and electron number density of air spark for longer time [68]. For early times, from 50 ns to 1 μs, the temperature and electron number density were measured from the emission spectra between 490 and 520 nm where NII emission lines are observed. For the longer temporal evolution, planar temperature measurements were measured using filtered Rayleigh scattering from 20 to 1000 μs from the initial laser pulse. The peak temperature was approximate 4100 K at 20 μs and decays to 580 K by 1 ms. This planer temperature images clearly showed a center jet propagating in the opposite direction as the initiating laser beam while the induced torus propagated in the direction of the laser beam. Besides of experimental research, many scholars carried out series of computational studies for laser-induced gas breakdown as well as the subsequent spark evolution processes [37, 41, 69]. Numerical studies are necessary for theory about laser plasma interaction and industrial applications of laser spark. However the computational works so far have focused on blast wave propagation and employed some unrealistic parameters of spark. The present study concerns numerical simulation of flow field distributions in spark evolution after laser energy deposition in argon.

3.2 Mathematic Model and Thermodynamic Parameters of Argon Spark

To simplify the physical problems, the following assumptions are adopted in current study. (1) The hydrodynamic spark evolution is axisymmetric. (2) The spark is in local thermodynamic equilibrium. (3) The spark only consists of Ar, Ar^+ and electron, and these species can be handled as perfect gas.

Based on these assumptions, evolution of argon spark can be modeled as:

$$\frac{\partial \rho}{\partial t}+\frac{\partial}{\partial x_j}\left(\rho u_j\right)=S_m \tag{3.1}$$

$$\frac{\partial\left(\rho u_j\right)}{\partial t}+\frac{\partial\left(\rho u_i u_j\right)}{\partial x_i}=-\frac{\partial p}{\partial x_j}+\frac{\partial \tau_{ij}}{\partial x_i} \tag{3.2}$$

$$\frac{\partial(\rho H)}{\partial t}+\frac{\partial\left(\rho u_j H\right)}{\partial x_j}=\frac{\partial p}{\partial t}+\frac{\partial}{\partial x_j}\left(\kappa \frac{\partial T}{\partial x_j}\right)+\frac{\partial\left(\tau_{ij} u_j\right)}{\partial x_j}-\frac{\partial\left(J_{\alpha j} h_\alpha\right)}{\partial x_j}+S_h \tag{3.3}$$

$$\frac{\partial\left(\rho Y_\alpha\right)}{\partial t}+\frac{\partial\left(\rho u_j Y_\alpha\right)}{\partial x_j}=\frac{\partial J_{\alpha j}}{\partial x_j}+R_\alpha \tag{3.4}$$

The static enthalpy of per mass mixture as well as species α is calculated by

$$h=\sum_\alpha Y_\alpha h_\alpha \tag{3.5}$$

$$h_\alpha=\int_{T_{ref}}^T c_{p\alpha} dT+h_\alpha^0 \tag{3.6}$$

The mass source per volume by chemical reactions is calculated by

$$S_h=-\sum_\alpha \frac{h_\alpha^0}{M_\alpha} R_\alpha \tag{3.7}$$

The mass change rate per volume is calculated by

$$R_\alpha=M_\alpha \sum \hat{R}_{\alpha,r} \tag{3.8}$$

Within the large temperature range considered in this study, the thermodynamic and transport parameters of argon spark have severe variations. Here the specific heat, viscosity, diffusivity, conductivity and acoustic velocity of argon spark mixture are deal with as functions varying with temperature, and their values can obtained in [70-76]. The complex ionization and recombination processes in spark evolution are modeled by Arrhenius formula. The parameters used in Arrhenius formula about these chemical reactions can be found in [77, 78]. To handle the energy consumption in the exothermic and endothermic reactions, the specific heats of substances in the gas mixture are also needed. In this study they are calculated by

$$E_\alpha=E_\alpha^{trans}+E_\alpha^{ele}+\sum_j I_{j-1} \tag{3.9}$$

$$C_{\alpha,p}=\frac{\partial E_\alpha}{\partial T}+R \tag{3.10}$$

Where E_{α}^{trans}, E_{α}^{ele} and I_{j-1} are the molar translational, electric and ionization energies of species α. The data about electronic energy levels used in present study is form NIST [79].

Given the symmetry of laser energy deposition in argon, the computational region is 16 mm in axial direction and 8 mm in radical direction. The axis is coincident with the axis of the laser beam. When the laser beam propagates toward right from left, the initial temperature is shown in Fig. 3.1, the temperature along the axis is calculated by

$$T = 16000e^{700x} \quad x \in [-0.0005\text{m}, 0.0005\text{m}]. \tag{3.11}$$

And the radical temperature is in Gaussian distribution, and the FWHM (full width at half maximum) is calculated by

$$FWHM = 2.82\times10^{4}e^{1050x} \quad x \in [-0.0005\text{m}, 0.0005\text{m}] \tag{3.12}$$

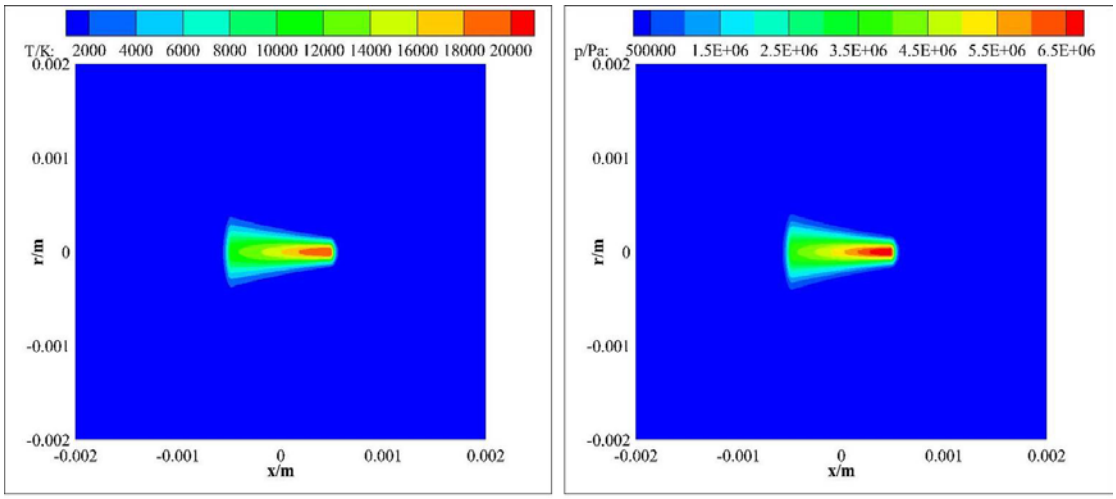

(a) Initial temperature (b) Initial pressure

Fig. 3.1 Initial conditions

To eliminate the unrealistic gradient, the adequate smoothing temperature functions are applied at x=0.5mm and x=0.5mm. The boundary at the axis is defined as axis boundary condition and the other boundaries are defined as pressure outlet boundary conditions. Under the condition of local thermodynamic equilibrium, the initial distributions of particle species in spark can be obtained from the initial temperature profile [80]. Eqs.(1-4) used in current study is calculated by Fluent 6.3.26. The thermodynamic and transport parameters and chemical reactions are modeled as functions of temperature and included in UDF. The specific heats of the spark mixture and substances in spark are set in piece-polynomial in control panel of Fluent. In calculation, SIMPLE algorithm is adopted for pressure-velocity coupling, second order upwind scheme is used for density, momentum, energy and mass fraction discretization in space and first-order implicit scheme is used for unsteady term discretization in time of the control equations.

3.3 Thermodynamic Properties of Argon Spark

3.3.1 Constitution and reactions of argon spark

The argon spark after laser is already in local equilibrium state, so its constitution can be calculated from Saha equation and number densities of particle species in plasma are functions of plasma temperature. Fig. 3.2(a) shows curves of the molar fractions of particle species in plasma variation with temperature. Upon the Fig. 3.2(a) and the initial pressure distribution can be obtained and is shown as Fig. 3.1(b). The molar weight of argon plasma can also be calculated from Fig. 3.2(a) and is shown as Fig. 3.2(b). Variation of molar weight is rewrote as the function of temperature and is included in UDF.

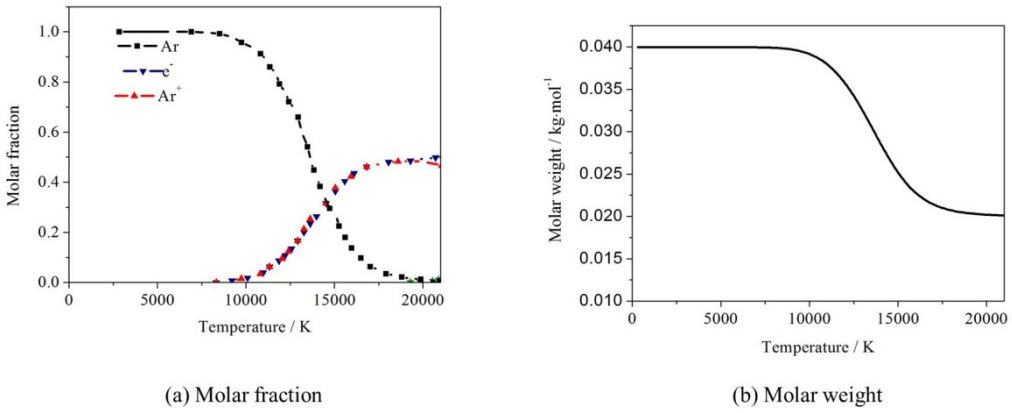

(a) Molar fraction (b) Molar weight

Fig. 3.2 Molar fraction and molar weight of argon spark

In evolution of argon spark, three are reactions of ionization and recombination. These reaction can be modeled by collisional theory, while the present study focuses on hydrodynamic evolution of spark, so the macroscopic Arrhenius is used for description of reactions in argon spark. in Table 2 shows the considered reactions in present study, and reaction(1-2), reaction(3-4) are ionization and recombination reactions respectively. The reaction rate can be calculated using the following equations and the related coefficients are also shown in Table 2.

$$k_{r,i}(T) = A_i T^z \left(\frac{\Theta}{T} + 2\right) \exp\left(-\frac{\Theta}{T}\right) \tag{3.13}$$

$$k_{r,r}(T) = A_r \left(\frac{\Theta}{T} + 2\right) \exp\left(-\frac{\Theta}{T}\right) \tag{3.14}$$

Where $A_{r,i}$ is ionization reaction coefficient in $m^3 \cdot mol^{-1} \cdot s^{-1}$, and $A_{r,r}$ is the recombination coefficient in $m^6 \cdot mol^{-2} \cdot s^{-1}$. Θ is the enabled temperature of reactions.

Table 2 Reactions in argon spark

No.	Reaction	$A_{r,i} / A_{r,r}$	z	Θ
1	$Ar + e^- \rightarrow Ar^+ + e^- + e^-$	2.25825×10^2	1.5	135300
2	$Ar + Ar \rightarrow Ar^+ + Ar + e^-$	1.01170×10^{-2}	1.5	135300
3	$Ar^+ + e^- + e^- \rightarrow Ar + e^-$	4.67812×10^3	---	47800
4	$Ar^+ + Ar + e^- \rightarrow Ar + Ar$	2.10334×10^{-1}	---	47800

3.3.2 Thermodynamic properties of argon spark

The temperature range of the present study is 300 K~20000 K, within which the related thermodynamic properties of spark have intense variation. Fig. 3.3 shows variation with temperature of the specific heat, viscosity, conductivity and acoustic velocity of argon spark. Viscosity, conductivity and acoustic velocity is included in UDF, and the specific heat is modeled as piecewise polynomial of temperature and set in the control panel of Fluent.

The electromagnetic field among charged particle in spark is ignored in present study, so the diffusivity is calculated upon the constant Schmidt number:

$$Sc = \frac{\eta}{\rho D} \tag{3.15}$$

Where Sc is the dimensionless Schmidt number. In order to ensure the same diffusion of particles in spark, the Schmidt number is set as 0.7 in current research.

Besides, there are abundant energy production and consumption in ionization and recombination reaction, the specific heats of particle species in spark are also needed. The specific heat of electrons is as constant of 37888737.6 $\mathrm{J \cdot Kg^{-1} \cdot K^{-1}}$. Fig. 3.4 presents the specific heats of Ar and Ar^+. They are function of temperature and can be calculated by the following equations:

$$E_\alpha = E_\alpha^{\mathrm{trans}} + E_\alpha^{\mathrm{ele}} + \sum_{\mathrm{j}} I_{\mathrm{j-1}}$$

(3.16)

$$C_{\alpha,\mathrm{p}} = \frac{\partial E_\alpha}{\partial T} + R \tag{3.17}$$

Where is $E_\alpha^{\mathrm{trans}}$ molar translational energy and E_α^{ele} is the electronic energy, I_{j} is the ionization energy, $C_{\alpha,\mathrm{p}}$ is the molar specific heat at constant pressure.

The electronic energy E_α^{ele} of particle species can be calculated as

$$E_\alpha^{\mathrm{ele}} = \frac{N_{\mathrm{A}} \sum_{\mathrm{i}} \varepsilon_{\mathrm{i}}^\alpha g_{\mathrm{i}} e^{-\varepsilon_{\mathrm{i}}^\alpha / k_{\mathrm{B}} T}}{\sum_{\mathrm{i}} g_{\mathrm{i}} e^{-\varepsilon_{\mathrm{i}}^\alpha / k_{\mathrm{B}} T}} \tag{3.18}$$

Where N_A is the Avogadro's constant, ε_i and ε_j are the energies at energy levels of i and j of particle species α.

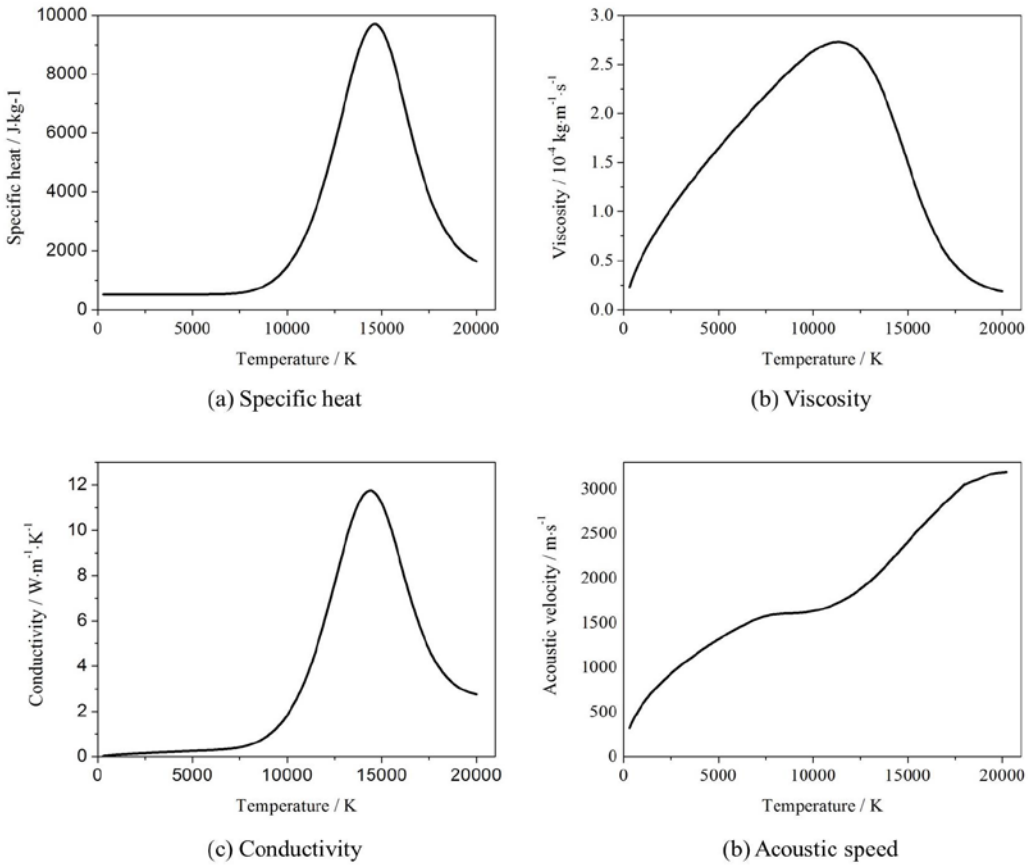

Fig. 3.3 Thermodynamic properties of argon spark

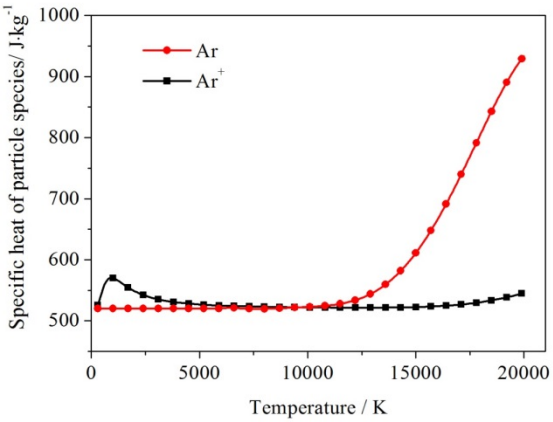

Fig. 3.4 Specific heat of particle species in argon spark

3.4 Simulation Results of Argon Spark Evolution

3.4.1 Mesh independent verification

Numerical verification is also implemented to eliminate the dependence of simulation results on grid system. For the computational region of 8 mm×16 mm, three mesh systems of 360×720, 480×960 and 600×1200 are used. Fig. 3.5 shows simulation results of the maximum electron number density as well as the maximum velocity under the three mesh systems. To balance the computational cost and results accuracy, the mesh system of 480×960 is adopted in present study.

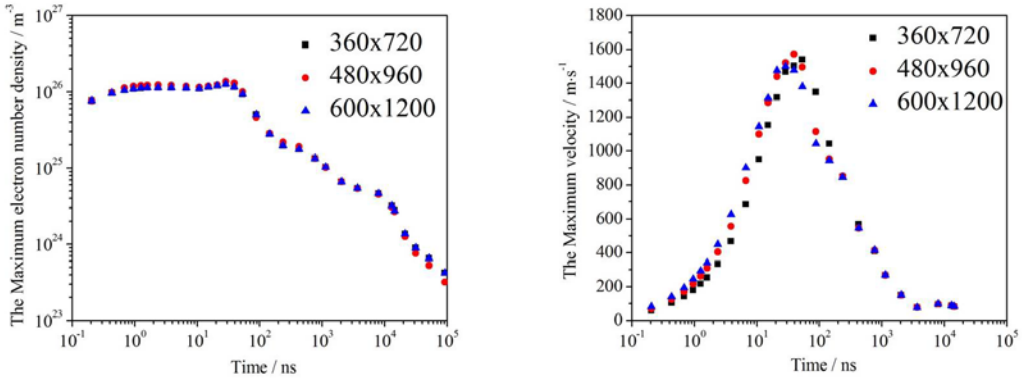

(a) Electron number density (b) Velocity

Fig. 3.5 Results of mesh independent verification

3.4.2 Pressure decay

Fig. 3.6 presents the maximum pressure decay process versus time. In the initial 100 ns, the maximum pressure drops to 20% of its initial value. While at the following time range, the fall of the maximum is very slow. And at about 30 μs, the maximum pressure is about equal to the ambient pressure.

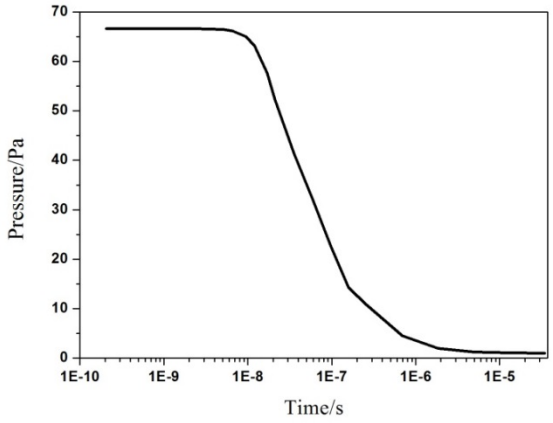

Fig. 3.6 Decay of the maximum pressure of argon spark

Fig. 3.7 illustrates evolution of argon spark pressure fields. At the initial stage, the axial shock wave propagation is dominating. The location of highest pressure region moves against the laser propagation direction and its maximum value descends sharply. Following the axial decay, the radial decay is also activated at about 150 ns. As shown in Fig. 3.7(d) radical movement of the high pressure region leads formation of a toroidal high pressure region at about 0.261 μs. In the middle stage of pressure deacy, an integrated shock wavefront is formed. Firstly the shape of wavefront is similar with the initial shape spark, however as time elapsed it changes to elliptic at about 1.1347 μs as shown in Fig. 3.7(e). At this moment its major radiuses locate at the axis, while following that the radical movement dominates the shock wave propagation. The shape of wavefront is in spheric at about 8 μs as shown in Fig. 3.7(h). After 8 μs, the shock wave advances spherically as time went on. Besides of the shock wave propagation, alternation of pressure gradient is also a matter of concern. The pressure in the spark core is highest at the initial stage, but the excessive expansion takes place for the mixture locating in the core. As shown in Fig. 3.7(f) at about 3μs the pressure of the spark core is about 7500 Pa which is less than the ambient pressure. Even if this reversed pressure gradient, the shock wave still propagates spherically. But the pressure of the spark core increase gradually. As shown in Fig. 3.7(g) the minimum pressure is about 8000 Pa at 4.9107 μs. At this moment a break is formed at the right end of low-pressure mixture lump locating in the core of spark. And as shown in Fig. 3.7(f), a penetration band is formed along the axis where the pressure is larger than its circumjacent region. The reason for this phenomenon will be explained in detailed in the next section.

3.4.3 Velocity vector and vorticity

Fig. 3.8 shows the velocity fields at 0.261 μs and 3.014 μs. As shown in Fig. 3.8(a), because of the high pressure of spark, the velocity vectors in the spark existing region are all outward and its

peripheral magnitude is bigger than that in the core. However as shown in Fig. 3.8(b) the direction of velocity vector changes at 3.014 μs. The velocity vector of the right region of spark is inward, which means that the gas outside of the spark moves into the core of spark. By comparison between the pressure and velocity vector distribution at 3.014 μs as shown in Fig. 3.7(f) and Fig. 3.7(b), the swerve of velocity vector is reasonable because of the negative pressure gradient. The gas movements into spark core leads to the penetration band of high pressure along the axis as shown in Fig. 3.7(f).

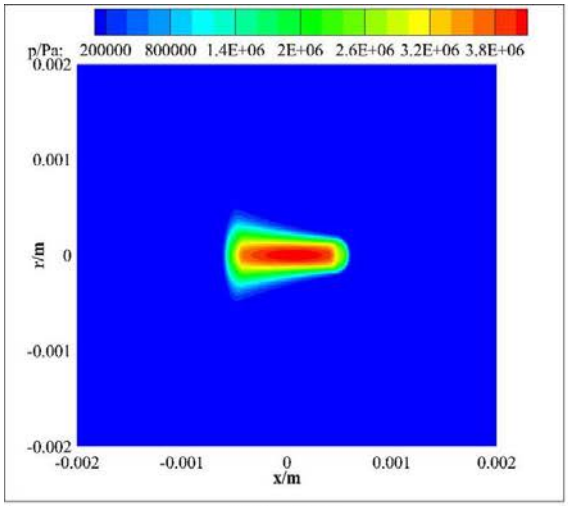

(a) 35.358 ns

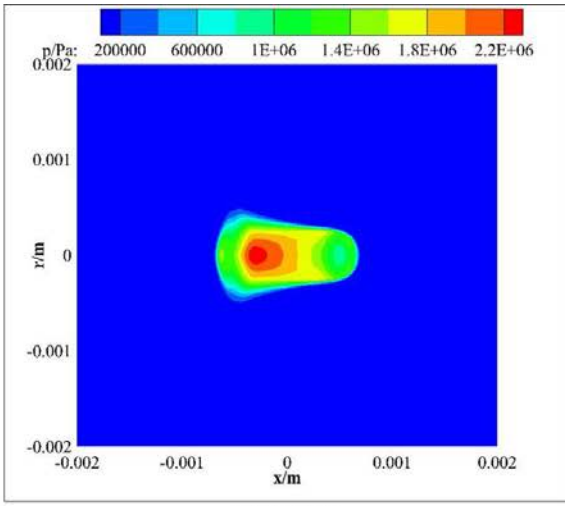

(b) 97.123 ns

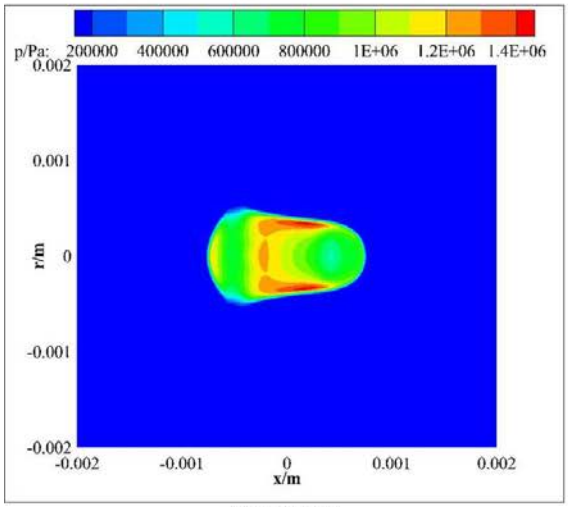

(c) 0.15946 μs

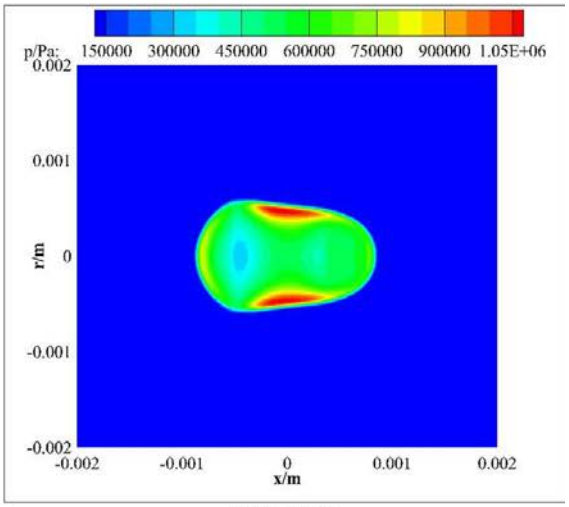

(d) 0. 261 μs

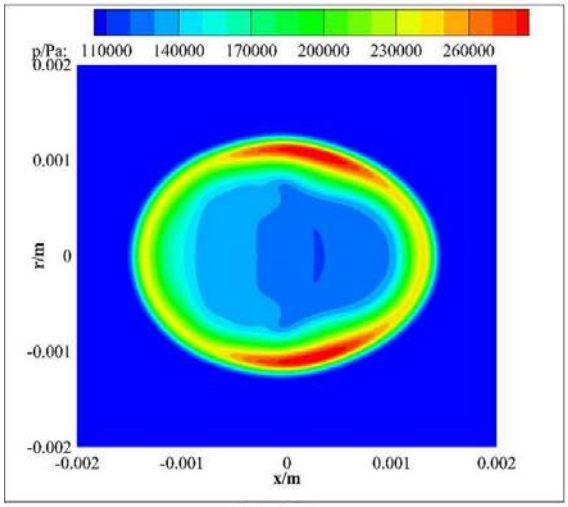

(e) 1.1347 μs

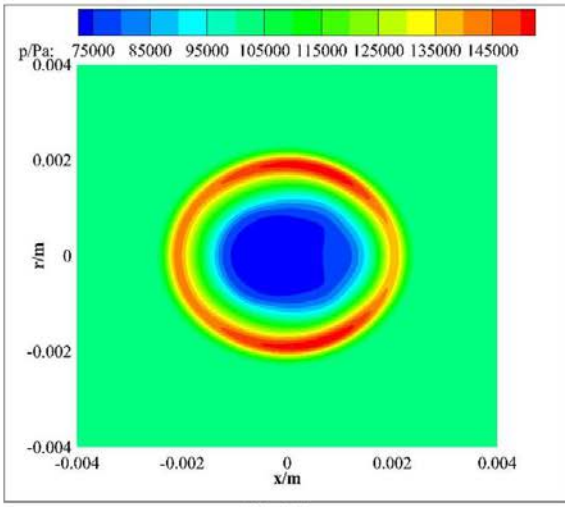

(f) 3.014 μs

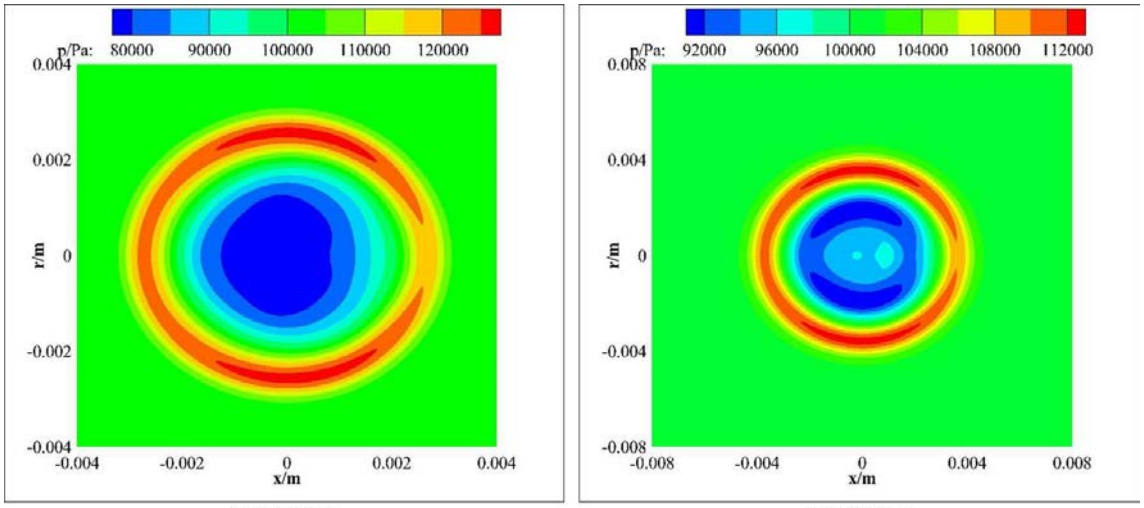

(g) 4.9107 μs (h) 8.0002 μs

Fig. 3.7 Evolution of pressure fields

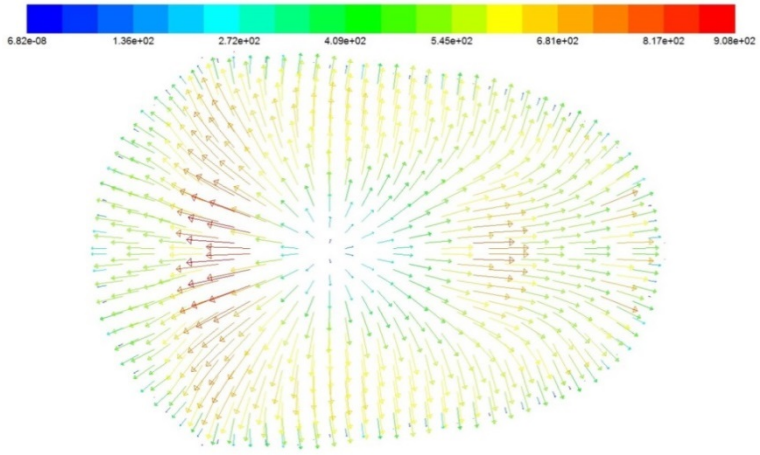

(a) 0.261μs

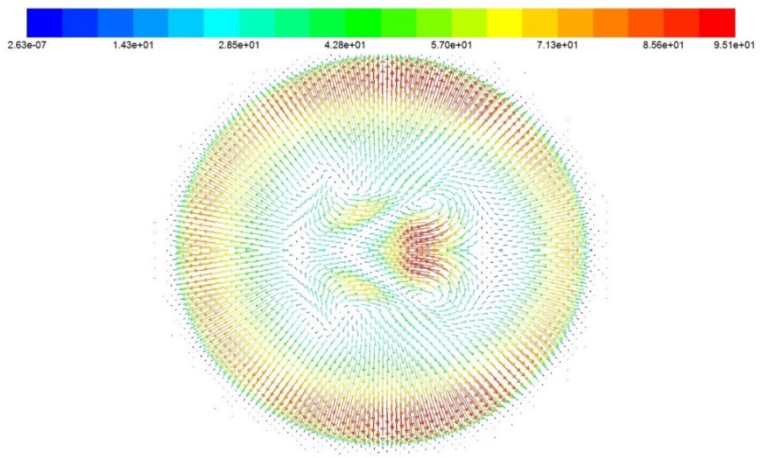

(b) 3.014μs

Fig. 3.8 Velocity vector distributions of argon spark

Fig. 3.9 presents the vorticity distribution of the flow field. Because of extrusion by the penetrating cold gas into spark core, vortex is produced near the axis. And with time elapses, the vortex moves depart from the axis.

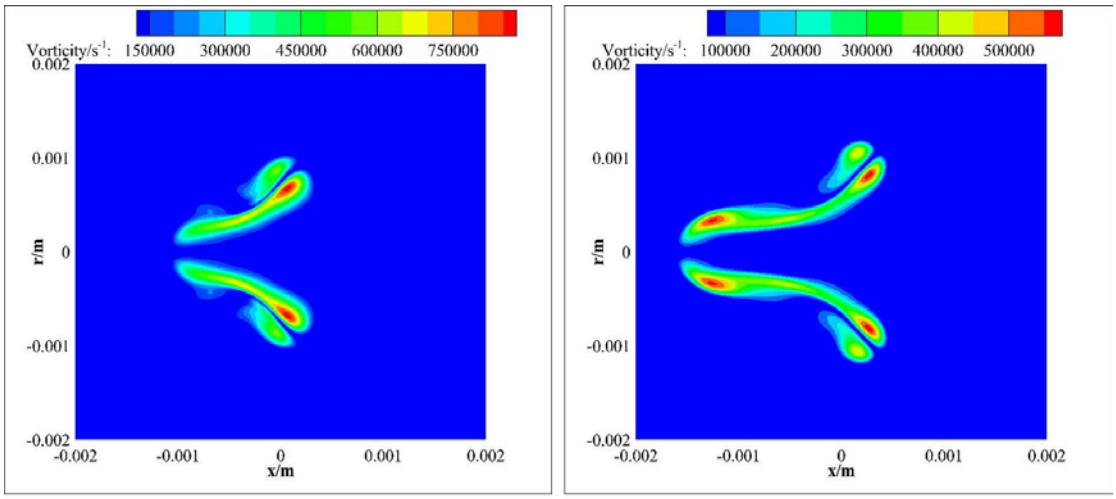

(a) 21.23μs (b) 34.583μs

Fig. 3.9 Vorticity distributions of argon spark

3.4.4 Density field

Fig. 3.10 illustrates the evolution of density fields of the spark. As shown in Fig. 3.10(a) and (b), the density field can be divided into three parts: the innermost layer is plasma whose high temperature leads the low density. The middle layer is the wavefront and its density is biggest because of compression of the shock wave. The outermost layer is the ambient gas. From the density field shown in Fig. 3.10(a), we can know that at the initial stage the axial propagation of the shock wave is stronger than its radical propagation, which leads the denser mixture at the right and left sides of the spark. At about 3 μs shown as Fig. 3.10(d), the outer layer gas is injected into the spark core by the negative pressure gradient. At last the cold gas can run through the spark core as shown in Fig. 3.10(f). The plasma whose density is lower is pushed off the axis.

3.4.5 High-temperature kernel

Evolution of the temperature distributions are shown in Fig. 3.11. At the initial stage evolution of the temperature distribution is dominated by the shock wave whose propagation spreads the temperature profile outward and leads the maximum temperature reduction. In the middle stage, spread of the high-temperature kernel and propagation of the shock wave are decoupled. Because of the negative pressure gradient leaded by the excessive expansion of high temperature kernel, the external cold gas moves inward and push the high temperature kernel to the origin of the spark. At about 5 μs the high temperature kernel is spherical as shown in Fig. 3.11(c). With the more cold gas

moves into the core, the kernel looks like “C” as shown in Fig. 3.11(d). At last the cold gas nearly can run though the core. The high temperature mixture is divided into two parts: one part is in a toroidal structure and the other one locates at the axis. With time elapses, the toroidal moves depart from the axis while the other part moves against the direction of laser propagation. This phenomenon can be also seen from the vorticity distribution as shown in Fig. 3.9.

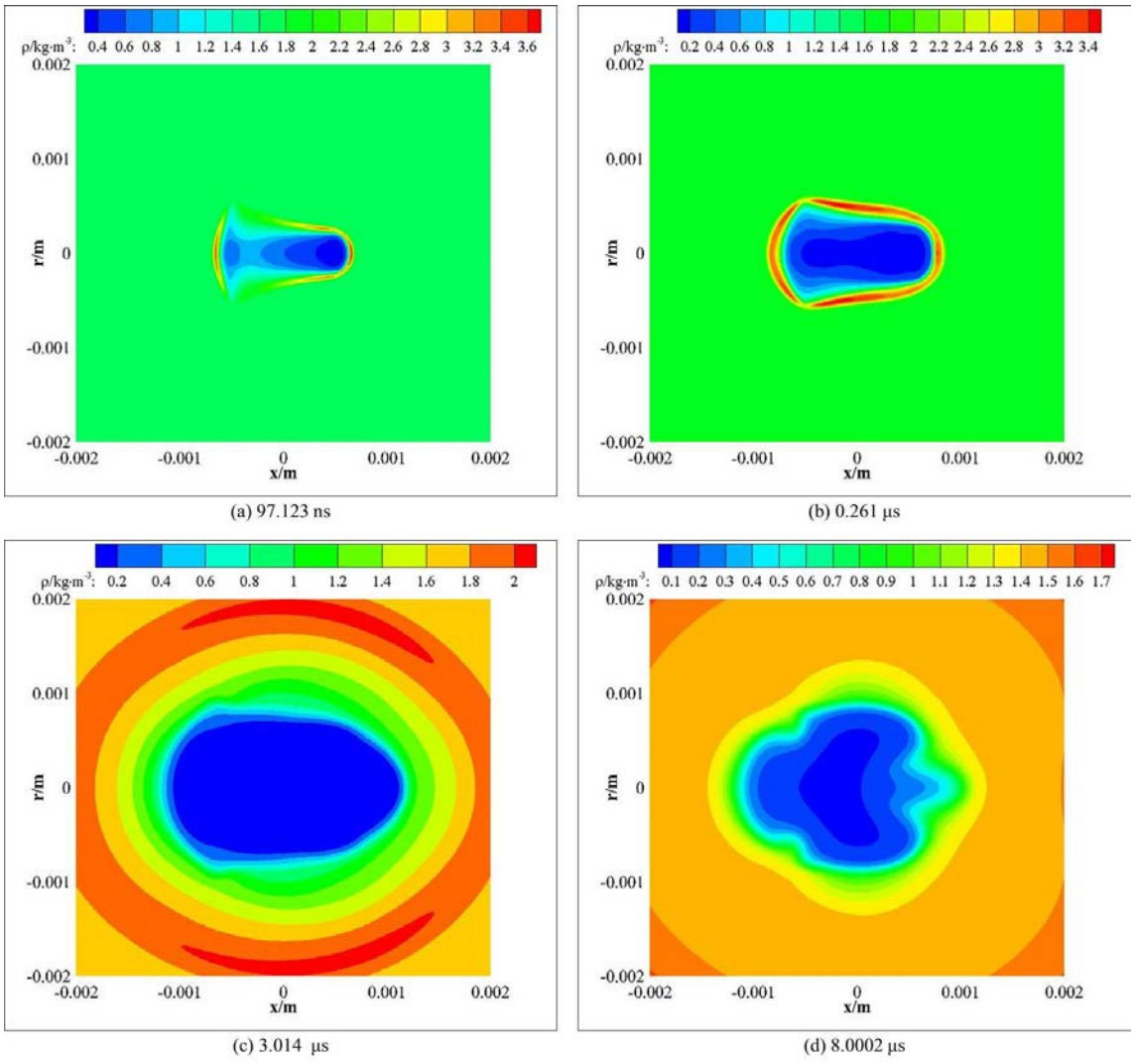

(a) 97.123 ns

(b) 0.261 μs

(c) 3.014 μs

(d) 8.0002 μs

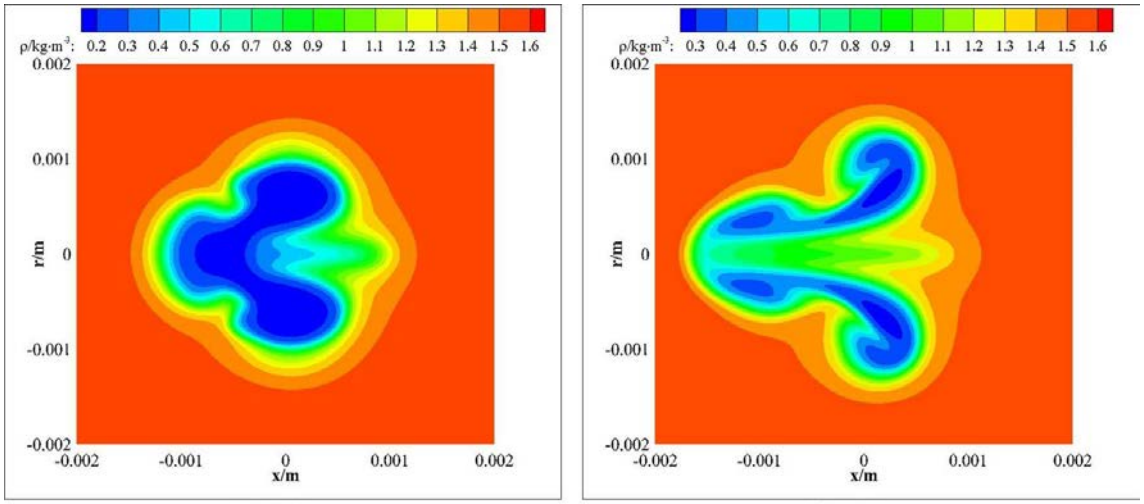

Fig. 3.10 Evolution of density fields

3.4.6 Wavefront of the shock wave

Fig. 3.12 presents axial and radical pressure distributions versus time. As shown in the figure, pressure of spark decreases quickly in the initial propagation of the shock wave, and with time elapsed the attenuation amplitude reduces gradually. The pressure values are not symmetric in the axial wavefronts. Pressure of the leftward wavefront is bigger than the other side, but the gap among the two side pressures has a downtrend. At 1.347 μs the rightward wavefront pressure is bigger than the leftward value, while their values equal to each together at about 1.8495 μs. After 1.8495 μs the pressure along the laser axis is in symmetric. Besides at the same instant the excessive expansion of the spark can be shown clearly in Fig. 3.12(b), the inner pressure of the spark is already smaller than the ambient value. However the inner pressure decreases unceasingly from 1.8495 μs to 4.9107 μs, and the inverse pressure gradient become larger. As shown by the above velocity vector field, this phenomena is reasonable because of the gas in the inner of the spark moves outward continuous by inertia. After 4.9107 μs, pressure in the core of the spark increases gradually, which is because the external cold gas ejects into the core. At about 13.033 μs, the shock wave disappears and the pressure falls back to the ambient pressure. At the initial stage of propagation of the shock wave, pressures at the axial and radical wavefronts are different. While from 4.9107 μs, the shape of the wavefront changes to spherical and pressure at the whole wavefront is equal.

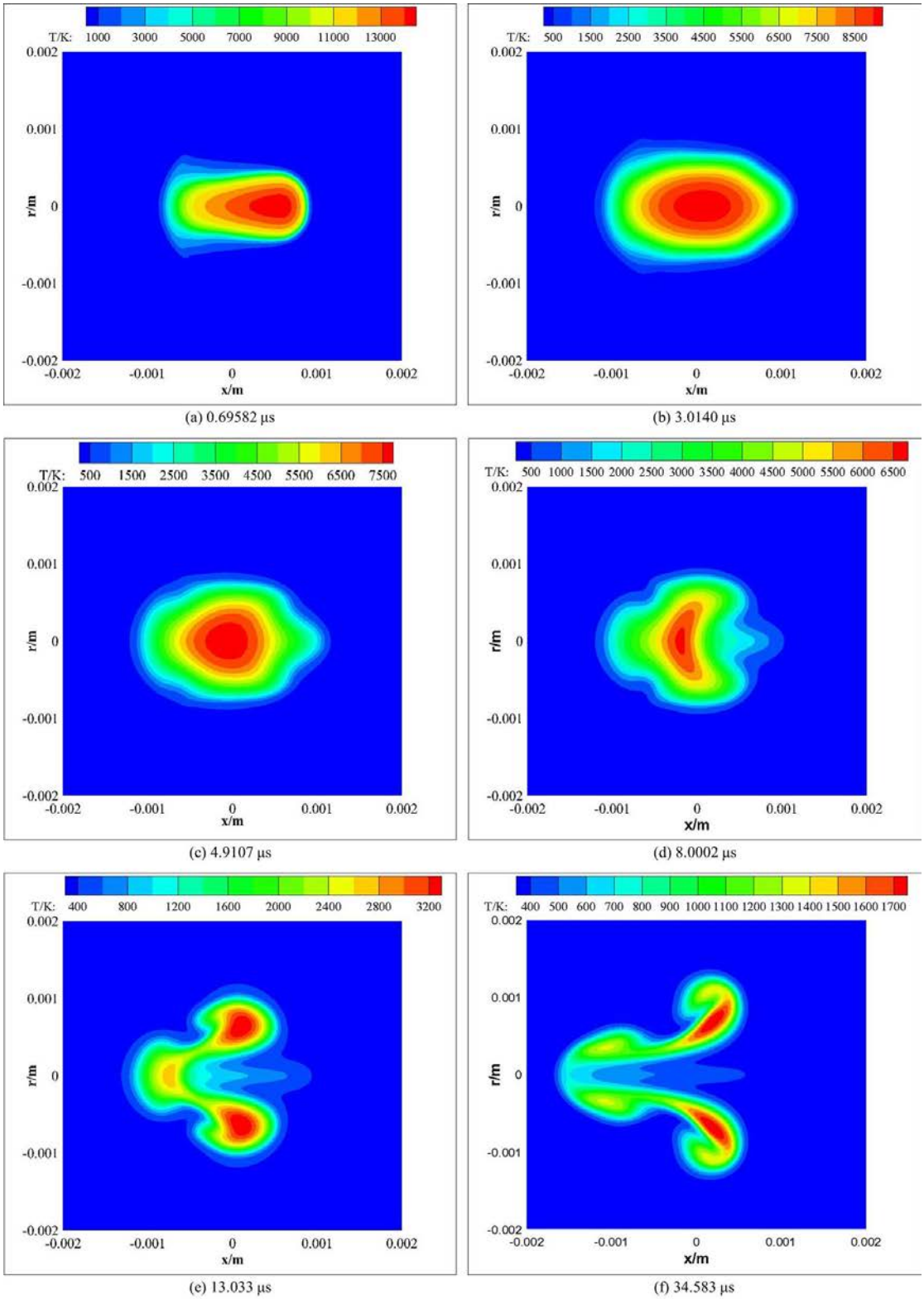

(a) 0.69582 μs (b) 3.0140 μs

(c) 4.9107 μs (d) 8.0002 μs

(e) 13.033 μs (f) 34.583 μs

Fig. 3.11 Evolution of temperature fields

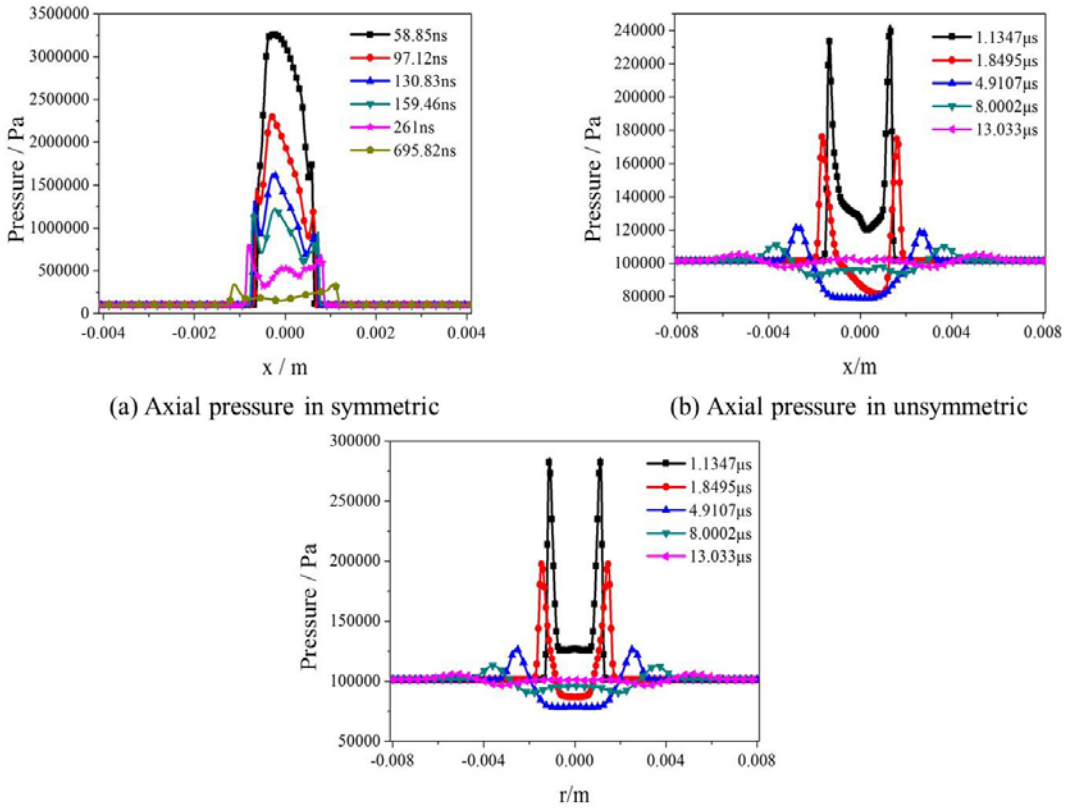

Fig. 3.12 Axial and radial pressure distributions

3.4.7 Comparison with experimental results by other scholars

By filtered Rayleigh scattering technology, Glumac measured the temperature distribution during the later period of the air spark evolution [16]. Fig. 3.13 shows temperature distributions at four time instants. In the figure, the laser beam propagates downward from the upper boundary. As shown by Fig. 3.13, the hot gas were divided into two parts, one located at the axis of the laser beam, the other part formed as a toroidal shape along the axis. From points of Glmac, the reason of this phenomena is the excessive expansion of spark by the asymmetric deposition of laser energy in air. Although the mediums of Glumac's experiment and present study are different, the computational results qualitatively match the experimental results and show the flow field evolution in detailed.

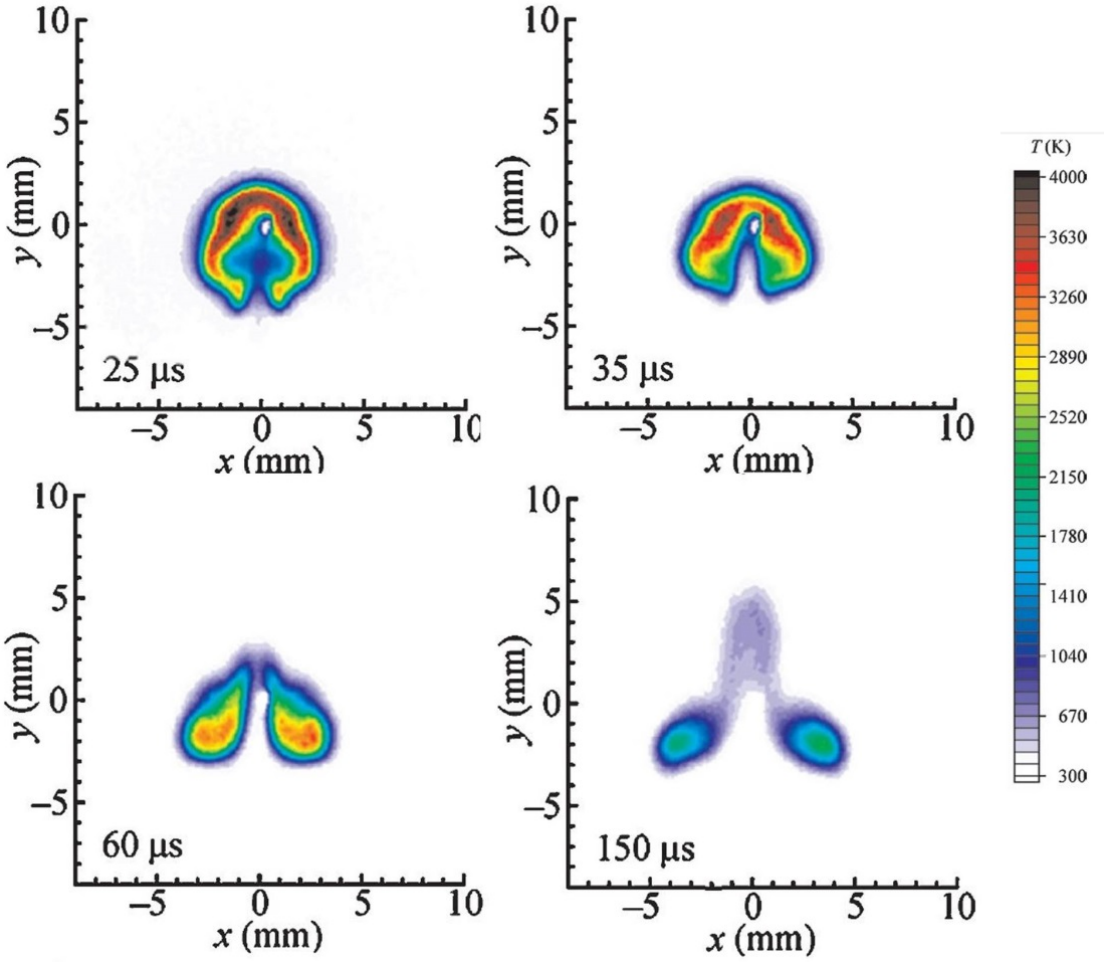

Fig. 3.13 Measured temperature of air spark by Glumac

3.5 Summary

This chapter simulates the argon spark evolution by laser irradiation. Because of the laser energy deposition in argon, an intensive shock wave is formed in the initial stage of spark evolution. The axial propagation is firstly faster than the radial propagation of the shock wave, so the shape of the wavefront changes from elliptic to spheric. At a specific moment, the pressure at the spark core is lower than the ambient pressure. However the negative pressure cannot immediately stop the outward velocity vector of high-temperature mixture, which leads the excessive expansion of the core of spark by the transient remaining outward movement. At last change of the direction of the velocity vector cause a collapse in the core of spark. The injection of external cold gas pushes the high temperature kernel into a toroidal shape.

CHAPTER 4. NUMERICAL SIMULATION OF LASER BEAM PROPAGATION BY THE FINITE DIFFERENCE TIME DOMAIN METHOD

When the high power laser beam is injected into gas, the interaction processes include ionization of gas molecule, optical breakdown, plasma generation, laser-supported denotation as well as propagation and attenuation of the shock wave in the far field. All these processes are the comprehensive thermal-mechanical effect, and they can be divided into three part: laser beam propagation, plasma generation and growth as well as energy exchange between laser and plasma. So combination of separate model and coupled solution of the three parts may after all be accepted as a good way for plasma investigation.

In this chapter, firstly the related theories about plasma generation and growth will be introduced. Maxwell equations, the Boltzmann equation and their numerical solution technologies for laser propagation, plasma generation and growth are the following content. For the energy exchange, the macroscopic energy equations, which will be calculated by the finite volume method, are directly derived from particles' continuous Boltzmann equation. At the end of this chapter the coupled measures among the three numerical methods are stated.

4.1 Laser Propagation and FDTD Method

In all these processes, space-time distribution of laser energy and absorption and scatter of laser beam by the gas play important roles. So in order to have intensive understand of thermal-mechanical interaction between laser and gas, study of generation and propagation of the laser beam is the primary task.

Propagation of laser can be described by geometrical or wave optics. However when laser advance in the plasma, the non-uniform characteristics can only reveal by the wave theory. In wave optics, Maxwell equations are used to model interference and diffraction of light. Besides, thermal radiation, conduction as well as thermodynamic evolution must be described by Boltzmann or Navier-Stokes equations. So we firmly believe that simultaneous solution of these equations a decent measure for generation and evolution of laser spark.

In this research, Maxwell equations are used to laser beam propagation in free space or in laser-supported gas plasma. In the following, Maxwell equations as well as the dependence on each other are firstly introduced according to laser propagation. Then using the Yee algorithm in the finite difference time domain method, the discrete forms of curl equation electric and magnetic fields are obtained. When the total/scatter field and perfectly matched layer boundary conditions are adopted, laser beam with arbitrary incident angle can be injected into computational region. After the staggered solution of discrete equations in time and space domains, electric and magnetic

fields distributions can be known in real time.

4.2 Maxwell Equations

For electromagnetic waves in any medium, the differential Maxwell equations are

$$\nabla \times \boldsymbol{E} = -\mu \frac{\partial \boldsymbol{H}}{\partial t} \tag{4.1}$$

$$\nabla \times \boldsymbol{H} = \varepsilon \frac{\partial \boldsymbol{E}}{\partial t} + \boldsymbol{J} \tag{4.2}$$

$$\nabla \cdot \boldsymbol{E} = \frac{\rho}{\varepsilon} \tag{4.3}$$

$$\nabla \cdot \boldsymbol{H} = 0 \tag{4.4}$$

where $\boldsymbol{E}$, $\boldsymbol{H}$ are electric and magnetic fields, ρ, $\boldsymbol{J}$ are charge and electric current densities, and ε, μ are electric permittivity and magnetic permittivity respectively.

Eq. (4.1)-(4.4) are curl and divergence equations of electric and magnetic fields, while they are not independent. For Eq. (4.1), after a divergence operator, $\nabla \cdot (\nabla \times \boldsymbol{E}) = -\nabla \cdot (\mu \partial \boldsymbol{H} / \partial t)$ is obtained, then the magnetic field is a solenoidal vector.

Similarly, after a divergence operation of Eq. (4.2), we can get Eq. (4.3).

$$\nabla \cdot (\nabla \times \boldsymbol{H}) = \nabla \cdot (\varepsilon \frac{\partial \boldsymbol{E}}{\partial t} + \boldsymbol{J})$$

$$\nabla \cdot (\varepsilon \frac{\partial \boldsymbol{E}}{\partial t} + \boldsymbol{J}) = 0$$

According to charge conversation law, electric current and charge densities have the following relationship.

$$\nabla \cdot \boldsymbol{J} = -\frac{\partial \rho}{\partial t} \tag{4.5}$$

Then

$$\nabla \cdot (\varepsilon \frac{\partial \boldsymbol{E}}{\partial t}) - \frac{\partial \rho}{\partial t} = 0$$

$$\nabla \cdot \boldsymbol{E} = \frac{\rho}{\varepsilon}$$

Based on the above proof, the following numerical simulation of laser propagation will start from the curl equations of electric and magnetic fields Eq. (4.1)-(4.2) as well as charge conversation law Eq. (4.5).

4.3 Yee Algorithm and Discrete Maxwell Equations

In order to numerically calculate Maxwell equations, we firstly need their discrete forms. For the

three dimensional scheme, Eq. (4.1)-(4.2) can be respectively rewritten in the followings.

$$\left.\begin{aligned}\frac{\partial Ez}{\partial y}-\frac{\partial Ey}{\partial z}&=-\mu\frac{\partial Hx}{\partial t}\\ \frac{\partial Ex}{\partial z}-\frac{\partial Ez}{\partial x}&=-\mu\frac{\partial Hy}{\partial t}\\ \frac{\partial Ey}{\partial x}-\frac{\partial Ex}{\partial y}&=-\mu\frac{\partial Hz}{\partial t}\end{aligned}\right\} \tag{4.6}$$

$$\left.\begin{aligned}\frac{\partial Hz}{\partial y}-\frac{\partial Hy}{\partial z}&=\varepsilon\frac{\partial Ex}{\partial t}+Jx\\ \frac{\partial Hx}{\partial z}-\frac{\partial Hz}{\partial x}&=\varepsilon\frac{\partial Ey}{\partial t}+Jy\\ \frac{\partial Hy}{\partial x}-\frac{\partial Hx}{\partial y}&=\varepsilon\frac{\partial Ez}{\partial t}+Jz\end{aligned}\right\} \tag{4.7}$$

With the development of computing technology, the directly numerical calculation of Maxwell equations for propagation of electromagnetic waves becomes a feasible measure. Comparing with other methods, the finite difference time domain method can be used for stable as well as transient problems. In 1966, using the finite difference method Yee [81] got the discrete forms of Maxwell equations having a variable of time in an ingenious mesh system. And problems about interaction between electromagnetic pulses and ideal conductor were solved successfully. This is the origin of name of FDTD: using the finite difference method to solve electromagnetic problems in the time domain.

One Yee cellular is shown in Fig. 4.1, in the cellular components along coordinate axis of electric and magnetic fields are arranged in a staggered mesh system. According to the assignment, every electric/magnetic field component is surrounded by four magnetic/electric field components, which makes the sample mode be automatically satisfied Faraday's law of electromagnetic induction and Ampere circuit law.

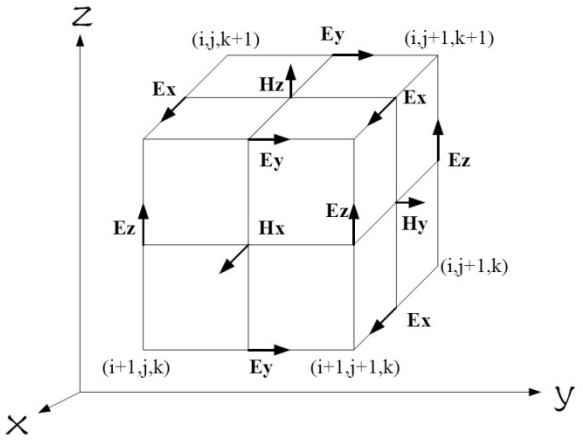

Fig. 4.1 Yee cellular in three dimensional FDTD method.

In a Yee cellular, electric and magnetic field components are alternately sampled, which is suit for discretization of Maxwell curl equations. Besides, in one time step of FDTD, the discrete equations are calculated in two batches. In the firstly time step, the electric/magnetic field is calculated using the magnetic/electric field value obtained in the last time step, then the magnetic/electric field is solved using the latest electric/magnetic field distribution in the last half step. As described explicit algorithm, the Maxwell equations can be solved iteratively without matrix inversion. And according to the above description and content labeled in Fig. 4.1, the electric and magnetic field components can be sampled as Table 3 in the space and time domains.

Table 3 Electric/Magnetic field components in space and time domains.

Electric/Magnetic Fields Component		Sample in Space Domain			Sample in Time Domain
		X	Y	Z	
E	Ex	i+1/2	j	k	n
	Ey	i	j+1/2	k	
	Ez	i	j	k+1/2	
H	Hx	i	j+1/2	k+1/2	n+1/2
	Hy	i+1/2	j	k+1/2	
	Hz	i+1/2	j+1/2	k	

When an electromagnetic wave with a chosen polarization hits an infinite homogeneous dielectric medium, its prorogation can be solved in two dimension. Assuming the medium expands infinitely along the Z-axis in the coordinate system, gradients of all physical quantities in Maxwell equations is zero. When $\partial\phi/\partial z = 0$ is substituted into the above equation sets (4.6)-(4.7), the Maxwell equations in two dimension can be obtained.

$$\frac{\partial Hz}{\partial y} = \varepsilon \frac{\partial Ex}{\partial t} + Jx \tag{4.8}$$

$$-\frac{\partial Hz}{\partial x} = \varepsilon \frac{\partial Ey}{\partial t} + Jy \tag{4.9}$$

$$\frac{\partial Ey}{\partial x} - \frac{\partial Ex}{\partial y} = -\mu \frac{\partial Hz}{\partial t} \tag{4.10}$$

$$\frac{\partial Ez}{\partial y} = -\mu \frac{\partial Hx}{\partial t} \tag{4.11}$$

$$\frac{\partial Ez}{\partial x} = \mu \frac{\partial Hy}{\partial t} \tag{4.12}$$

$$\frac{\partial Hy}{\partial x} - \frac{\partial Hx}{\partial y} = -\varepsilon \frac{\partial Ez}{\partial t} + Jz \tag{4.13}$$

Eqs. (4.8)-(4.13) are independent each other. Eq. (4.8)-(4.10) involves only Ex, Ey and Hz.

Because there is no magnetic-field component along the expanding direction (Z-axis) of infinite medium, Eq. (4.8)-(4.10) is designated the transverse-electric model with respect to Z. Similarly, Eq. (4.11)-(4.13) is generally called transverse-magnetic model with respect to Z because it is only about Hx, Hy and Ez.

Corresponding to TEz/TMz, there are Yee cellular in two dimensions. Take TEz as an example, the Yee cellular as well as electric/magnetic fields components in Yee cellular are shown in Fig. 4.2 and Table 4.

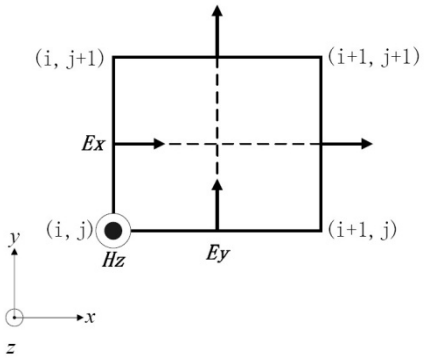

Fig. 4.2 Yee cellular for TEz model in two dimensional FDTD method.

Table 4 Electric/Magnetic fields components in TEz cellular.

Electric/Magnetic Field Component		Sample in Space Domain		Sample in Time Domain
		X	Y	
E	Ex	i	j+1/2	n
	Ey	i+1/2	j	
H	Hz	i	j	n+1/2

Refer to Fig. 4.2 and Table 4, considering a typical substitution of central differences for time and space derivatives into Eq. (4.8), we can have initially

$$\frac{Hz^{n+1/2}(i,j+1)-Hz^{n+1/2}(i,j)}{\Delta y}=\varepsilon\left(i,j+1/2\right)\frac{Ex^{n+1}\left(i,j+1/2\right)-Ex^{n}\left(i,j+1/2\right)}{\Delta t}+Jx^{n}\left(i,j+1/2\right)$$

Then

$$Ex^{n+1}\left(i,j+1/2\right)=Ex^{n}\left(i,j+1/2\right)+\frac{\Delta t}{\varepsilon_0\varepsilon_\gamma\left(i,j+1/2\right)\Delta y}\left(Hz^{n+1/2}(i,j+1)-Hz^{n+1/2}(i,j)\right)-\frac{\Delta t}{\varepsilon_0\varepsilon_\gamma\left(i,j+1/2\right)}Jx^{n}\left(i,j+1/2\right) \tag{4.14}$$

Similarity, discrete forms of Eq. (4.9) and (4.10) can be obtains as

$$Ey^{n+1}(i+1/2,\, j) = Ey^{n}(i+1/2,\, j) - \frac{\Delta t}{\varepsilon_0 \varepsilon_\gamma (i+1/2,\, j)\Delta x}\left(Hz^{n+1/2}\left(i+1,\, j\right) - Hz^{n+1/2}\left(i,\, j\right)\right) - \frac{\Delta t}{\varepsilon_0 \varepsilon_\gamma (i+1/2,\, j)} Jy^{n}(i+1/2,\, j) \tag{4.15}$$

$$Hz^{n+1/2}\left(i,\, j\right) = Hz^{n-1/2}\left(i,\, j\right) - \frac{\mu_0 \mu_\gamma \left(i,\, j\right)\Delta t}{\Delta x}\left(Ey^{n}\left(i+1/2,\, j\right) - Ey^{n}\left(i-1/2,\, j\right)\right) + \frac{\mu_0 \mu_\gamma \left(i,\, j\right)\Delta t}{\Delta y}\left(Ex^{n}\left(i,\, j+1/2\right) - Ex^{n}\left(i,\, j-1/2\right)\right) \tag{4.16}$$

In Eq. (4.14) and (4.15), the relative permittivity has two sampling locations $\left(i, j+1/2\right)$ and $(i+1/2, j)$. While in the coding process, only values of the relative permittivity locate at $\left(i+1/2, j+1/2\right)$ are used for saving the computational expense.Eq. (4.14)-(4.16) is the general calculation method of Yee algorithm for transverse-electric model wave respect to Z (TEz) in two dimensions.

4.4 Boundary Condition in FDTD Method

The size of area that can be simulated using FDTD is limited by computer resources. If the wave is generated in the computational region, as the wave propagates outward, it will eventually come to the edge of the allowable space, which is dictated by how the electromagnetic matrices have been dimensioned in the program. If nothing were done to address this, unpredictable reflections would be generated that would go back inward. These would be no way to determine which is the real wave and which is the reflected junk. In order to eliminate the reflected junk, absorbing boundary conditions is approached. One of the most flexible and efficient ABCs is the perfectly matched layer (PML) developed by Berenger [82]. The principle of PMLABCs can be divided into two sections.

Firstly let waves go into the PML boundaries without reflection. If a wave is propagating in medium A and it impinges upon medium B, the amount of reflection is dictated by the intrinsic impedances of the two media $\Gamma = \left(\eta_A - \eta_B\right)/\left(\eta_A + \eta_B\right)$, which is determined by the permittivity ε and permeability μ of the two media $\eta = \sqrt{\mu/\varepsilon}$. Usually permeability μ was a constant, so when a propagating pulse went among medias with different permittivity ε, it saw a change in impendence and reflected a portion of the pulse. However if permeability μ changed artificially with permittivity ε, η would remain a constant and Γ would be zero and no reflection would occur.

Secondly waves propagating in PBM boundaries can decay to zero within infinite thickness of PBM boundaries. Which is accomplished by making both the permittivity ε and permeability μ be complex， because the imaginary part represents the part that causes decay.

4.5 Incident Wave Source Solutions in FDTD Method

The development of the plane-wave source condition allowed the earliest engineering application of FDTD computational electromagnetic modeling. While in order to correctly source an incident plane wave in the Yee space lattice, the technology must meet the following requirements:

a) The incident wave must have an arbitrary and easily specified propagation direction, polarization, time waveform and duration.

b) The incident wave must have a planar wave-front that is perpendicular to the direction of propagation.

c) The incident wave must have constant amplitude along any plane parallel to the wave-front.

d) The incident wave must be invisible to any scattered numerical waves, allowing them to pass through the wave source with any hindrance or interaction to eventually reach the exterior region.

e) The incident wave must satisfy the requirement of PML absorbing boundary condition that only outward traveling wave collide the interceptive.

As shown in Fig. 4.3, two coordinate systems are organized: one is used for FDTD calculation, and the other one is based on direction of incident plane. The plane wave propagate into the total fields along the direction of y'. The intersection angle between forward direction of y' and x axis is φ_i, so conversion equation of vector from x'-y' to x-y can be obtained.

$$\begin{bmatrix} x \\ y \\ z \end{bmatrix} = \begin{bmatrix} \sin\varphi_i & \cos\varphi_i & 0 \\ -\cos\varphi_i & \sin\varphi_i & 0 \\ 0 & 0 & 1 \end{bmatrix} \begin{bmatrix} x' \\ y' \\ z' \end{bmatrix}$$

For TEz case, values of electromagnetic fields in x'-y' coordinate system is：

$$\begin{bmatrix} Ex' \\ Ey' \\ Ez' \end{bmatrix} = \begin{bmatrix} 0 \\ E_i \\ 0 \end{bmatrix}, \quad \begin{bmatrix} Hx' \\ Hy' \\ Hz' \end{bmatrix} = \begin{bmatrix} 0 \\ 0 \\ E_i / Z \end{bmatrix}$$

So values of $\boldsymbol{E}_{inc}$ and $\boldsymbol{H}_{inc}$ in x-y can be obtained.

$$\begin{cases} Ex = \cos\varphi_i Ey' = \cos\varphi_i E_i \\ Ey = \sin\varphi_i Ey' = \sin\varphi_i E_i \\ Hz = Hz' = E_i / Z \end{cases}$$

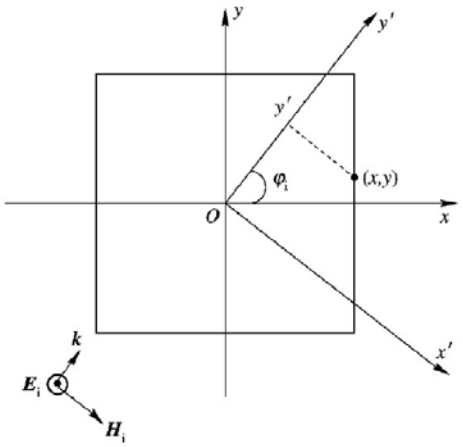

Fig. 4.3 Incident plane wave in FDTD.

4.6 Numerical Dispersion and Stability of FDTD Method

In order to eliminate numerical dispersion in FDTD, the space step must satisfy the following limit.

$$\delta_{\max} \le \frac{\lambda}{12} \tag{4.17}$$

Here λ is wavelength of electromagnetic wave.

In FDTD the time step should satisfy the Conrant Limit. The Counrant stability bound is given in three dimensions by

$$\Delta t \le \Delta t_{\max} = \frac{1}{c\sqrt{\frac{1}{(\Delta x)^2}+\frac{1}{(\Delta y)^2}+\frac{1}{(\Delta z)^2}}}. \tag{4.18}$$

Here c is the speed of light. For two dimensional TEz case, the above equation is

$$\Delta t \le \frac{1}{c\sqrt{\frac{1}{(\Delta x)^2}+\frac{1}{(\Delta y)^2}}}. \tag{4.19}$$

Furthermore, if $\Delta x = \Delta y = \delta$, then $\Delta t \le \frac{\delta}{\sqrt{2}c}$.

4.7 Numerical Results of Two Dimensional Gaussian Beam

4.7.1 Theory of the Gaussian beam

In most laser applications it is necessary to focus, modify, or shape the laser beam by using lenses and other optical elements. In general, laser-beam propagation can be approximated by assuming that the laser beam has an ideal Gaussian intensity profile, corresponding to the theoretical TEM_{00} mode. Gaussian beam is a beam of E/M radiation whose transverse electric field and intensity (irradiance) distributions are well approximated by Gaussian functions. Lots of lasers are

approximated as Gaussian profile shown in Fig. 4.4. It's a convenient, widespread model in laser optics.

The mathematic expression for Gaussian beam is:

$$E(r,z)=E_0\frac{\omega_0}{\omega(z)}\exp\left(-\frac{r^2}{\omega^2(z)}\right)\exp\left(-ik\left(z+\frac{r^2}{2R(z)}\right)+i\xi(z)\right). \tag{4.20}$$

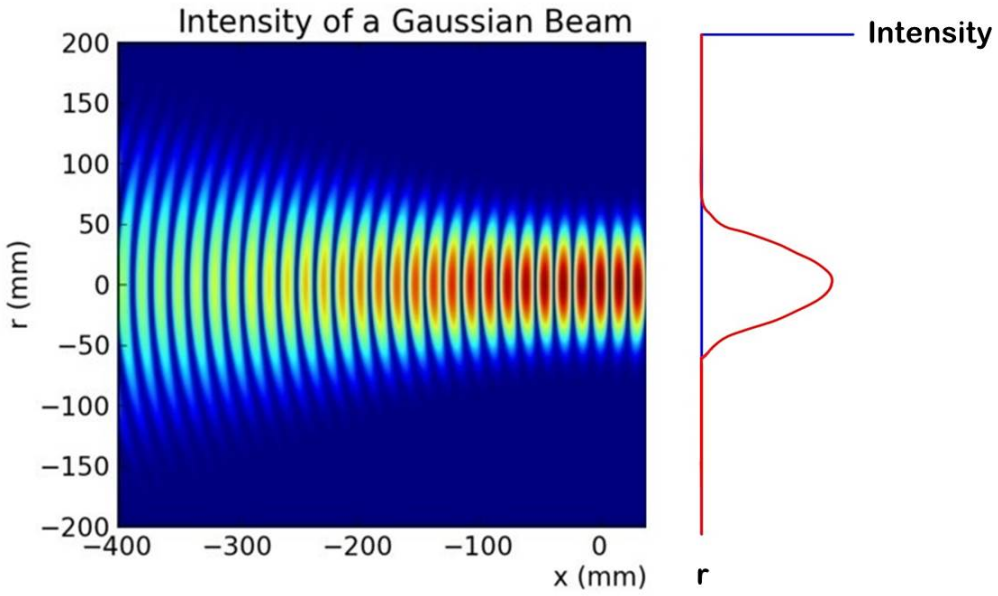

Fig. 4.4 Gaussian beam for simplified laser beam.

Where:

r is the radial distance from the center axis of the beam;

z is the axial distance from the beam's narrowest point (beam waist);

i is the imaginary unit ($i^2=-1$);

$k=2\pi/\lambda$ is the wave number (in radians per meter);

$E_0=\left|E(0,0)\right|$;

$\omega(z)$ is the radius at which the field amplitude and intensity drop to e^{-1} and e^{-2} of their axial values respectively;

$\omega_0=\omega(0)$ is the beam waist;

$R(z)$ is the radius of curvature at the equiphase surface of the beam's wave fronts;

$\xi(z)$ is the Gouy phase shift, an extra contribution to the phase shift in Gaussian beam.

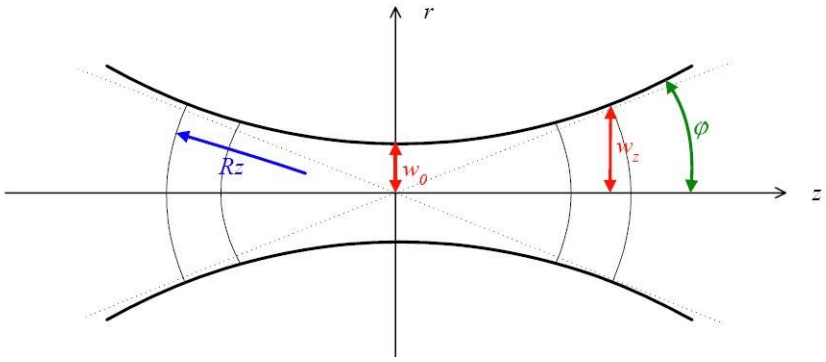

Fig. 4.5 Structure of Gaussian beam.

4.7.2 FDTD for the Gaussian beam

For FDTD coding, we only need the amplitude of E/M fields at each location, and add the time marching term, so rewrite Eq. (4.20) for two-dimensional linearly polarized Gaussian beam shown as Fig. 4.6.

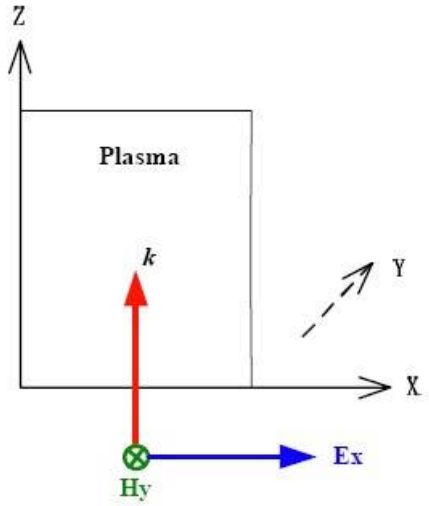

Fig. 4.6 Model of two-dimensional Gaussian beam.

$$Ex(x,z) = E_0 \frac{\omega_0}{\omega(z)} \exp\left(-\frac{x^2}{\omega^2(z)}\right) \sin(\varpi t - \varphi_0), \tag{4.21}$$

or

$$Hy(x,z) = H_0 \frac{\omega_0}{\omega(z)} \exp\left(-\frac{x^2}{\omega^2(z)}\right) \sin(\varpi t - \varphi_0). \tag{4.22}$$

4.7.3 Numerical results

(1) Parameters about Gaussian beam

The used parameters of Gaussian beam and the computational region are shown in Table 5.

Table 5 Parameters of Gaussian beam and the computational region.

Laser	Wavelength	10.64 μm
	Intensity	1.25×10^{7} $W\cdot cm^{-2}$
Computational Region	size	135.68×135.68 μm^{2}
	Mesh step	0.53 μm
	Time step	$\Delta x/2c$

(2) Unfocused Gaussian beam

The simulation results of unfocused and continuous Gaussian beam is shown in Fig. 4.7. In this simulation the laser source is set along the bottom line of the computational region. The positive and negative electric field can be clearly seen in Fig. 4.7(a).

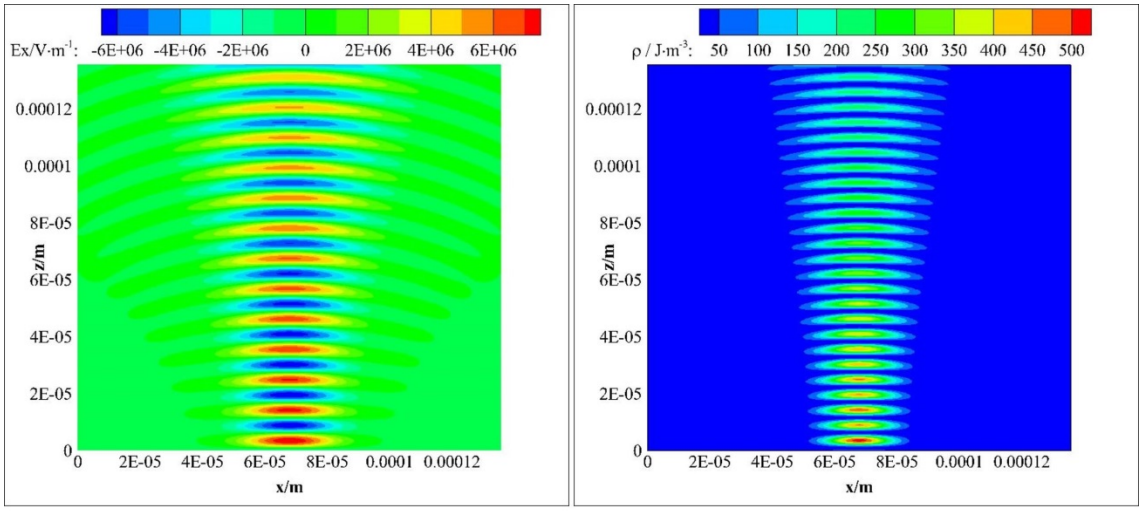

Fig. 4.7 Electric field and energy density of the unfocused Gaussian beam.

(3) Continuous Gaussian beam

The simulation results of continuous and focus Gaussian beam is shown in Fig. 4.8. The difference of this simulation compared with the last simulation is that one equiphase surface is added in the laser source. As shown as Fig. 4.8, the laser beam is focused at the center of the computational region where the electric field intensity and the energy density have their maximum values.

(4) Pulsed Gaussian beam

Gaussian pulse in the time domain can be modeled as

$$f(t)=aExp\left(-\frac{(t-b)^2}{c^2}\right). \tag{4.23}$$

Where a is the height of the curve's peak, b is the position of the center of the peak, c controls the width of the curve, when $t-b=\pm c$, the electromagnetic field drop to e^{-1}. And the

pulse width is $t_p = 2c$.

Fig. 4.10 and Fig. 4.9 show simulation results of artificial pulsed Gaussian beam with pulse width of 1 ps. And the electromagnetic field at the source line has its maximum value at 2 ps. In Fig. 4.9, the maximum values of energy density and intensity at the focus spot do not reach at 2 ps, and the gap is the needed time interval when the Gaussian beam propagates from its source to the focus spot. Fig. 4.10 illustrates the energy distributions variation with time.

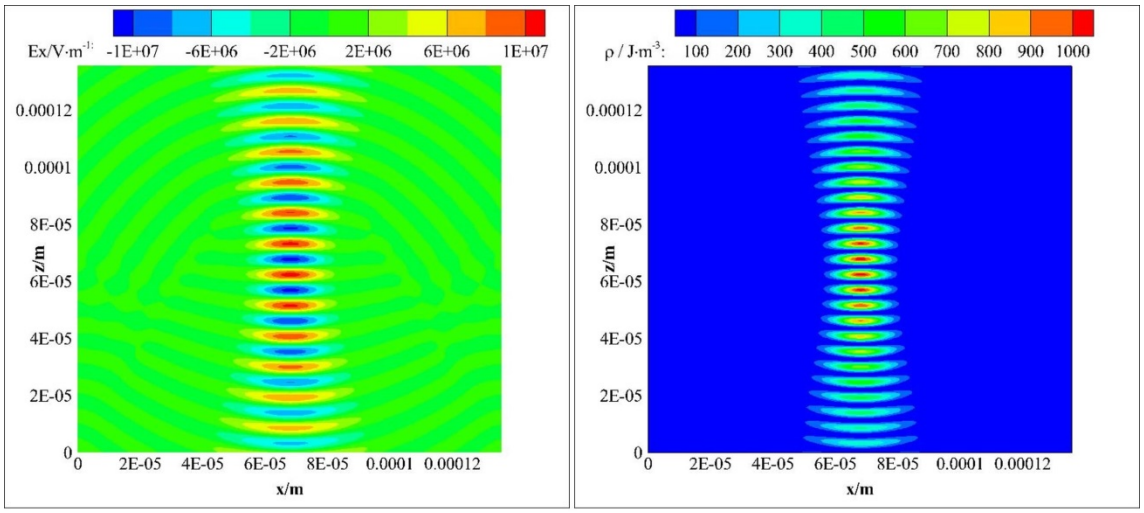

Fig. 4.8 Electric field and energy density of the focused Gaussian beam.

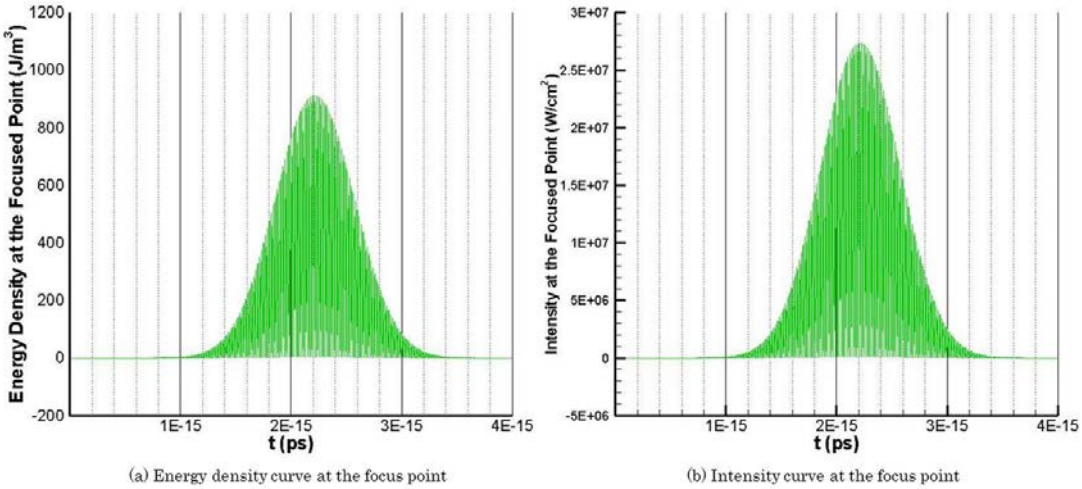

Fig. 4.9 Energy density and intensity curves at the focus point of pulsed Gaussian beam.

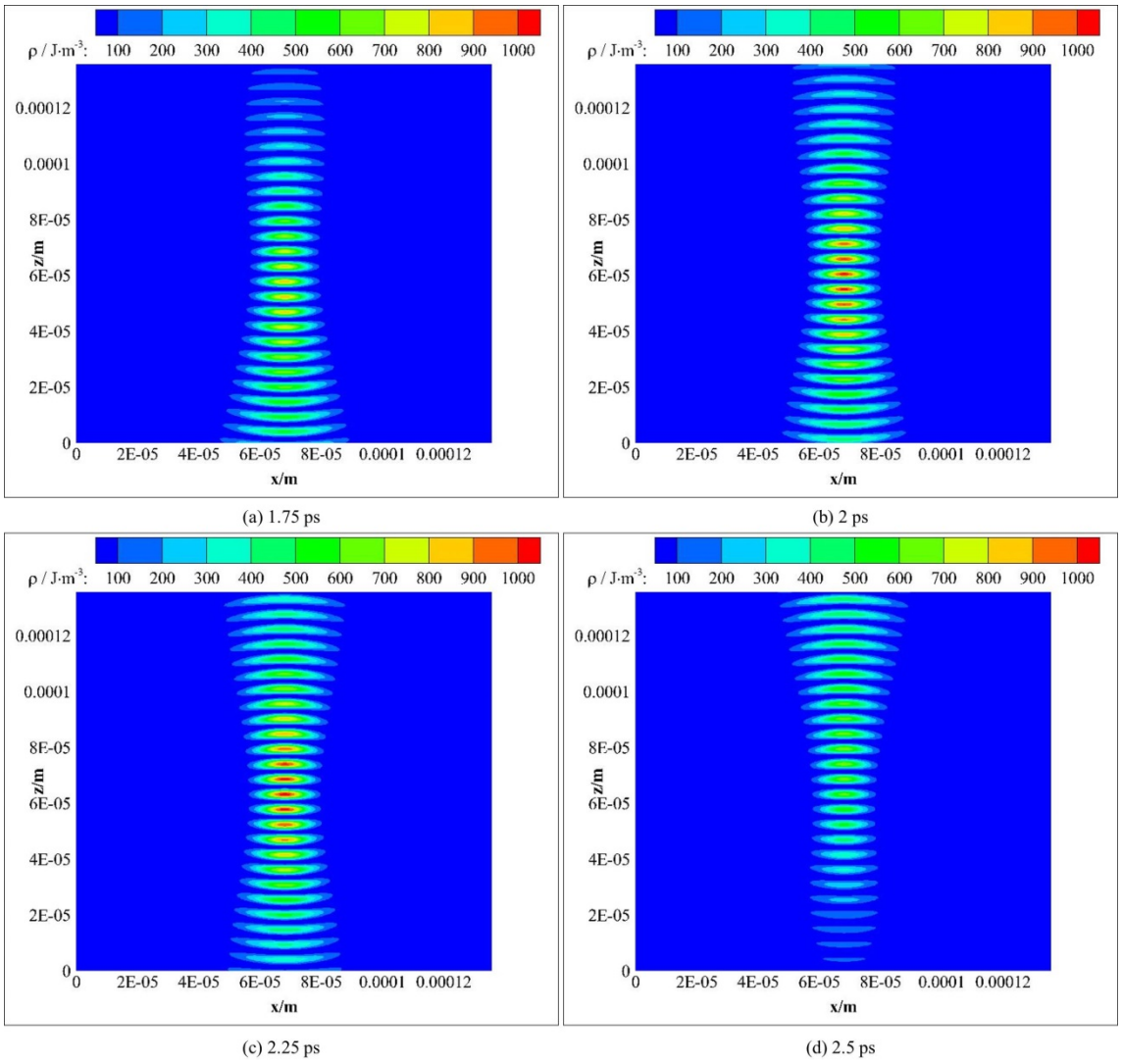

Fig. 4.10 Energy densities of focused Gaussian beam at 1.75ps, 2ps, 2.25ps and 2.75ps.

CHAPTER 5. THE LATTICE BOLTZMANN METHOD AND ITS APPLICATION FOR PLASMA

5.1 Gas Kinetic Theory and the Boltzmann Equation

5.1.1. The Boltzmann equation

Gas is a system containing a very large number of interacting particles, so that for its analysis it is appropriate and convenient to use statistical approach. Each particle in gas can be localized by a position vector $\boldsymbol{r} = x\boldsymbol{i} + y\boldsymbol{j} + z\boldsymbol{k}$ drawn from the origin of a coordinate system to the center of mass of the particle. Position coordinates (x, y, z) is defined as the configuration space. Analogy with configuration space, the linear velocity of the center of mass of the particle can be represented by the vector $\boldsymbol{v} = v_x\boldsymbol{i} + v_y\boldsymbol{j} + v_z\boldsymbol{k}$. And the velocity space is defined by the velocity coordinates (v_x, v_y, v_z). In gas kinetics, six coordinates (x, y, z, v_x, v_y, v_z) is defined as the phase space. In this six-dimensional space the dynamic state of each particle is appropriately represented by a single point. The coordinated $(\boldsymbol{r}, \boldsymbol{\upsilon})$ of the represented point in the phase space give the position and velocity of the particle. When the particle moves, its representative point describes a trajectory in phase space.

A differential element of the volume in the phase space is represented by $d^3rd^3v = dxdydzdv_xdv_ydv_z$. Inside d^3rd^3v at the position $(\boldsymbol{r}, \boldsymbol{v})$ in the phase space, there only the particles inside d^3r around $\boldsymbol{r}$ whose velocities lie inside d^3v about $\boldsymbol{v}$. The coordinates $\boldsymbol{r}$ and $\boldsymbol{v}$ of the phase space are independent variables.

Let $d^6N_a(\boldsymbol{r}, \boldsymbol{v}, t)$ denote the number of type *a* inside the volume element d^3rd^3v around the phase space coordinate $(\boldsymbol{r}, \boldsymbol{v})$ at the instant *t*. The distribution function in gas kinetics, $f_a(\boldsymbol{r}, \boldsymbol{v}, t)$, is defined as the density of representative points of the type *a* particles in phase space.

$$f_a(\boldsymbol{r}, \boldsymbol{v}, t) = \frac{d^6N_a(\boldsymbol{r}, \boldsymbol{v}, t)}{d^3rd^3v} \tag{5.1}$$

Using the distribution function, the usual statistical definitions of number density and average velocity can be obtained.

$$n_a(\boldsymbol{r}, t) = \frac{1}{d^3r}\int_v d^6N_a(\boldsymbol{r}, \boldsymbol{v}, t) = \int_v f_a(\boldsymbol{r}, \boldsymbol{v}, t)d^3v \tag{5.2}$$

$$\boldsymbol{u}_a(\boldsymbol{r}, t) = \frac{1}{n_a(\boldsymbol{r}, t)d^3r}\int_v \boldsymbol{v}\, d^6N_a(\boldsymbol{r}, \boldsymbol{v}, t) = \frac{1}{n_a(\boldsymbol{r}, t)}\int_v \boldsymbol{v}\, f_a(\boldsymbol{r}, \boldsymbol{v}, t)d^3v \tag{5.3}$$

One of the primary problems of kinetic theory consists in determining the distribution function for a given system. The differential equation that governs the temporal and spatial variation of the

distribution function under given conditions is known generally as the Boltzmann equation.

" $f_a(\boldsymbol{r},\boldsymbol{v},t)d^3rd^3v$ " represents the number of particles of type "*a*" at instant "*t*" within the volume $d^3r\,d^3v$ of the phase space about the coordinates $(\boldsymbol{r},\boldsymbol{v})$. Suppose that each particle is subjected to the external force $\boldsymbol{F}$. In the absence of particle interactions, particles will migrate and be accelerated. A particle of type "*a*" with coordinate about $(\boldsymbol{r},\boldsymbol{v})$ at instant "*t*" will be found after a time interval "*dt*" about the new coordinate $(\boldsymbol{r}',\boldsymbol{v}')$ such that $\boldsymbol{r}'(t+dt)=\boldsymbol{r}'(t)+\boldsymbol{v}dt$ and $\boldsymbol{v}'(t+dt)=\boldsymbol{v}(t)+\boldsymbol{F}dt/m_a$. Thus all particle of type "*a*" inside the volume element $d^3r\,d^3v$ of the phase space about $(\boldsymbol{r},\boldsymbol{v})$ at instant "*t*" will occupy a new volume element $d^3r'\,d^3v'$ about $(\boldsymbol{r}',\boldsymbol{v}')$ after the interval "*dt*". So the following equation can be obtained.

$f_a(\boldsymbol{r}',\boldsymbol{v}',t+dt)d^3r'd^3v'=f_a(\boldsymbol{r},\boldsymbol{v},t)d^3rd^3v$

While when the effects due to particle interactions are taken into account, the above equation needs to be modified. As a result of collisions during the time interval "*t*", some of the particles of type "*a*" that were initially with the volume element $d^3r\,d^3v$ of phase space may be removed from it. And particles of type "*a*" outside this volume element may end up inside it. Generally, the number of particles of type "*a*" inside $d^3r\,d^3v$ about the coordinate $(\boldsymbol{r},\boldsymbol{v})$ at instant "*t*" will be different from the number of particle of type "*a*" inside $d^3r'\,d^3v'$ about the coordinate $(\boldsymbol{r}',\boldsymbol{v}')$ at instant "*t+dt*". This net gain or lose can be denoted as $\left[\delta f_a(\boldsymbol{r},\boldsymbol{v},t)/\delta t\right]_{coll}d^3rd^3vdt$. The equation can be modified as following.

$$f_a(\boldsymbol{r}',\boldsymbol{v}',t+dt)d^3r'd^3v'-f_a(\boldsymbol{r},\boldsymbol{v},t)d^3rd^3v=\left[\frac{\delta f_a(\boldsymbol{r},\boldsymbol{v},t)}{\delta t}\right]_{coll}d^3rd^3vdt \tag{5.4}$$

As a result of the particle motion, the element of volume $d^3r\,d^3v$ may be distorted in shape. The relation between the new element of volume and the initial one is given by

$$d^3r'\,d^3v'=\left|\boldsymbol{J}\right|d^3r\,d^3v$$

where **J** stands for the Jacobian of the transform from the initial coordinate $d^3r\,d^3v$ to the final one $d^3r'\,d^3v'$. Neglecting terms of the order $(dt)^2$, it can be easily verified that $\left|\boldsymbol{J}\right|=1$ [83].

$$\left[f_a(\boldsymbol{r}',\boldsymbol{v}',t+dt)-f_a(\boldsymbol{r},\boldsymbol{v},t)\right]d^3rd^3v=\left[\frac{\partial f_a(\boldsymbol{r},\boldsymbol{v},t)}{\partial t}\right]_{coll}d^3rd^3vdt$$

The first term on the left-hand side of the above equation can be expanded in a Taylor series about $f_a(\boldsymbol{r},\boldsymbol{v},t)$ as followings neglecting terms of order and higher.

$$\begin{aligned}f_a(\boldsymbol{r}',\boldsymbol{v}',t+dt)&=f_a(\boldsymbol{r}+\boldsymbol{v}dt,\boldsymbol{v}+\boldsymbol{a}dt,t)\\&=f_a(\boldsymbol{r},\boldsymbol{v},t)+\left[\frac{\partial f_a}{\partial t}+\left(v_x\frac{\partial f_a}{\partial x}+v_y\frac{\partial f_a}{\partial y}+v_z\frac{\partial f_a}{\partial z}\right)+\left(a_x\frac{\partial f_a}{\partial v_x}+a_y\frac{\partial f_a}{\partial v_y}+a_z\frac{\partial f_a}{\partial v_z}\right)\right]dt\end{aligned}$$

Using the ∇ operator notation, the above equation is changed to

$$f_a(\boldsymbol{r}',\boldsymbol{v}',t+dt)=f_a(\boldsymbol{r},\boldsymbol{v},t)+\left[\frac{\partial f_a(\boldsymbol{r},\boldsymbol{v},t)}{\partial t}+\boldsymbol{v}\cdot\nabla f_a(\boldsymbol{r},\boldsymbol{v},t)+\boldsymbol{a}\cdot\nabla_v f_a(\boldsymbol{r},\boldsymbol{v},t)\right]dt$$

Substituting this result into Eq. (5.4) gives the famous Boltzmann equation.

$$\frac{\partial f_a(\boldsymbol{r},\boldsymbol{v},t)}{\partial t}+\boldsymbol{v}\cdot\nabla f_a(\boldsymbol{r},\boldsymbol{v},t)+\boldsymbol{a}\cdot\nabla_v f_a(\boldsymbol{r},\boldsymbol{v},t)=\left[\frac{\delta f_a(\boldsymbol{r},\boldsymbol{v},t)}{\delta t}\right]_{coll} \tag{5.5}$$

5.1.2. The H-theorem and equilibrium distribution function

In order to solve the Boltzmann equation, the calculation of net variation of distribution function caused by particle interactions is vital. Here molecular chaos is used: (a) the gas is assumed to be sufficiently dilute that only binary collisions are taken into account. (b) The velocities of the colliding molecules are assumed to be statistically independent. Any possible correlations between the velocity and position of any single molecule are also neglect. (c) The phase space distribution function does not vary appreciably during the brief time interval of molecular collision, nor does it change significantly over spatial scales comparable to the range of intermolecular forces. The net change of distribution function is a result of two competing processes. First the molecules in d^3r can be scattered out of this velocity range as a result of collisions with other molecules. Secondly molecule in d^3r whose velocity is originally not between $\boldsymbol{v}$ and $\boldsymbol{v}+d\boldsymbol{v}$ can be scattered into the specified velocity range.

Considering molecular encounters taking place in the configuration space volume element d^3r between a molecule, whose post collision velocity is $\boldsymbol{v}'$, in the velocity range $\boldsymbol{v}\sim\boldsymbol{v}+d\boldsymbol{v}$ and all other molecules whose initial and final velocities are denoted by $\boldsymbol{v}_2$ and $\boldsymbol{v}_2'$. The collision term in the Boltzmann equation can be obtained [84].

$$\left[\frac{\delta f_a(\boldsymbol{r},\boldsymbol{v},t)}{\delta t}\right]_{coll}=\int_{\infty}d\boldsymbol{v}_2\int_0^{2\pi}d\varepsilon\int_0^{\pi}d\chi\sin\chi S(g,\chi)g\left[f(\boldsymbol{r},\boldsymbol{v}',t)f(\boldsymbol{r},\boldsymbol{v}_2',t)-f(\boldsymbol{r},\boldsymbol{v},t)f(\boldsymbol{r},\boldsymbol{v}_2,t)\right] \tag{5.6}$$

where ε is the impact azimuths, χ is the deflection angle, g is again the magnitude of the relative velocity and $S(g,\chi)$ is the cross section.

The Boltzmann H-theorem shows when $f(\boldsymbol{r},\boldsymbol{v},t)$ satisfies the Boltzmann equation, the Boltzmann function decrease monotonically until it reach reaches a limiting value, which occurs when there is no further change in the system. This limiting value is reached only when $f(\boldsymbol{r},\boldsymbol{v}',t)f(\boldsymbol{r},\boldsymbol{v}_2',t)=f(\boldsymbol{r},\boldsymbol{v},t)f(\boldsymbol{r},\boldsymbol{v}_2,t)$ and the limiting condition is caused equilibrium state. Phase space distribution function in equilibrium state is denoted by $f^{eq}(\boldsymbol{r},\boldsymbol{v},t)$.

To satisfy $f(\boldsymbol{r},\boldsymbol{v}',t)f(\boldsymbol{r},\boldsymbol{v}_2',t)=f(\boldsymbol{r},\boldsymbol{v},t)f(\boldsymbol{r},\boldsymbol{v}_2,t)$, the logarithmic function of phase space distribution function $\ln f(\boldsymbol{r},\boldsymbol{v},t)$ must be linear combination of collision invariants [85]: molecular mass "m", molecular momentum "$m\boldsymbol{v}$" and molecular energy "$m\boldsymbol{v}^2/2$". At last the equilibrium distribution function, named Maxwell-Boltzmann distribution function can be

obtained.

$$f^{eq}(\boldsymbol{r},\boldsymbol{v},t)=\frac{n}{(2\pi RT)^{D/2}}\exp\left[-\frac{(\boldsymbol{v}-\boldsymbol{u})^2}{2RT}\right] \tag{5.7}$$

5.1.3. The BGK collision model

The main difficulty to solve Boltzmann equation is because of the collision term. BGK collision model is one famous simplified collision model. In 1954, Bhatnagar, Gross and Krook [86] used the relaxation model to take the place of complex collisions to restore a situation of local equilibrium. The model assumes that a situation initially not in equilibrium, described by a distribution function $f(\boldsymbol{r},\boldsymbol{v},t)$ different from $f^{eq}(\boldsymbol{r},\boldsymbol{v},t)$, reaches a local equilibrium condition exponentially with time with a relaxation time τ.

$$\left[\frac{\delta f_a(\boldsymbol{r},\boldsymbol{v},t)}{\delta t}\right]_{coll}=-\frac{f_a(\boldsymbol{r},\boldsymbol{v},t)-f_a^{eq}(\boldsymbol{r},\boldsymbol{v},t)}{\tau}$$

When the BGK collision is substituted into Boltzmann equation, the modified equation is called Boltzmann-BGK equation.

$$\frac{\partial f(\boldsymbol{r},\boldsymbol{v},t)}{\partial t}+\boldsymbol{v}\cdot\nabla f(\boldsymbol{r},\boldsymbol{v},t)+\boldsymbol{a}\cdot\nabla_v f(\boldsymbol{r},\boldsymbol{v},t)=-\frac{f(\boldsymbol{r},\boldsymbol{v},t)-f^{eq}(\boldsymbol{r},\boldsymbol{v},t)}{\tau} \tag{5.8}$$

For plasma, the Boltzmann-BGK equation is particularly applicable to weakly ionized plasma in which only charge-neutral collisions are important. However it oversimplifies the entire relaxation phenomena and does not predict correctly the different relaxation collision frequencies for the various physical quantities of interest, such as the macroscopic velocity, momentum and energy. According to the relaxation model, these macroscopic physical variables approach equilibrium at the same speed. A detailed analysis of the collision process, however, shows that this is not the case, and the relaxation times for the various macroscopic variables differ to some extent. The relaxation model is therefore strictly applicable only to the case of collisions between particles of the same mass. In spite of this limitation, the relaxation model is still useful partly because of its simplicity and partly because it usually gives a first approximation to the problem under consideration.

5.2 The Boltzmann-BGK Equation and Lattice Boltzmann Method

5.2.1 Derivation process of LBGK equation

The lattice Boltzmann method is a numerical solution method of Boltzmann-BGK equation. The discrete Boltzmann-BGK equation includes discrete velocity space, discrete configuration space and discrete time progress. The lattice Boltzmann method is derived from lattice gas automata [87]. But derivation have directly connected the lattice Boltzmann equation to the Boltzmann equation [88, 89]; the framework of the lattice Boltzmann equation can rest on that of the Boltzmann

equation and the rigorous results of the Boltzmann equation can be extended to the lattice Boltzmann equation. Here the discrete Boltzmann-BGK equation in two dimensions without external force term is taken as to example to show its derivation from continuous Boltzmann-BGK equation. The models for the force term will be introduced later.

Molecules are in chaotic thermal motion all the time, so the molecular velocity space is continuous and the velocity is infinite dimensions in the velocity space. In order to discretely solve Boltzmann-BGK equation, the velocity is simplified as $\{\boldsymbol{v}_0, \boldsymbol{v}_1, \boldsymbol{v}_2, \cdots, \boldsymbol{v}_n\}$, and the discrete distribution function is as $\{f_0(\boldsymbol{r}, \boldsymbol{v}_0, t), \cdot f_1(\boldsymbol{r}, \boldsymbol{v}_1, t), f_2(\boldsymbol{r}, \boldsymbol{v}_2, t), \cdots, f_n(\boldsymbol{r}, \boldsymbol{v}_n, t)\}$. Then the Boltzmann-BGK equation in discrete velocity space is as followings.

$$\frac{\partial f_\alpha(\boldsymbol{r}, \boldsymbol{v}_\alpha, t)}{\partial t} + \boldsymbol{v}_\alpha \cdot \nabla f_\alpha(\boldsymbol{r}, \boldsymbol{v}_\alpha, t) = -\frac{f_\alpha(\boldsymbol{r}, \boldsymbol{v}_\alpha, t) - f_\alpha^{eq}(\boldsymbol{r}, \boldsymbol{v}_\alpha, t)}{\tau} \quad (\alpha = 0,1,2,\cdots,n) \tag{5.9}$$

$f_\alpha^{eq}(\boldsymbol{r}, \boldsymbol{v}_\alpha, t)$ is the discrete distribution function in discrete phase space and can be derived from the Maxwell-Boltzmann distribution equation.

$$\begin{aligned} f_\alpha^{eq}(\boldsymbol{r}, \boldsymbol{v}_\alpha, t) &= \frac{n}{(2\pi RT)^{D/2}} \exp\left[-\frac{(\boldsymbol{v}_\alpha - \boldsymbol{u})^2}{2RT}\right] \\ &= \frac{n}{(2\pi RT)^{D/2}} \exp\left[-\frac{\boldsymbol{v}_\alpha{}^2 - 2\boldsymbol{v}_\alpha \cdot \boldsymbol{u} + u^2}{2RT}\right] \\ &= \frac{n}{(2\pi RT)^{D/2}} \exp\left[-\frac{\boldsymbol{v}_\alpha{}^2}{2RT}\right] \exp\left[\frac{2\boldsymbol{v}_\alpha \cdot \boldsymbol{u} - u^2}{2RT}\right] \\ &= \frac{n}{(2\pi RT)^{D/2}} \exp\left[-\frac{\boldsymbol{v}_\alpha{}^2}{2RT}\right]\left[1 + \frac{\boldsymbol{v}_\alpha \cdot \boldsymbol{u}}{RT} - \frac{(\boldsymbol{v}_\alpha \cdot \boldsymbol{u})^2}{2R^2T^2} - \frac{u^2}{2RT}\right] + O(\boldsymbol{u}^3) \\ &= n\omega_\alpha\left[1 + \frac{\boldsymbol{v}_\alpha \cdot \boldsymbol{u}}{RT} - \frac{(\boldsymbol{v}_\alpha \cdot \boldsymbol{u})^2}{2R^2T^2} - \frac{u^2}{2RT}\right] + O(\boldsymbol{u}^3) \end{aligned} \tag{5.10}$$

where $\omega_\alpha = \frac{1}{(2\pi RT)^{D/2}} \exp\left[-\frac{\boldsymbol{v}_\alpha{}^2}{2RT}\right]$ is the statistical weight.

In order to numerically calculation Eq. (5.9), the discrete configuration space and the discrete time are necessary. At last, the completely Boltzmann equation in discrete phase space is obtained, named by the lattice Boltzmann-BGK equation.

$$f_\alpha(\boldsymbol{r} + \boldsymbol{v}_\alpha \delta t, t + \delta t) - f_\alpha(\boldsymbol{r}, t) = -\frac{f_\alpha(\boldsymbol{r}, t) - f_\alpha^{eq}(\boldsymbol{r}, t)}{\tau/\delta t} \quad (\alpha = 0,1,2,\cdots,n) \tag{5.11}$$

5.2.2 LBM model and discrete Boltzmann equation

As the above derivation process, the discrete velocity space, the discrete equilibrium function as well as lattice Boltzmann equation are together named lattice Boltzmann model. For different

purposes, there are many lattice Boltzmann models, such as single component single phase lattice Boltzmann model, single component, multiphase lattice Boltzmann model, multicomponent multiphase lattice Boltzmann model, incompressible model and compressible model. In 1992, model DdQm(d-dimensions, m-discrete velocities) [90] is the fundamental model of lattice Boltzmann method. Model D2Q9 is one of them.

The discrete velocity space of model D2Q9 is:

$$\boldsymbol{v}_\alpha = \begin{cases} 0 & \alpha = 0 \\ c\left(\cos\left[(\alpha-1)\dfrac{\pi}{2}\right], \sin\left[(\alpha-1)\dfrac{\pi}{2}\right]\right) & \alpha = 1,2,3,4 \\ c\left(\cos\left[(\alpha-1)\dfrac{\pi}{2}+\dfrac{\pi}{4}\right], \sin\left[(\alpha-1)\dfrac{\pi}{2}+\dfrac{\pi}{4}\right]\right) & \alpha = 5,6,7,8 \end{cases} \tag{5.12}$$

where $c = \delta x/\delta t$, δx and δt are space and time steps respectively.

The discrete equilibrium distribution function is

$$f_\alpha^{eq}(\boldsymbol{r},\boldsymbol{v}_\alpha,t) = n\omega_\alpha\left[1+\frac{\boldsymbol{v}_\alpha\cdot\boldsymbol{u}}{RT}-\frac{(\boldsymbol{v}_\alpha\cdot\boldsymbol{u})^2}{2R^2T^2}-\frac{u^2}{2RT}\right] \tag{5.13}$$

and $\omega_0 = 4/9, \omega_{1\sim4} = 4/9, \omega_{5\sim9} = 4/9$.

The lattice Boltzmann equation for model D2Q9 is Eq. (5.13).

5.2.3 Force term

In Boltzmann equation, the effect of the external force to the distribution function is expressed by $\boldsymbol{a}\cdot\nabla_v f(\boldsymbol{r},\boldsymbol{v},t)$. But in LBM this term cannot be calculated directly as a result of the discrete velocity space, so it is necessary to develop alternative methods to evaluate the external force.

The first kind of measure to model the discrete external force term is correction of the equilibrium distribution function. Shan and Chen [91] , named by Shan-Chen model, tried to change the macroscopic velocity in the equilibrium distribution function to model the effect of external force to particle movement. In lattice Boltzmann-BGK equation, the time interval among twice particle migration is τ , so the velocity variation in this time interval is $\boldsymbol{a}\tau$, so Shan and Chen used $\boldsymbol{u} = \boldsymbol{u} + \boldsymbol{a}\tau$ in the equilibrium distribution function calculation process, but the fluid macroscopic velocity in statistic process is still as $\boldsymbol{u} = \sum_i \boldsymbol{v}_i f_i \Big/ n$. Later Shan-Doolen model [92] redressed the macroscopic velocity calculation equation $\boldsymbol{u} = \frac{1}{n}\left[\left(1-\frac{1}{\tau}\right)\sum_i \boldsymbol{v}_i f_i + \frac{1}{\tau}\sum_i \boldsymbol{v}_i f_i^{eq}\right]$. But strict theoretical works by Guo [93] showed that these two models are only suitable for constant force.

The other kind of scheme for external force term is to adding a discrete force term in lattice

Boltzmann-BGK equation.

$$f_\alpha(\boldsymbol{r}+\boldsymbol{v}_\alpha\delta t,t+\delta t)-f_\alpha(\boldsymbol{r},t)=-\frac{f_\alpha(\boldsymbol{r},t)-f_\alpha^{eq}(\boldsymbol{r},t)}{\tau/\delta t}+\delta t F_\alpha\ (\alpha=0,1,2,\cdots,n) \tag{5.14}$$

Here $F_\alpha(\alpha=0,1,2,\cdots,n)$ is a function about the external force vector. The first and simplest model was derived from the lattice gas automata by He [94]. The discrete force F_α is taken as $F_\alpha=\omega_\alpha\frac{n\boldsymbol{v}_\alpha\cdot\boldsymbol{a}}{RT}$, where $\boldsymbol{a}$ is the particle acceleration due to the external force, and the velocity used in equilibrium was macroscopic velocity or the average velocity $\boldsymbol{u}=\frac{1}{n}\sum_i\boldsymbol{v}_i f_i+\frac{1}{2}\boldsymbol{a}\delta t$. This model is suitable for the case where the spatial and temporal gradient of the external force is negligible, so it is always applied for the flows under a constant body force, such as constant pressure gradient and gravity.

The most famous model for the external force is built by He, Shan and Doolen [95]. The distribution function in the external force term is substituted by the equilibrium distribution function.

$$\begin{aligned}&\boldsymbol{a}\cdot\nabla_v f(\boldsymbol{r},\boldsymbol{v},t)\\&\approx\boldsymbol{a}\cdot\nabla_v f^{eq}(\boldsymbol{r},\boldsymbol{v},t)\\&=\boldsymbol{a}\cdot\frac{\partial}{\partial\boldsymbol{v}}\left(\frac{n}{2\pi RT}\exp\left[-\frac{(\boldsymbol{v}-\boldsymbol{u})^2}{2RT}\right]\right)\\&=-\frac{n}{RT}\boldsymbol{a}\cdot(\boldsymbol{v}-\boldsymbol{u})f^{eq}(\boldsymbol{r},\boldsymbol{v},t)\end{aligned} \tag{5.15}$$

When the discrete equilibrium distribution function is used in this model, the discrete force term in Eq. (5.14) can be obtained.

$$F_\alpha=-\frac{n}{RT}\boldsymbol{a}\cdot(\boldsymbol{v}-\boldsymbol{u})f_\alpha^{eq}(\boldsymbol{r},\boldsymbol{v}_\alpha,t) \tag{5.16}$$

Besides, the macroscopic velocity used for the equilibrium distribution function in this model should be $\boldsymbol{u}=\frac{1}{n}\sum_i\boldsymbol{v}_i f_i+\frac{1}{2}\boldsymbol{a}\delta t$.

Luo [96] derived the discrete force term from second velocity momentum equation of continuous external force term. After modification by Martys, Ladd and Verberg, the common form of the discrete force is as follows.

$$\boldsymbol{F}_i=\omega_i\left[\frac{\boldsymbol{B}\cdot\boldsymbol{v}_i}{RT}+\frac{\boldsymbol{C}:(\boldsymbol{v}_i\boldsymbol{v}_i-RT\boldsymbol{I})}{2R^2T^2}\right] \tag{5.17}$$

B and **C** are functions of the external force. This kind of model has strict theoretical derivation, but by Chapman-Enskog analysis it has the similar application limitation [93]. One special emphasis is that Guo [97] also got a correctional discrete force term. While the performance is almost same

with He-Shan-Doolen model, thus Guo's work gives theoretical foundation to He-Shan-Doolen model. By Chapman-Enskog analysis, lattice Boltzmann-BKG equation can recover Navier-Stokes with truncation error of $O(u^3)$. Is this research, He-Shan-Doolen model is chosen for the external force term.

5.3 The Lattice Boltzmann Method for Laser-Induced Plasma

5.3.1 Continuous Boltzmann equations for plasma

Plasma is a system containing a very large number of interacting charged particles, so that for its analysis it is appropriate and convenient to use statistical approach. Plasma is consisted of several kinds of particles, thus the Boltzmann equation can be used for evolution of each kind. Taken argon plasma as an example, it mainly contains electrons, ions of one positive charge and argon neutrals. The Boltzmann transport equation for argon plasma can be written as follows:

$$\frac{\partial f_s(\boldsymbol{r},\boldsymbol{v}_s,t)}{\partial t}+\boldsymbol{v}_s\cdot\nabla f_s(\boldsymbol{r},\boldsymbol{v}_s,t)+\boldsymbol{a}_s\cdot\nabla_v f_s(\boldsymbol{r},\boldsymbol{v}_s,t)=\left[\frac{\delta f_s(\boldsymbol{r},\boldsymbol{v}_s,t)}{\delta t}\right]_{coll}+\Delta f_s(\boldsymbol{r},\boldsymbol{v}_s,t). \tag{5.18}$$

The subscript s denotes the type of particles and can take e, i and n for electrons, ions and neutrals respectively. $\left[\frac{\delta f_s(\boldsymbol{r},\boldsymbol{v}_s,t)}{\delta t}\right]_{coll}$ denotes collisions among particles. $\Delta f_s(\boldsymbol{r},\boldsymbol{v}_s,t)$ denotes particle distribution function change for particle generation or vanish by ionization or recombination reactions.

Particles interaction in plasma consist elastic collisions with neutrals as well as Coulomb collisions between charged particles. In Li's work [48], only the elastic collisions with neutrals are considered as approximation for laser interaction with weakly ionized helium plasma. As improvement of Li' model, Chen [98] presented a FDTD-LBM model for electromagnetic wave propagation in weakly ionized hydrogen plasmas, which consists of elastic collision terms between molecules, Coulomb collision terms between charged particles, kinetics collision, and force models in multicomponent schemes and multi-scale lattice technique for matching FDTD to LBM. This research mainly considers plasma generation process by laser irradiation. Because ionization rate is very low in plasma generation process, elastic collisions with neutrals undoubtedly dominate particle interaction. Thus the collision term can be replaced by binary collision term with neutrals used in Li's model:

$$\left[\frac{\delta f_s(\boldsymbol{r},\boldsymbol{v}_s,t)}{\delta t}\right]_{coll}=-\frac{f_s(\boldsymbol{r},\boldsymbol{v}_s,t)-f_{sn}^{eq}(\boldsymbol{r},\boldsymbol{v}_s,t)}{\tau_{sn}}. \tag{5.19}$$

$f_{sn}^{eq}(\boldsymbol{r},\boldsymbol{v}_s,t)$ is the equilibrium distribution function of particle s due to collisions with neutrals and can take $f_{en}^{eq}(\boldsymbol{r},\boldsymbol{v}_e,t)$, $f_{in}^{eq}(\boldsymbol{r},\boldsymbol{v}_i,t)$, $f_{nn}^{eq}(\boldsymbol{r},\boldsymbol{v}_n,t)$ for electron-neutral, ion-neutral and neutral-neutral collisions respectively. τ_{sn} can take τ_{en}, τ_{in}, τ_{nn} denoting the relaxation times for electron-neutral, ion-neutral and neutral-neutral collisions respectively.

The cross-collision distribution function is defined as

$$f_{sn}^{eq}(\boldsymbol{r},\boldsymbol{v}_s,t)=\frac{n_s}{2\pi RT_{sn}}\exp\left[-\frac{(\boldsymbol{v}_s-\boldsymbol{u}_{sn})^2}{2RT_{sn}}\right], \tag{5.20}$$

where $\boldsymbol{u}_{sn}$ is the barycentric velocity of the binary collision between particle s and neutrals,

$$\boldsymbol{u}_{sn}=\frac{\rho_s\boldsymbol{u}_s+\rho_n\boldsymbol{u}_n}{\rho_s+\rho_n}. \tag{5.21}$$

T_{sn} is the post-collision temperature after collision with neutrals. According to the kinetic theory [84], T_{en} and T_{in} are defined as

$$T_{en}=T_e+\frac{2m_{en}(T_n-T_e)}{m_e+m_n}+\frac{m_nm_{en}(\boldsymbol{u}_n-\boldsymbol{u}_e)^2}{3k_B(m_e+m_n)}-\frac{2\tau_{en}(\mathrm{R}_e^i-\mathrm{R}_e^m)U_ie}{3k_B}, \tag{5.22}$$

$$T_{in}=T_i+\frac{2m_{in}(T_n-T_i)}{m_i+m_n}+\frac{m_nm_{in}(\boldsymbol{u}_n-\boldsymbol{u}_i)^2}{3k_B(m_i+m_n)}, \tag{5.23}$$

where $m_{en}=m_em_n/(m_e+m_n)$ and $m_{in}=m_im_n/(m_i+m_n)$ are reduced mass of binary collisions. Comparing to ions' post-collision temperature calculation equation, the external term in electrons' post-collision temperature calculation equation considers energy consumption in electron impact ionization and three-body recombination.

The relaxation time τ_{sn} in Eq. (5.19) is defined as

$$\tau_{sn}=\frac{1}{\sigma_{sn}n_n\langle v_s\rangle}, \tag{5.24}$$

where σ_{sn} is the cross section of the elastic collision between particle species s and neutrals. And the cross section can be calculated as $\sigma_{sn}=\pi(r_s+r_n)^2$.

The change of distribution function $\Delta f_s(\boldsymbol{r},\boldsymbol{v}_s,t)$ by inelastic processes, such as multiphoton ionization, electron impact ionization as well as three-body recombination is calculated by

$$\Delta f_s(\boldsymbol{r},\boldsymbol{v}_s,t)=R_s f_s^{eq}(\boldsymbol{r},\boldsymbol{v}_s,t), \tag{5.25}$$

where R_e is coefficient for ionization and recombination. And it can be calculated by rates of multiphoton ionization, electron impact ionization and three–body recombination:

$$R_e=R_n^m n_n/n_e+R_e^i-R_e^r, \tag{5.26}$$

$$R_i=R_n^m n_n/n_i+R_e^i n_e/n_i-R_e^r n_e/n_i, \tag{5.27}$$

$$R_n=-R_n^m-R_e^i n_e/n_n+R_e^r n_e/n_n, \tag{5.28}$$

$$R_n^m=W_{MPI}=A_{MPI}^N I^N, \tag{5.29}$$

$$R_e^i=\sigma_{ec}\langle v_e\rangle n_n, \tag{5.30}$$

$$R_e^r=b_{rec}n_i. \tag{5.31}$$

Taking the specific forms of terms of convection and external force terms, the continuous Boltzmann equation for weakly ionization plasma can be obtained as:

$$f_e^{\alpha}\left(\vec{x}+\vec{e}_e^{\alpha}\Delta t,t+\Delta t\right)=f_e^{\alpha}\left(\vec{x},t\right)-\frac{f_e^{\alpha}\left(\vec{x},t\right)-f_{en}^{\alpha,eq}\left(\vec{x},t\right)}{\tau_{en}}+\Delta t\frac{\vec{a}_e\cdot\left(\vec{e}_e^{\alpha}-\vec{u}_e\right)}{c_{s,e}^2}f_e^{\alpha,eq}\left(\vec{x},t\right)+\Delta tR_e f_e^{\alpha,eq}\left(\vec{x},t\right), \tag{5.32}$$

$$f_i^{\alpha}\left(\vec{x}+\vec{e}_i^{\alpha}\Delta t,t+\Delta t\right)=f_i^{\alpha}\left(\vec{x},t\right)-\frac{f_i^{\alpha}\left(\vec{x},t\right)-f_{in}^{\alpha,eq}\left(\vec{x},t\right)}{\tau_{in}}+\Delta t\frac{\vec{a}_i\cdot\left(\vec{e}_i^{\alpha}-\vec{u}_i\right)}{c_{s,i}^2}f_i^{\alpha,eq}\left(\vec{x},t\right)+\Delta tR_i f_i^{\alpha,eq}\left(\vec{x},t\right), \tag{5.33}$$

$$f_n^{\alpha}\left(\vec{x}+\vec{e}_n^{\alpha}\Delta t,t+\Delta t\right)=f_n^{\alpha}\left(\vec{x},t\right)-\frac{f_n^{\alpha}\left(\vec{x},t\right)-f_n^{\alpha,eq}\left(\vec{x},t\right)}{\tau_{nn}}-\Delta tR_n f_n^{\alpha,eq}\left(\vec{x},t\right). \tag{5.34}$$

5.3.2 The lattice Boltzmann method used for plasma

Despite its close connection with the Boltzmann equation which is the governing equation for plasma dynamics, application of the lattice Boltzmann method for plasma simulation is still in initial stage. When the discrete velocity model is used in Chapman-Enskog analysis, the lattice parameters, such as lattice viscosity, are generally not equal the physical ones. For simple flow problems (such as driven cavity flow and natural convection in a cavity), the fluid flow is determined solely by some dimensionless numbers (such as Reynolds and Rayleigh numbers). Thus the actual properties of the fluid do not need to be used. However, for laser plasma problems, one or several particularly dimensionless number cannot characterize the flow because of the complexity. So in the simulation work of plasma problems using the lattice Boltzmann method, the actual properties must be applied. Li [46] introduced a rescaling method for weakly ionized plasma. In his model, there is not variation of the kinematic viscosity when LBM is adopted by laser plasma. In addition, plasma evolution is driven by the electromagnetic field of laser beam, so the characteristic velocity due to the external force must be matched. In the following D2Q9 is taken as an example to show the rescaling process about the viscosity. The rescaling process about the characteristic velocity will be implemented in later where LBM is used for electron diffusion problem under an external electric filed.

For D2Q9 model, the lattice viscosity [85] is

$$\upsilon_{LBM}=\theta_{LBM}^2\left(\tilde{\tau}-\frac{1}{2}\right)\delta t, \tag{5.35}$$

where θ_{LBM} is the lattice velocity, $\tilde{\tau}$ is the dimensionless relaxation time in LBM. The actual kinematic viscosity is

$$\upsilon=\frac{8\theta^2\tau}{3\pi}, \tag{5.36}$$

where τ is the physical relaxation time in the continuous Boltzmann equation. $\theta=\sqrt{RT}$ is the

physical sound speed. To preserve the diffusion characteristics of particles in plasma, it was assumed that the lattice and kinematic viscosities must be equal:

$$\theta_{LBM} = \frac{8\theta^2\tau}{\sqrt{3}\pi\Delta x\left(\tilde{\tau}-1/2\right)}. \tag{5.37}$$

Thus one rescaling parameter γ is defined as

$$\gamma = \frac{\sqrt{3}\pi\Delta x\left(\tilde{\tau}-1/2\right)}{8\theta\tau}, \tag{5.38}$$

and the lattice Boltzmann relaxation time can be obtained as

$$\tau_{LBM} = \tilde{\tau}\Delta t = \frac{8\tilde{\tau}\gamma^2}{3\pi\left(\tilde{\tau}-1/2\right)}\tau. \tag{5.39}$$

5.4 The Finite Difference Lattice Boltzmann Method

In order to calculate the average values of the particle physical properties, it is necessary to know the distribution function for the system under consideration. The dependence of the distribution function on the independent variables location velocity and time is governed by the continuous Boltzmann equation. The collision term in the continuous Boltzmann equation is very complex, and when it is simplified by the BGK model, the continuous Boltzmann-BGK equation is obtained. When the discrete velocity is used, the discrete Boltzmann-BGK equation is obtained as

$$\frac{\partial f_\alpha}{\partial t} + \vec{c}_\alpha \cdot \nabla f_\alpha = -\frac{1}{\tau}\left(f_\alpha - f_\alpha^{eq}\right). \tag{5.40}$$

When the first differential forward scheme and first upwind scheme is used for the time and space derivation in the discrete Boltzmann-BGK equation, the lattice Boltzmann-BGK equation is obtained. The process using lattice model to calculate lattice Boltzmann-BGK equation is named as the lattice Boltzmann method. In the standard lattice Boltzmann method (SLBM) calculation process, collision and streaming are two essential steps. While in the numerical implementation, the standard suffers some inherent disadvantages, such as uniform mesh, high computational amount. Because LBM is only one special calculation method, many scholars proposed other methods for the Boltzmann equation, such as interpolation-supplemented lattice Boltzmann method (ISLBM), Taylor series expansion and least square-based lattice Boltzmann method (TLLBM), finite-volume lattice Boltzmann method (FVLBM) and finite-difference lattice Boltzmann method (FDLBM). SLBM, ISLBM as well as TLLBM are for the lattice Boltzmann-BGK equation. FVLBM and FDLBM are for discrete Boltzmann-BGK equation. In FDLBM the unsteady and convective terms are solved by the related time and space discrete schemes.

5.4.1 Time discretization

Time discretization is mainly used for the unsteady term $\partial f_\alpha/\partial t$ in Eq. (5.40). There are several

schemes for time accuracy improvement in LBM compressible models. The followings are detailed implementation procedures of second order Runge-Kutta scheme by Cao[99], semi-implicit schemes by Mei and Shyy [100], explicit scheme by Guo [101] and implicit-explicit (IMEX) Runge-Kutta (RK) scheme by Wang [102].

a) The second order Runge-Kutta scheme

$$\begin{aligned} f_\alpha(\vec{x},t+\Delta t/2) &= f_\alpha(\vec{x},t)-(\Delta t/2)R_\alpha(\vec{x},t) \\ f_\alpha(\vec{x},t+\Delta t) &= f_\alpha(\vec{x},t)-\Delta t R_\alpha(\vec{x},t+\Delta t/2) \end{aligned}, \tag{5.41}$$

where $R_\alpha = -\vec{c}_\alpha \cdot \nabla f_\alpha - \left(f_\alpha - f_\alpha^{eq}\right)/\tau$.

b) The semi-implicit scheme

Mei obtained a finite difference lattice Boltzmann equation by discretizing the convective term in an explicit form and the collision term in an implicit form

$$f_\alpha(\vec{x},t+\Delta t) = f_\alpha(\vec{x},t)-\Delta t\vec{c}_\alpha\cdot\nabla f_\alpha(\vec{x},t)-\frac{\Delta t}{\tau}\left[f_\alpha(\vec{x},t+\Delta t)-f_\alpha^{eq}(\vec{x},t+\Delta t)\right]. \tag{5.42}$$

The latest equilibrium distribution function is obtained by a linear extrapolation scheme of results at the former two time steps

$$f_\alpha^{eq}(\vec{x},t+\Delta t) = 2f_\alpha^{eq}(\vec{x},t)-f_\alpha^{eq}(\vec{x},t-\Delta t). \tag{5.43}$$

c) The explicit scheme based on semi-implicit scheme

In order to save the computational cost, Guo modified the semi-implicit scheme by introducing a new distribution function. Firstly Eq. (5.42) is rewrite as

$$f_\alpha(\vec{x},t+\Delta t) = f_\alpha(\vec{x},t)-\Delta t\vec{c}_\alpha\cdot\nabla f_\alpha(\vec{x},t)+\Delta t\left[\theta\Omega_\alpha(\vec{x},t+\Delta t)+(1-\theta)\Omega_\alpha(\vec{x},t)\right], \tag{5.44}$$

where $0\le\theta\le 1$ and Ω_α is the collision term $\Omega_\alpha = -\left(f_\alpha - f_\alpha^{eq}\right)/\tau$. Here θ is the percentage of implicit part in the total collision term. If the new distribution function is defined as

$$g_\alpha = f_\alpha - \Delta t\theta\Omega_\alpha = f_\alpha + \frac{\Delta t\theta}{\tau}\left(f_\alpha - f_\alpha^{eq}\right), \tag{5.45}$$

Eq. (5.44) becomes as

$$g_\alpha(\vec{x},t+\Delta t) = -\Delta t\vec{c}_\alpha\cdot\nabla f_\alpha(\vec{x},t)+(1-\omega+\omega\theta)f_\alpha(\vec{x},t)+\omega(1-\theta)f_\alpha^{eq}(\vec{x},t), \tag{5.46}$$

where $f_\alpha(\vec{x},t) = \dfrac{g_\alpha(\vec{x},t)+\omega\theta f_\alpha^{eq}(\vec{x},t)}{1+\omega\theta}$ and $\omega = \Delta t/\tau$.

5.4.2 Space discretization

Space discretization scheme for the convective term in Eq. (5.40) is firstly critical for the computational accuracy. Secondly it is proved that the appropriate space discretization scheme can well capture the discontinuity even on a coarser grid [103]. Monotone upstream-centered scheme

for conservation laws (MUSCL), total variation diminishing (TVD), weighted essentially non-oscillatory (WENO) are common schemes for shock wave capture in the finite difference method. For two dimensional flows, in consideration of the x component of the convection term $\vec{c}_\alpha \cdot \nabla f_\alpha$ in Eq. (5.40) can be written as

$$\frac{\partial(c_{\alpha x} f_\alpha)}{\partial x} = \frac{1}{\Delta x}\left(\hat{F}_{\alpha,I+1/2,J} - \hat{F}_{\alpha,I-1/2,J}\right), \tag{5.47}$$

where $c_{\alpha x}$ is the x component of $\vec{c}_\alpha$, $\hat{F}_{\alpha,I+1/2,J}$ is the numerical flux at the interface of $\Delta x_I + \Delta x/2$ (I and J are node indexes). Difference of the above different scheme is mainly the different methods to calculate this numerical flux.

a) MUSCL

For third MUSCL scheme [104], the numerical flux is defined as

$$F_{\alpha,I+1/2,J} = \begin{cases} (f_L)_{\alpha,I+1/2,J}\, c_\alpha & if\ c_\alpha \geq 0 \\ (f_R)_{\alpha,I+1/2,J}\, c_\alpha & if\ c_\alpha \leq 0 \end{cases}, \tag{5.48}$$

and

$$\begin{cases} (f_L)_{\alpha,I+1/2,J} = f_{\alpha,I,J} + \left\{\frac{s}{4}\left[(1-\kappa s)\Delta_- + (1+\kappa s)\Delta_+\right]\right\}_{I,J} \\ (f_R)_{\alpha,I+1/2,J} = f_{\alpha,I+1,J} - \left\{\frac{s}{4}\left[(1-\kappa s)\Delta_+ + (1+\kappa s)\Delta_-\right]\right\}_{I+1,J} \end{cases}, \tag{5.49}$$

where $\kappa = 1/3$ and s is a limiter:

$$s = \frac{2\Delta_+\Delta_- + \varepsilon^2}{\Delta_+^2 + \Delta_-^2 + \varepsilon}. \tag{5.50}$$

Here $\varepsilon = 10^{-6}$ is a small number preventing division by zero in the region of null gradient and

$$\begin{aligned} (\Delta_+)_{I,J} &= f_{\alpha,I+1,J} - f_{\alpha,I,J} \\ (\Delta_-)_{I,J} &= f_{\alpha,I,J} - f_{\alpha,I-1,J} \end{aligned}. \tag{5.51}$$

b) WENO scheme

The WENO scheme [105] is an enhancement on the essentially non-oscillatory (ENO) scheme, and it uses a convex combination of all candidate stencils instead of just one as in the original ENO scheme. In fifth WENO, the numerical flux is defined as

$$\hat{F}_{\alpha,I+1/2,J} = \omega_1 \hat{F}^1_{\alpha,I+1/2,J} + \omega_2 \hat{F}^2_{\alpha,I+1/2,J} + \omega_3 \hat{F}^3_{\alpha,I+1/2,J}. \tag{5.52}$$

Under the condition of $e_{\alpha x} \geq 0$, three-order fluxes on three different stencils are given by

$$\begin{aligned}
\hat{F}^1_{\alpha,I+1/2,J} &= \frac{1}{3}F_{\alpha,I-2,J} - \frac{7}{6}F_{\alpha,I-1,J} + \frac{11}{6}F_{\alpha,I,J} \\
\hat{F}^2_{\alpha,I+1/2,J} &= -\frac{1}{6}F_{\alpha,I-1,J} + \frac{5}{6}F_{\alpha,I,J} + \frac{1}{3}F_{\alpha,I+1,J} \\
\hat{F}^3_{\alpha,I+1/2,J} &= \frac{1}{3}F_{\alpha,I,J} + \frac{5}{6}F_{\alpha,I+1,J} - \frac{1}{6}F_{\alpha,I+2,J}
\end{aligned}, \tag{5.53}$$

and the weighted factors ω_i are given by

$$\begin{aligned}
\omega_i &= \frac{\delta_i}{\delta_1+\delta_2+\delta_3} \\
\delta_i &= \frac{d_i}{\left(\vartheta+\theta_i\right)^2} \\
d_1 &= 1/10\,,\, d_2 = 3/5\,,\, d_3 = 3/10 \\
\vartheta &= 10^{-6} \\
\theta_1 &= \frac{13}{12}\left(F_{\alpha,I-2,J} - 2F_{\alpha,I-1,J} + F_{\alpha,I,J}\right)^2 + \frac{1}{4}\left(F_{\alpha,I-2,J} - 4F_{\alpha,I-1,J} + 3F_{\alpha,I,J}\right)^2 \\
\theta_2 &= \frac{13}{12}\left(F_{\alpha,I-1,J} - 2F_{\alpha,I,J} + F_{\alpha,I+1,J}\right)^2 + \frac{1}{4}\left(F_{\alpha,I-1,J} - F_{\alpha,I+1,J}\right)^2 \\
\theta_3 &= \frac{13}{12}\left(F_{\alpha,I,J} - 2F_{\alpha,I+1,J} + F_{\alpha,I+2,J}\right)^2 + \frac{1}{4}\left(3F_{\alpha,I,J} - 4F_{\alpha,I+1,J} + F_{\alpha,I+2,J}\right)^2
\end{aligned}. \tag{5.54}$$

5.5 Simulation of Isothermal Electron Diffusion by LBM

In this section, the above continuous Boltzmann equations for plasma will be solved to simulate the diffusion problem of isothermal weakly ionization plasma. In a $3.71\times3.71\,mm^2$ domain, a helium plasma is preexisted. The electron and singly charged ion number density are all $n_e = n_i = 10^{16}\ cm^{-3}$, and neutral number density is $n_n = 10^{16}\ cm^{-3}$. Thus the electron temperature can be calculated as 0.8008eV according to Saha equation [83]. Neutral temperature is set as 500K. The motive power in this simulation is a n uniform electric fields and the internally generated electric field due to interaction of electrons and ion is neglected.

The initial distribution of the electron number density is in a Gaussian distribution:

$$n_e\left(x,y,t=0\right) = n_{e0}\left[1+0.01\exp\left(-\frac{\left(x-x_c\right)^2+\left(y-y_c\right)^2}{r^2}\right)\right], \tag{2.3.40}$$

where $r = 0.29\ mm$ and $\left(x_c, y_c\right)$ represents the center point of the computational domain. The uniform electric field of 2000 $\mathrm{V/m}$ is used in the positive x direction.

If the above physical parameters are directly used, the dimensionless lattice relaxation time in LBM is 1.304×10^6, which is outrageously out of the valid range [106]. Under an external uniform electric field, the electron drift velocity can be calculated as [107]:

$$\boldsymbol{v}_d = -\frac{e\boldsymbol{E}_0}{m_e}\tau_{en} = \boldsymbol{a}_e\tau_{en}\,. \tag{2.3.41}$$

According to the second rescaling rule $\boldsymbol{a}_e \tau_{en} = \boldsymbol{a}_{e,LBM} \tau_{en,LBM}$, the lattice acceleration can be obtained as

$$\boldsymbol{a}_{e,LBM} = \frac{3\pi\left(\tilde{\tau} - 0.5\right)}{8\gamma^2 \tilde{\tau}} \boldsymbol{a}_e . \tag{2.3.42}$$

Using the mesh system of 256×256, the diffusion process of electrons at $y = y_c$ under an uniform electric field of $\boldsymbol{E}_0 = 20000\ \mathrm{V/m}$ is shown in Fig. 5.1.

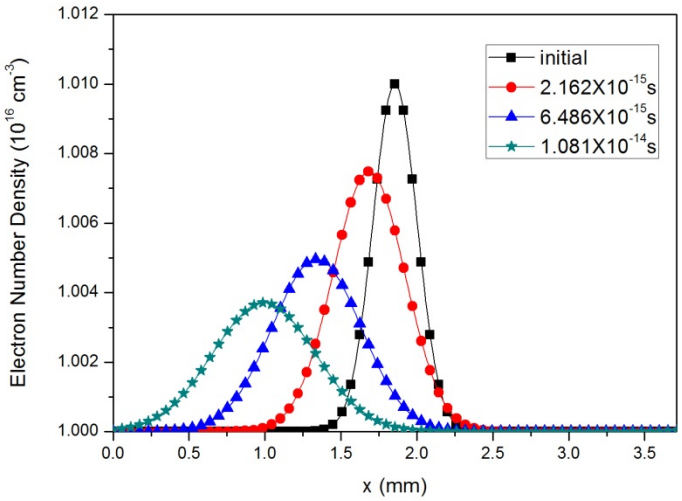

Fig. 5.1 Electron diffusion under an uniform electric field.

CHAPTER 6. NUMERICAL SIMULATION OF INTERACTION BETWEEN LASER AND THE WEAKLY IONIZED PLASMA AND LASER-INDUCED GAS BREAKDOWN PROCESSES

In this chapter interaction of weakly ionized plasma and laser as well as gas plasma generation process by laser irradiation will be simulated. The laser beam is firstly modeled by Maxwell equations and solved by FDTD method. The generation of plasma will be modeled by continuous Boltzmann equations and solved by LBM. The complex energy transformation and transition processes are described macroscopic equations directly derived from continuous Boltzmann equations. These macroscopic are at last solved by the finite volume method (FVM). To ensure the numerical stability the coupling measures among FDTD, LBM and FVM are also discussed in this chapter.

6.1 Introduction

The total deposition process of laser energy into gas can be described by four progressive steps: initial release of electron by multiphoton ionization, ionization of the gas in the focal spot by electron cascade, absorption and reflection of laser energy by the gaseous plasma as well as formation and propagation of the denotation wave into the surrounding gas and relaxation of focal region plasma.

For multiphoton ionization, one electron absorbs several photons simultaneously so that it can escape from the bound of its nuclei. Inverse bremsstrahlung absorption is the mainly measure for transition from laser energy to thermal energy of the plasma. Inverse bremsstrahlung leads the advancement of electron thermal and kinetic energy, which enhances electron cascade process producing dense plasma.

In this chapter, macroscopic equations, which are derived from continuous Boltzmann equations and used for energy transition between particles in plasma, are firstly introduced. And the following is follow chart of the hybrid model. At last the hybrid model is used for simulation of interaction of laser and plasma existing in advance as well as argon plasma generation process.

6.2 Energy Equations of Particles in Plasma as well as the Finite Volume Method

There are complex energy conversion and transformation processes simultaneously existing in the interaction between laser and plasma. However, as a newly developed mesoscopic method, D2Q9 model in LBM cannot have a comprehensive description for such complex energy transport processes. For this reason, total energy equations of different particle species in plasma are directly

derived from the continuous Boltzmann equations and then solved by FVM.

6.2.1 Derivation process of macroscopic energy equations

From the distribution function, the macroscopic variables of physical interest for plasma, such as number density, mean velocity, temperature, and so on, can be calculated. Similarly the differential equations governing the temporal and spatial variations of these macroscopic parameters can also be derived directly from the Boltzmann equation.

The macroscopic variables are related to the moments of the distribution function and the transport equations satisfied by these variables can be obtained by taking the various moments of the Boltzmann equation. The first three moments of the Boltzmann equation, obtained by multiplying it by m_α, $m_\alpha \boldsymbol{v}_\alpha$ and $m_\alpha v_\alpha^2/2$ respectively and integration over all of the velocity space, give the equation of conservation of mass, the equation of conservation of momentum and the equation of conservation of energy. In this research, the macroscopic energy equations of electrons, ions and neutrals are directly derived from their continuous Boltzmann equations. In the following macroscopic energy equation of electrons is taken as an example to show the derivation process. Thus the integrating factor is $\chi(\boldsymbol{v}_e) = \frac{1}{2} m_e v_e^2$. For the continuous Boltzmann equation about electrons:

$$\frac{\partial f_e}{\partial t} + \boldsymbol{\upsilon}_e \cdot \nabla f_e + \boldsymbol{a}_e \cdot \nabla_{\boldsymbol{\upsilon}_e} f_e = -\frac{f_e - f_{en}^{eq}}{\lambda_{en}} + \mathrm{R_e}\, f_e^{eq}, \tag{6.1}$$

multiplying $\chi(\boldsymbol{v}_e) = m_e v_e^2/2$ on every term and integrating the resulting equation over all of the velocity space, the total energy equation can be obtained as

$$\begin{aligned} &\int_{\boldsymbol{v}_e} \chi(\boldsymbol{v}_e) \frac{\partial f_e}{\partial t} d\boldsymbol{v}_e + \int_{\boldsymbol{v}_e} \chi(\boldsymbol{v}_e)(\boldsymbol{v}_e \cdot \nabla f_e) d\boldsymbol{v}_e + \int_{\boldsymbol{v}_e} \chi(\boldsymbol{v}_e)(\boldsymbol{a}_e \cdot \nabla_{\boldsymbol{v}_e}) f_e d\boldsymbol{v}_e \\ &= -\frac{1}{\lambda_{en}} \int_{\boldsymbol{v}_e} \chi(\boldsymbol{v}_e)(f_e - f_{en}^{eq}) d\boldsymbol{v}_e + R_e \int_{\boldsymbol{v}_e} \chi(\boldsymbol{v}_e) f_e^{eq} d\boldsymbol{v}_e \end{aligned}, \tag{6.2}$$

where the first three terms in the left and the right two terms are the unsteady term, the convection term, the acceleration term, and the collision and source terms respectively.

According to gas kinetic theory the mean value of physical parameters can be obtained by

$$\left\langle \chi(\boldsymbol{r},\boldsymbol{v},t) \right\rangle = \frac{1}{n(\boldsymbol{r},t)} \int_{\boldsymbol{v}} \chi(\boldsymbol{r},\boldsymbol{v},t)\, f(\boldsymbol{r},\boldsymbol{v},t)\, d\boldsymbol{v}. \tag{6.3}$$

1) The unsteady term

$$\int_{\boldsymbol{v}_e} \chi(\boldsymbol{v}_e) \frac{\partial f_e}{\partial t} d\boldsymbol{v}_e = \frac{\partial}{\partial t} \int_{\boldsymbol{v}_e} \chi(\boldsymbol{v}_e) f_e d\boldsymbol{v}_e - \int_{\boldsymbol{v}_e} f_e \frac{\partial \chi(\boldsymbol{v}_e)}{\partial t} d\boldsymbol{v}_e = \frac{\partial}{\partial t} \int_{\boldsymbol{v}_e} \chi(\boldsymbol{v}_e) f_e d\boldsymbol{v}_e = \frac{\partial}{\partial t} \left(n_e \left\langle \frac{1}{2} m_e v_e^2 \right\rangle \right)$$

$$
\begin{aligned}
n_e\left\langle\frac{1}{2}m_e v_e^2\right\rangle &= \frac{1}{2}n_e m_e\left\langle v_e^2\right\rangle \\
&= \frac{1}{2}n_e m_e\left\langle(\boldsymbol{c}_e+\boldsymbol{u}_e)\cdot(\boldsymbol{c}_e+\boldsymbol{u}_e)\right\rangle \\
&= \frac{1}{2}n_e m_e\left\langle\boldsymbol{c}_e^2\right\rangle+\frac{1}{2}n_e m_e\left\langle\boldsymbol{c}_e\right\rangle\cdot\boldsymbol{u}_e+\frac{1}{2}n_e m_e\left\langle u_e^2\right\rangle \\
&= \frac{1}{2}n_e m_e\left\langle\boldsymbol{c}_e^2\right\rangle+\frac{1}{2}n_e m_e u_e^2
\end{aligned}
$$

Here c_e is the thermal velocity and $\langle c_e\rangle = 0$.

In gas kinetic theory, the static pressure has the formula $p = \rho\langle c^2\rangle/3$. Assuming electrons as ideal gas, its state equation is $p = nk_BT$.

Thus

$$
n_e\left\langle\frac{1}{2}m_e v_e^2\right\rangle = \frac{3}{2}p_e+\frac{1}{2}n_e m_e u_e^2 = \frac{3}{2}n_e k_B T_e+\frac{1}{2}n_e m_e u_e^2 = \varepsilon_e,
$$

$$
\int_{\boldsymbol{\upsilon}_e}\chi(\boldsymbol{v}_e)\frac{\partial f_e}{\partial t}d\boldsymbol{v}_e = \frac{\partial\varepsilon_e}{\partial t}. \tag{6.4}
$$

2) The convection term

$$
\int_{\boldsymbol{\upsilon}_e}\chi(\boldsymbol{\upsilon}_e)(\boldsymbol{v}_e\cdot\nabla f_e)d\boldsymbol{\upsilon}_e = \nabla\cdot\left(\int_{\boldsymbol{\upsilon}_e}\chi(\boldsymbol{\upsilon}_e)\boldsymbol{\upsilon}_e f_e d\boldsymbol{\upsilon}_e\right)-\int_{\boldsymbol{\upsilon}_e}f_e\boldsymbol{\upsilon}_e\cdot\nabla\chi(\boldsymbol{\upsilon}_e)d\boldsymbol{\upsilon}_e-\int_{\boldsymbol{\upsilon}_e}f_e\chi(\boldsymbol{\upsilon}_e)\nabla\cdot\boldsymbol{\upsilon}_e d\boldsymbol{\upsilon}_e
$$

$\boldsymbol{r}$, $\boldsymbol{\upsilon}_e$ and t in the distribution function are independent variables, so $\nabla\cdot\boldsymbol{\upsilon}_e = 0$. And $\chi(\boldsymbol{\upsilon}_e)$ has no dependent upon space, so $\nabla\chi(\boldsymbol{\upsilon}_e) = 0$. So at last we have

$$
\int_{\boldsymbol{\upsilon}_e}\chi(\boldsymbol{\upsilon}_e)(\boldsymbol{\upsilon}_e\cdot\nabla f_e)d\boldsymbol{\upsilon}_e = \nabla\cdot\left(\int_{\boldsymbol{\upsilon}_e}\chi(\boldsymbol{\upsilon}_e)\boldsymbol{\upsilon}_e f_e d\boldsymbol{\upsilon}_e\right) = \nabla\cdot\left(n_e\left\langle\boldsymbol{\upsilon}_e\chi(\boldsymbol{\upsilon}_e)\right\rangle\right) = \nabla\cdot\left(\frac{1}{2}n_e m_e\left\langle(\boldsymbol{\upsilon}_e\cdot\boldsymbol{\upsilon}_e)\boldsymbol{\upsilon}_e\right\rangle\right)
$$

$$
\begin{aligned}
\left\langle(\boldsymbol{\upsilon}_e\cdot\boldsymbol{\upsilon}_e)\boldsymbol{\upsilon}_e\right\rangle &= \left\langle\left[(\boldsymbol{c}_e+\boldsymbol{u}_e)\cdot(\boldsymbol{c}_e+\boldsymbol{u}_e)\right](\boldsymbol{c}_e+\boldsymbol{u}_e)\right\rangle \\
&= \left\langle\boldsymbol{c}_e^2\boldsymbol{c}_e\right\rangle+\left\langle\boldsymbol{c}_e^2\right\rangle\boldsymbol{u}_e+2\left\langle\boldsymbol{c}_e\boldsymbol{c}_e\right\rangle\cdot\boldsymbol{u}_e+2\boldsymbol{u}_e\boldsymbol{u}_e\cdot\left\langle\boldsymbol{c}_e\right\rangle+u_e^2\left\langle\boldsymbol{c}_e\right\rangle+\left\langle u_e^2\boldsymbol{u}_e\right\rangle \\
&= \left\langle\boldsymbol{c}_e^2\boldsymbol{c}_e\right\rangle+\left\langle\boldsymbol{c}_e^2\right\rangle\boldsymbol{u}_e+2\left\langle\boldsymbol{c}_e\boldsymbol{c}_e\right\rangle\cdot\boldsymbol{u}_e+u_e^2\boldsymbol{u}_e
\end{aligned}
$$

$$
\begin{aligned}
\nabla\cdot\left(\frac{1}{2}n_e m_e\left\langle(\boldsymbol{\upsilon}_e\cdot\boldsymbol{\upsilon}_e)\boldsymbol{\upsilon}_e\right\rangle\right) &= \nabla\cdot\left(\frac{1}{2}n_e m_e\left[\left\langle\boldsymbol{c}_e^2\boldsymbol{c}_e\right\rangle+\left\langle\boldsymbol{c}_e^2\right\rangle\boldsymbol{u}_e+2\left\langle\boldsymbol{c}_e\boldsymbol{c}_e\right\rangle\cdot\boldsymbol{u}_e+u_e^2\left\langle\boldsymbol{u}_e\right\rangle\right]\right) \\
&= \nabla\cdot\left(\boldsymbol{q}_e+\frac{1}{2}n_e m_e\left\langle\boldsymbol{c}_e^2\right\rangle\boldsymbol{u}_e+\boldsymbol{P}_e\cdot\boldsymbol{u}_e+\frac{1}{2}n_e m_e u_e^2\boldsymbol{u}_e\right) \\
&= \nabla\cdot\left(\boldsymbol{q}_e+\boldsymbol{P}_e\cdot\boldsymbol{u}_e+\frac{3}{2}p_e\boldsymbol{u}_e+\frac{1}{2}n_e m_e u_e^2\boldsymbol{u}_e\right) \\
&= \nabla\cdot\boldsymbol{q}_e+\nabla\cdot\left(\boldsymbol{P}_e\cdot\boldsymbol{u}_e\right)+\nabla\cdot\left(\varepsilon_e\boldsymbol{u}_e\right)
\end{aligned} \tag{6.5}
$$

3) The acceleration term

$$\begin{aligned}\int_{\boldsymbol{\upsilon}_e}\chi(\boldsymbol{\upsilon}_e)(\boldsymbol{a}_e\cdot\nabla_{\boldsymbol{\upsilon}_e})f_e d\boldsymbol{\upsilon}_e &= \int_{\boldsymbol{\upsilon}_e}\nabla_{\boldsymbol{\upsilon}_e}\cdot\left(\boldsymbol{a}_e\chi(\boldsymbol{\upsilon}_e)f_e\right)d\boldsymbol{\upsilon}_e-\int_{\boldsymbol{\upsilon}_e}f_e\boldsymbol{a}_e\cdot\nabla_{\boldsymbol{\upsilon}_e}\chi(\boldsymbol{\upsilon}_e)d\boldsymbol{\upsilon}_e-\int_{\boldsymbol{\upsilon}_e}f_e\chi(\boldsymbol{\upsilon}_e)\nabla_{\boldsymbol{\upsilon}_e}\cdot\boldsymbol{a}_e d\boldsymbol{\upsilon}_e\\ &=-\int_{\boldsymbol{\upsilon}_e}f_e\boldsymbol{a}_e\cdot\nabla_{\boldsymbol{\upsilon}_e}\chi(\boldsymbol{\upsilon}_e)d\boldsymbol{\upsilon}_e-\int_{\boldsymbol{\upsilon}_e}f_e\chi(\boldsymbol{\upsilon}_e)\nabla_{\boldsymbol{\upsilon}_e}\cdot\frac{\boldsymbol{F}_e}{m_e}d\boldsymbol{\upsilon}_e\\ &=-\int_{\boldsymbol{\upsilon}_e}f_e\boldsymbol{a}_e\cdot\nabla_{\boldsymbol{\upsilon}_e}\chi(\boldsymbol{\upsilon}_e)d\boldsymbol{\upsilon}_e-\frac{1}{m_e}\int_{\boldsymbol{\upsilon}_e}f_e\chi(\boldsymbol{\upsilon}_e)\nabla_{\boldsymbol{\upsilon}_e}\cdot\boldsymbol{F}_e d\boldsymbol{\upsilon}_e\\ &=-\int_{\boldsymbol{\upsilon}_e}f_e\boldsymbol{a}_e\cdot\nabla_{\boldsymbol{\upsilon}_e}\chi(\boldsymbol{\upsilon}_e)d\boldsymbol{\upsilon}_e-\frac{1}{m_e}\int_{\boldsymbol{\upsilon}_e}f_e\chi(\boldsymbol{\upsilon}_e)\nabla_{\boldsymbol{\upsilon}_e}\cdot\left(\boldsymbol{E}+\boldsymbol{\upsilon}_e\times\boldsymbol{B}\right)d\boldsymbol{\upsilon}_e\\ &=-\int_{\boldsymbol{\upsilon}_e}f_e\boldsymbol{a}_e\cdot\nabla_{\boldsymbol{\upsilon}_e}\chi(\boldsymbol{\upsilon}_e)d\boldsymbol{\upsilon}_e\\ &=-n_e\left\langle\boldsymbol{a}_e\cdot\nabla_{\boldsymbol{\upsilon}_e}\chi(\boldsymbol{\upsilon}_e)\right\rangle\end{aligned}$$

$$\nabla_{\boldsymbol{\upsilon}_e}\chi(\boldsymbol{\upsilon}_e)=\frac{1}{2}m_e\nabla_{\boldsymbol{\upsilon}_e}(\boldsymbol{\upsilon}_e\cdot\boldsymbol{\upsilon}_e)=\frac{1}{2}m_e\nabla_{\boldsymbol{\upsilon}_e}(\boldsymbol{\upsilon}_e\cdot\boldsymbol{\upsilon}_e)=m_e(\boldsymbol{\upsilon}_e\cdot\nabla_{\boldsymbol{\upsilon}_e})\boldsymbol{\upsilon}_e=m_e\boldsymbol{\upsilon}_e$$

$$\begin{aligned}\int_{\boldsymbol{\upsilon}_e}\chi(\boldsymbol{\upsilon}_e)(\boldsymbol{a}_e\cdot\nabla_{\boldsymbol{\upsilon}_e})f_e d\boldsymbol{\upsilon}_e &= -n_e\left\langle\boldsymbol{a}_e\cdot\nabla_{\boldsymbol{\upsilon}_e}\chi(\boldsymbol{\upsilon}_e)\right\rangle\\ &=-n_e\left\langle\boldsymbol{a}_e\cdot m_e\boldsymbol{\upsilon}_e\right\rangle\\ &=-n_e\left\langle q_e\left(\boldsymbol{E}+\boldsymbol{\upsilon}_e\times\boldsymbol{B}\right)\cdot\boldsymbol{\upsilon}_e\right\rangle\\ &=-n_e q_e\boldsymbol{u}_e\cdot\boldsymbol{E}\\ &=-\boldsymbol{J}_e\cdot\boldsymbol{E}\end{aligned}$$

4) The collision term

$$R_{\mathrm{e}}\int_{\boldsymbol{\upsilon}_e}\chi(\boldsymbol{\upsilon}_e)f_e^{eq}d\boldsymbol{\upsilon}_e=R_{\mathrm{e}}\varepsilon_e$$

$$\begin{aligned}-\frac{1}{\lambda_{en}}\int_{\boldsymbol{\upsilon}_e}\chi(\boldsymbol{\upsilon}_e)(f_e-f_{en}^{eq})d\boldsymbol{\upsilon}_e &= -\frac{1}{\lambda_{en}}\left[\int_{\boldsymbol{\upsilon}_e}\chi(\boldsymbol{\upsilon}_e)f_e d\boldsymbol{\upsilon}_e-\int_{\boldsymbol{\upsilon}_e}\chi(\boldsymbol{\upsilon}_e)f_{en}^{eq}d\boldsymbol{\upsilon}_e\right]\\ &=-\frac{1}{\lambda_{en}}\left[\frac{3}{2}n_e k_B\left(T_e-T_{en}\right)+\frac{1}{2}n_e m_e\left(u_e^2-u_{en}^2\right)\right]\end{aligned}$$

$$\begin{aligned}&\frac{3}{2}n_e k_B\left(T_e-T_{en}\right)+\frac{1}{2}n_e m_e\left(u_e^2-u_{en}^2\right)\\ &=\frac{3}{2}n_e k_B\left(-\frac{2m_{en}\left(T_n-T_e\right)}{m_e+m_n}-\frac{m_n m_{en}\left(\boldsymbol{u}_n-\boldsymbol{u}_e\right)^2}{3k_B\left(m_e+m_n\right)}+\frac{2\lambda_{en}\,\mathrm{R_e}\,U_i e}{3k_B}\right)+\frac{1}{2}n_e m_e\left(u_e^2-u_{en}^2\right)\\ &=-\frac{3k_B n_e m_{en}\left(T_n-T_e\right)}{m_e+m_n}+\lambda_{en}\,\mathrm{R_e}\,n_e U_i e+\frac{1}{2}n_e m_e\left(u_e^2-u_{en}^2-\frac{m_n m_n\left(\boldsymbol{u}_n-\boldsymbol{u}_e\right)^2}{\left(m_e+m_n\right)^2}\right)\\ &=-\frac{3k_B n_e m_{en}\left(T_n-T_e\right)}{m_e+m_n}+\lambda_{en}\,\mathrm{R_e}\,n_e U_i e+\frac{1}{2}n_e m_e\left(u_e^2-u_{en}^2-\left(\boldsymbol{u}_{en}-\boldsymbol{u}_e\right)^2\right)\\ &=-\frac{3k_B n_e m_{en}\left(T_n-T_e\right)}{m_e+m_n}+\lambda_{en}\,\mathrm{R_e}\,n_e U_i e+n_e m_e\boldsymbol{u}_{en}\cdot\left(\boldsymbol{u}_e-\boldsymbol{u}_{en}\right)\end{aligned}$$

So we get the final form of collision and source terms as

$$
\begin{aligned}
&-\frac{1}{\lambda_{en}}\int_{\boldsymbol{\upsilon}_e}\chi(\boldsymbol{\upsilon}_e)(f_e-f_{en}^{eq})d\boldsymbol{\upsilon}_e+\mathrm{R_e}\int_{\boldsymbol{\upsilon}_e}\chi(\boldsymbol{\upsilon}_e)f_e^{eq}d\boldsymbol{\upsilon}_e\\
&=-\frac{1}{\lambda_{en}}\left[-\frac{3k_Bn_em_{en}\left(T_n-T_e\right)}{m_e+m_n}+\lambda_{en}\,\mathrm{R_e}\,n_eU_ie+n_em_e\boldsymbol{u}_{en}\cdot\left(\boldsymbol{u}_e-\boldsymbol{u}_{en}\right)\right]+\mathrm{R_e}\,\varepsilon_e\\
&=\frac{3k_Bn_em_{en}\left(T_n-T_e\right)}{\lambda_{en}\left(m_e+m_n\right)}-\mathrm{R_e}\,n_eU_ie-\frac{n_em_e}{\lambda_{en}}\boldsymbol{u}_{en}\cdot\left(\boldsymbol{u}_e-\boldsymbol{u}_{en}\right)+\mathrm{R_e}\,\varepsilon_e
\end{aligned}
$$

Thus electron energy equation can be obtained as

$$
\begin{aligned}
&\frac{\partial\varepsilon_e}{\partial t}+\nabla\cdot\boldsymbol{q}_e+\nabla\cdot\left(\boldsymbol{P}_e\cdot\boldsymbol{u}_e\right)+\nabla\cdot\left(\varepsilon_e\boldsymbol{u}_e\right)-\boldsymbol{J}_e\cdot\boldsymbol{E}\\
&=\frac{3k_Bn_em_{en}\left(T_n-T_e\right)}{\lambda_{en}\left(m_e+m_n\right)}-\mathrm{R_e}\,n_eU_ie-\frac{n_em_e}{\lambda_{en}}\boldsymbol{u}_{en}\cdot\left(\boldsymbol{u}_e-\boldsymbol{u}_{en}\right)+\mathrm{R_e}\,\varepsilon_e
\end{aligned}
\tag{6.6}
$$

5) The total energy equation of ions and neutrals

The total energy equations of electrons and ions are similar, while for electron ionization, the consumption energy is supplied by electrons. So the total energy equation of ions is

$$
\frac{\partial\varepsilon_i}{\partial t}+\nabla\cdot\boldsymbol{q}_i+\nabla\cdot\left(\boldsymbol{P}_i\cdot\boldsymbol{u}_i\right)+\nabla\cdot\left(\varepsilon_i\boldsymbol{u}_i\right)-\boldsymbol{J}_i\cdot\boldsymbol{E}=\frac{3k_Bn_im_{in}\left(T_n-T_i\right)}{\lambda_{in}\left(m_i+m_n\right)}-\frac{n_im_i}{\lambda_{in}}\boldsymbol{u}_{in}\cdot\left(\boldsymbol{u}_i-\boldsymbol{u}_{in}\right)+\mathrm{R}_i\,\varepsilon_i \tag{6.7}
$$

Because of no charge, the total energy equation of neutrals has no joule heating term.

Besides, in laser induced weakly ionized gas plasma only binary collisions (electron-neutral and ion-neutral) are considered. The number density of neutrals is much larger than that of charged particles, so not the all neutral participate the collisions with electrons and ions. Here collisions between neutrals and electron will be taken as an example to show the energy obtained by neutrals.

After the collision with electrons, the post-collision average velocity and temperature of neutrals are

$$
\boldsymbol{u}_n{}'=\boldsymbol{u}_{ne}=\frac{m_e\boldsymbol{u}_e+m_n\boldsymbol{u}_n}{m_e+m_n}
$$

$$
T_n^{'}=T_{ne}=T_n+\frac{2m_{en}}{m_e+m_n}\left(T_e-T_n\right)+\frac{m_em_{en}}{3k_B\left(m_e+m_n\right)}\left(\boldsymbol{u}_n-\boldsymbol{u}_e\right)^2
$$

So in the collisions with electrons, the change energy is

$$
\frac{3}{2}n_ek_B\left(T_n-T_{ne}\right)+\frac{1}{2}n_em_n\left(u_n^2-u_{ne}^2\right)
$$

Comparing with energy change of electrons, in the above equation the number density of electrons is used even though the mass of neutrals are used. The above equation is reasonable because not all neutrals participate into the collisions, so the number density of electrons is used to denote that part of neutrals which have collisions with electrons.

$$
\begin{aligned}
&\frac{3}{2}n_e k_B\left(T_n - T_{ne}\right) + \frac{1}{2}n_e m_n\left(u_n^2 - u_{ne}^2\right) \\
&= \frac{3}{2}n_e k_B\left(-\frac{2m_{en}\left(T_e - T_n\right)}{m_e + m_n} - \frac{m_e m_{en}\left(\boldsymbol{u}_e - \boldsymbol{u}_n\right)^2}{3k_B\left(m_e + m_n\right)}\right) + \frac{1}{2}n_e m_n\left(u_n^2 - u_{ne}^2\right) \\
&= -\frac{3k_B n_e m_{en}\left(T_e - T_n\right)}{m_e + m_n} + \frac{1}{2}n_e\left(m_n\left(u_n^2 - u_{ne}^2\right) - \frac{m_e m_{en}\left(\boldsymbol{u}_e - \boldsymbol{u}_n\right)^2}{m_e + m_n}\right) \\
&= \frac{3k_B n_e m_{en}\left(T_n - T_e\right)}{m_e + m_n} + \frac{1}{2}n_e m_n\left(u_n^2 - u_{ne}^2 - \frac{m_e m_e}{\left(m_e + m_n\right)^2}\left(\frac{\left(m_e + m_n\right)\boldsymbol{u}_{en} - m_n\boldsymbol{u}_n - m_e\boldsymbol{u}_n}{m_e}\right)^2\right) \\
&= \frac{3k_B n_e m_{en}\left(T_n - T_e\right)}{m_e + m_n} + \frac{1}{2}n_e m_n\left(u_n^2 - u_{ne}^2 - \left(\boldsymbol{u}_{ne} - \boldsymbol{u}_n\right)^2\right) \\
&= \frac{3k_B n_e m_{en}\left(T_n - T_e\right)}{m_e + m_n} + n_e m_n \boldsymbol{u}_{en}\cdot\left(\boldsymbol{u}_n - \boldsymbol{u}_{en}\right)
\end{aligned}
$$

Similar with the collisions between electrons and neutrals, the change energy in collisions between ions and neutrals is

$$
\frac{3}{2}n_i k_B\left(T_n - T_{ni}\right) + \frac{1}{2}n_i m_n\left(u_n^2 - u_{ni}^2\right) = \frac{3k_B n_i m_{in}\left(T_n - T_i\right)}{m_i + m_n} + n_i m_n \boldsymbol{u}_{in}\cdot\left(\boldsymbol{u}_n - \boldsymbol{u}_{in}\right)
$$

At last, the total energy equation of neutrals is

$$
\begin{aligned}
&\frac{\partial \varepsilon_n}{\partial t} + \nabla\cdot\boldsymbol{q}_n + \nabla\cdot\left(\boldsymbol{P}_n\cdot\boldsymbol{u}_n\right) + \nabla\cdot\left(\varepsilon_n\boldsymbol{u}_n\right) = \\
&\frac{3k_B n_e m_{en}\left(T_e - T_n\right)}{\lambda_{en}\left(m_e + m_n\right)} - \frac{n_e m_n}{\lambda_{en}}\boldsymbol{u}_{en}\cdot\left(\boldsymbol{u}_n - \boldsymbol{u}_{en}\right) + \frac{3k_B n_i m_{in}\left(T_i - T_n\right)}{\lambda_{in}\left(m_i + m_n\right)} - \frac{n_i m_n}{\lambda_{in}}\boldsymbol{u}_{in}\cdot\left(\boldsymbol{u}_n - \boldsymbol{u}_{in}\right) + \mathrm{R}_n\,\varepsilon_n
\end{aligned}
\tag{6.8}
$$

6.2.2 Theory of the finite volume method

Different from the finite difference and finite element methods, the finite volume method (FVM) [108] divides the computational domain into a series of control volume. Each control volume is represented by one node. Then equations in conservative form, such as Euler and Navier-Stokes equations, have integration implementation at each control volume to get their discrete forms. Thus simulation results can be obtained after numerical calculation of the discrete equations. In the integration, variation profiles of the unknown function as well as its first-order derivative should be artificial assumed at interfaces of control volumes, such as piecewise-linear or stepwise. In the discretization process of location derivative terms, values at the last (explicit scheme) or present (implicit scheme) time levels can be used. For explicit scheme, the discrete equation can be solved easily. While for implicit scheme, there are many methods for solution of equation sets, such as TDMA, Gauss-Seidel iteration. Nowadays FVM can be used compressible and incompressible flow fluid problems. When Navier-Stokes equations are numerically calculated, density (pressure), velocity can be solved directly-the primitive variable method. in addition, there are vorticity-stream

function and vorticity-velocity methods which use stream function or vorticity as unknown functions.

6.3 Measures for Coupling among LB, FDTD and FV Methods

FDTD, LBM and FVM are together used to numerically simulate the generation process of gas plasma induced by laser radiation. In order to ensure the coordination of the calculation, it is necessary to use the same mesh system and time step in the three different methods. In FDTD, because of the stability requirement, the space step cannot be larger than one-tenth of the laser wavelength [109, 110], so the whole space step is determined by FDTD.

Furthermore, the time step in FDTD must satisfy the Courant condition:

$$c\Delta t \le \frac{1}{\sqrt{\frac{1}{(\Delta x)^2}+\frac{1}{(\Delta y)^2}+\frac{1}{(\Delta z)^2}}}. \tag{6.9}$$

For two dimensional case, when $\Delta x = \Delta y = \delta$, the limiting condition of the time step is

$$c\Delta t \le \frac{1}{\sqrt{2}\delta}. \tag{6.10}$$

In the same mesh system, the time step should be selected as

$$\Delta t = \min\left(\Delta t_{FDTD}, \Delta t_{LBM}, \Delta t_{FVM}\right). \tag{6.11}$$

For the time step in LBM, it is determined by $\Delta t_{LBM} = \frac{\delta}{\sqrt{3}\theta_{\max}}$, where $\theta_{\max}$ is the maximum sound speed of three different particle. Usually $\theta_{\max}$ is the sound speed of electrons, even which $\theta_{\max}$ is much smaller than the speed of light under the laser irradiation. After the similar preliminary quantitative analysis, it can be concluded that the smallest time step among the three different methods is that used in FDTD.

Once all needed parameters are known, the entire numerical implementation processes can be briefly summarized as shown in Fig. 6.1. Firstly Maxwell equations are solved by FDTD, new electric and magnetic fields of the laser beam are obtained. Secondly, using the previous number densities, velocities and temperature, the rescaled parameters in LBM are calculated. Following the rescaling process, number density and velocities fields of different particles species in plasma can be renovated after discrete Boltzmann equations being solved. At last, temperature fields are clarified by solving the total energy equations of electrons, ions and neutrals directly derived from the continuous Boltzmann equations.

6.4 Numerical Simulation of Interaction between Laser and Weakly Ionized Plasma

In this section, two problems are solved to validate the above mathematic models. The first one is

the interaction between laser and plasma with temperature change. In this problem, with assumption of 0.01% ionization rate before calculation, inelastic collisions just contain electron impact ionization and three-body recombination. In the second part, FDTD and LBM are then coupled together for the simulation of multiphoton ionization process of neutrals.

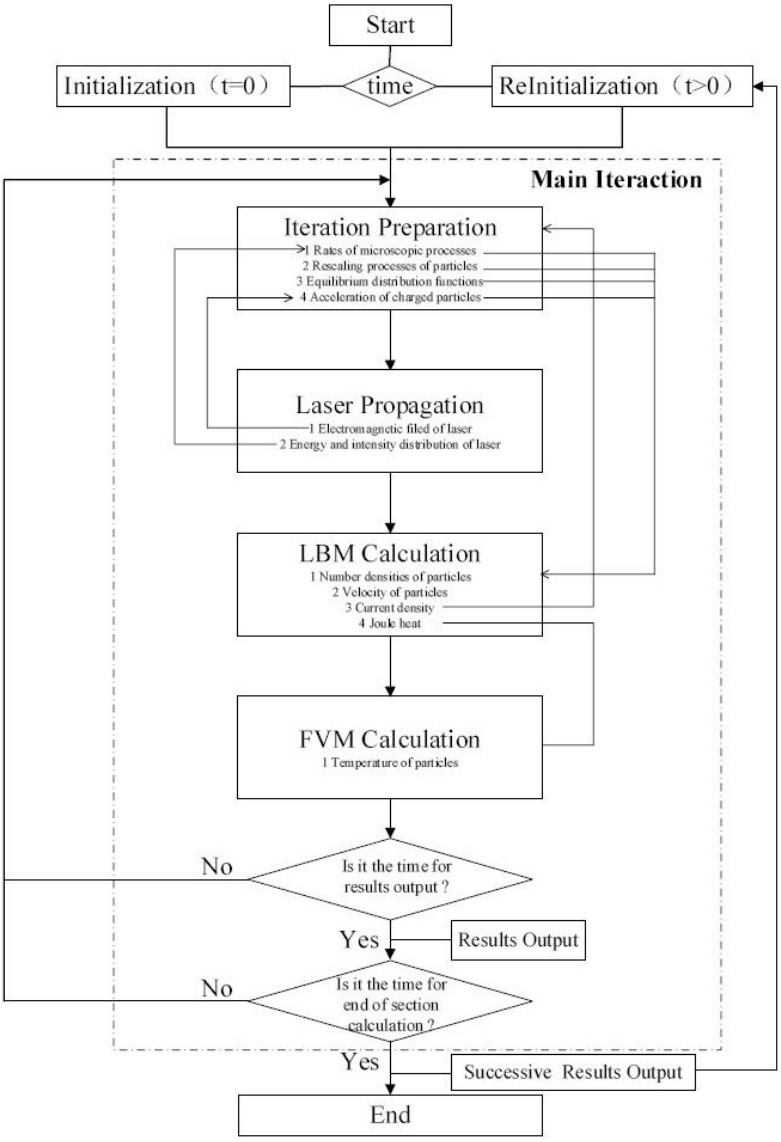

Fig. 6.1 Flow chart of the hybrid model.

6.4.1 Interaction between laser and plasma

In this case, 0.01% ionization rate is assumed as an initial condition. It is not necessary to consider the occurrence of initial charged particles. Calculation of change rates of distribution functions by multiphoton ionization is skipped, then total coefficients of ionization and recombination for electrons, ions and neutrals are $R_e = R_e^i - R_e^r$, $R_i = R_e^i n_e / n_i - R_e^r n_e / n_i$, $R_n = -R_e^i n_e / n_n + R_e^r n_e / n_n$

respectively.

Initial parameters of the physical problems are shown in Table 6. For simplicity, the continuous laser is simplified as a Gaussian beam. The source of Gaussian beam is set at the bottom line of the computational domain and then laser propagates toward the top.

Fig. 6.2 presents electron and ion number densities at 40 ps. Form the figure, we can see electron and ion number densities along laser's propagation centerline are bigger than that in the other region. For a Gaussian beam, intensity of electromagnetic field is Gaussian distributions perpendicular to the beam propagation, so the electrons and ions existing in the centerline of laser can obtained much more laser energy and their kinetic energy increases sharply. Because of electron impact ionization, these electrons with enough kinetic energy can produce new electrons and ions by collisions with neutrals, which is why number densities of charged particles are bigger along laser's centerline. In addition, laser energy is piecemeal absorbed by changed particles when propagating in plasma, the electrons in the upper part of the computational region can be accelerated so slowly that fewer new electrons can be produced in the electron impact ionization process. Therefore, along laser's propagation centerline, number densities of charged particles decrease gradually.

Table 6 Parameters about interaction between laser and plasma.

Laser	wavelength[μm]		intensity[$W \cdot m^{-2}$]
	10.64		2×10^{8}
Physical region	area[μm^2]		mesh
	135.68×135.68		256×256
Particles in plasma	species	initial number density[m^{-3}]	initial temperature[K]
	electron	2.687×10^{21}	12277.5
	ion	2.687×10^{21}	12277.5
	neutral	2.687×10^{25}	12277.5

Temperature fields of electrons and ions at 40 ps are showed in Fig. 6.3. Along the centerline of laser, temperatures of charged particles are higher, and the reason is similar with that of larger number densities of charged particles. At the same position and time, electron temperature is much higher than that of ions, which is because, in the same electromagnetic field, the heated process of ions with much heavier weight is slower than the process of electrons. Comparing Fig. 6.3(a) and Fig. 6.3(b), the hot electron area is little larger, which is reasonable because the accelerated process of electrons with lighter weight is faster and then electrons can spread into the broader area within the same time interval than ions.

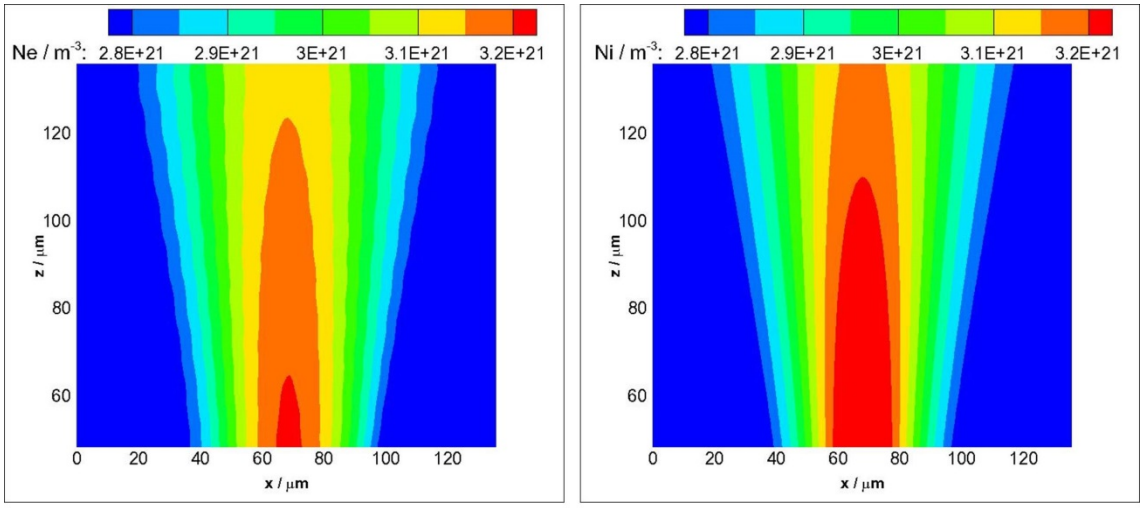

(a) Electron (b) Helium ion

Fig. 6.2 Electron and ion number densities at 40 ps.

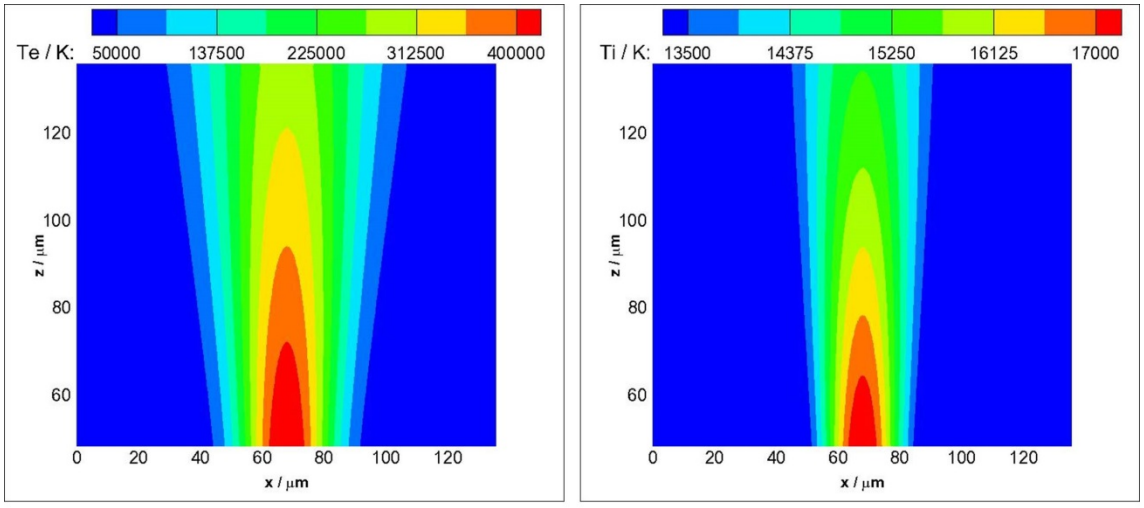

(a) Electron (b) Helium ion

Fig. 6.3 Electron and ion temperature at 40 ps.

6.4.2 Multiphoton ionization of Helium

In this case, temperature change is neglected in calculation. The main purpose of this problem is to validate the applicability of the model to multiphoton ionization. Besides the assumption of three order multiphoton ionization process is used in calculation of the multiphoton ionization cross section.

As the medium of plasma, there are only helium neutrals as the initial condition in the computational domain. The related initial parameters are shown in Table 7. For laser, the Gaussian source is also set at the bottom line of the computational domain, but the focusing process is included in FDTD for this problem.

Table 7 Parameters about laser induced isothermal helium plasma with MPI.

Laser	wavelength[μm]		intensity[$W \cdot m^{-2}$]
	10.64		5×10^{8}
Physical region	area[μm^2]		mesh
	135.68×135.68		256×256
Particles in plasma	species	initial number density[m^{-3}]	initial temperature[K]
	electron	0	11604.4
	ion	0	11604.4
	neutral	6.304×10^{23}	11604.4

Fig. 6.4 shows number densities of electrons and ions at 5 and 10 ps. From (a) and (b) in Fig. 6.4, we can see electrons and ions are firstly produced at focus point of laser, which is reasonable because the initial electrons and ions appear mainly depending on multiphoton ionization. The denser photons at laser's focusing point ensure the bigger cross section and then multiphoton ionization process firstly occurs at laser's focus point.

Comparing (a)–(c) and (b)–(d) in Fig. 6.4, growth of the hot plasma area is obvious. Once initial electrons and ions are produced, they are accelerated and absorb laser energy intensely. After electrons and ions accelerated by the laser, they can move to broader area. Form Fig. 6.4, we can see that growth of plasma is opposite to laser's propagation direction. This is because the charged particles in the lower area of the computational region firstly come into contact with laser, then they can absorb laser energy more strongly.

In this section, only single ionization is considered, so the total number of electrons and ions should be equal theoretically. Comparing number densities of electrons and ions at the same position and time, ion number density is much larger than that of electrons. For the same electromagnetic field, the magnitude of Lorentz forces for electrons and ions are equal, while ions with heavier weight can only get smaller accelerator and spread to smaller area comparing with electrons, so ion number density is larger than that of electron at the same position and time.

If the interaction time of laser and plasma is expanded, the growth of plasma becomes slower and slower. In present study, the growth of plasma is mainly depending on multiphoton ionization and electron impact ionization. Once initial electrons and ions are produced by multiphoton ionization, they can directly absorb laser's energy by Lorentz force. When electromagnetic energy is obtained by charged particles, the photon number density decreases. The multiphoton ionization rate R_n^{mpi} becomes smaller, so fewer charged particles can be produced by multiphoton ionization. For electron impact ionization, the rate R_e^{eii} increases mainly depending on the cross section and average thermal speed of electrons. These two parameters increase with temperature, while in present study isothermal plasma is assumed, so they cannot obviously increase with the absorbed process of laser energy. Based on the above two reasons, the general result is that plasma's growth

becomes slower. In the real plasma generation and development processes, once electrons are produced by multiphoton ionization, their temperature increases sharply because of acceleration by Lorentz force and frequent collisions with neutrals. The rise of temperature make the number density change coefficient by electron impact ionization increase, so plasma can continue growing.

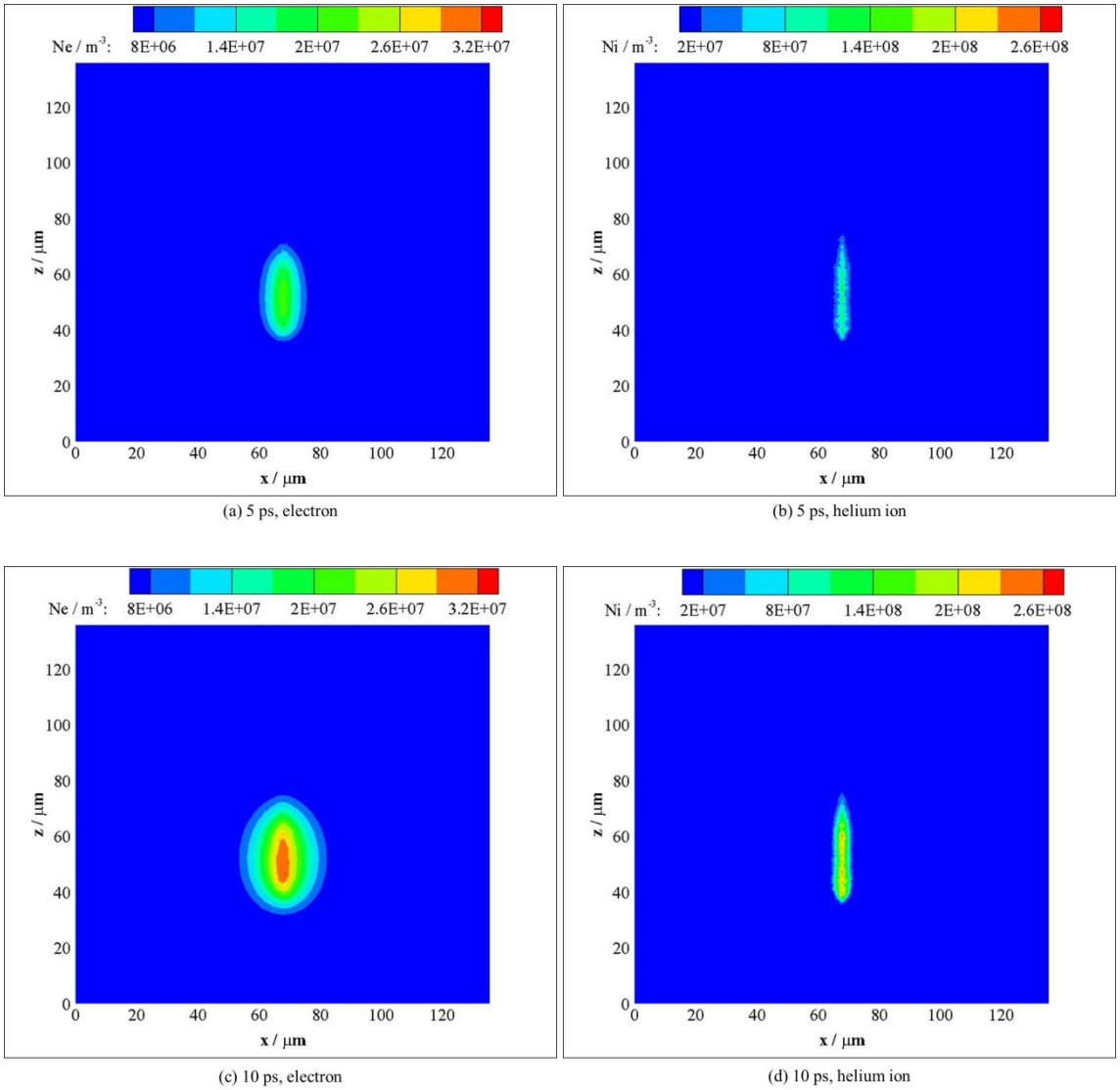

(a) 5 ps, electron (b) 5 ps, helium ion

(c) 10 ps, electron (d) 10 ps, helium ion

Fig. 6.4 Electron (a, c) and ion (b, d) number densities at 5 (a, b) and 10 (c, d) ps.

6.5 Numerical simulation of Laser-induced Argon Breakdown

Using the above developed model, generation and development processes of helium plasma induced by laser radiation are simulated in this paper. Physical parameters about the laser, helium as well as the computational region are shown in Table 8.

In this simulation, the assumption of three-order multiphoton ionization process is used. From the parameters in Table 8, the space step can be inferred as one twentieth of the laser wavelength,

which ensures that FDTD can capture fluctuations of the electromagnetic field. The time step used in this simulation is calculated by $\Delta t = \Delta x / 2c$ to protect the numerical stability.

Table 8 Parameters about laser induced helium plasma.

Laser	wavelength[μm]		intensity[$W \cdot m^{-2}$]
	10.64		1.488×10^{8}
Physical region	area[μm^2]		mesh
	135.68×135.68		256×256
Particles in plasma	species	initial number density[m^{-3}]	initial temperature[K]
	electron	0	300
	ion	0	300
	neutral	2.44×10^{24}	300

Fig. 6.5 presents number densities of electrons and ions at 20 ps, 60 ps and 100 ps. Firstly, it is very easy to be found expansions of the area with the same charged particles species after comparing Fig. 6.5 (a), (b) and (c), (d), (e) and (f). These are evidence of the growth of plasma with the extended interaction time between laser and plasma. In Fig. 6.5 the laser propagates to the top from the bottom line of the computational region, while the growth of plasma is along the opposite direction of laser propagation. In the interaction between laser and plasma, the charged particles in the following area of plasma are firstly exposed to laser, so they can absorb more energy and then get larger velocity and temperature. According to the theory of electron impact ionization, the more kinetic and internal energy electrons have, the more electrons and ions can be produced in the collisions between electrons and helium neutrals. So the plasma grows along the opposite direction of laser propagation. Besides, as shown in Fig. 6.5, the area with electrons is larger than that with ions, which is reasonable because electrons can get larger acceleration compared with ions in the same electromagnetic field and migrate into a broader area within the same time interval. Furthermore, at the same time, the number density of electrons is little smaller than that of ions on the same nodes. This phenomenon accords with the larger migration area of electrons because only singly ionized process is considered in the developed model.

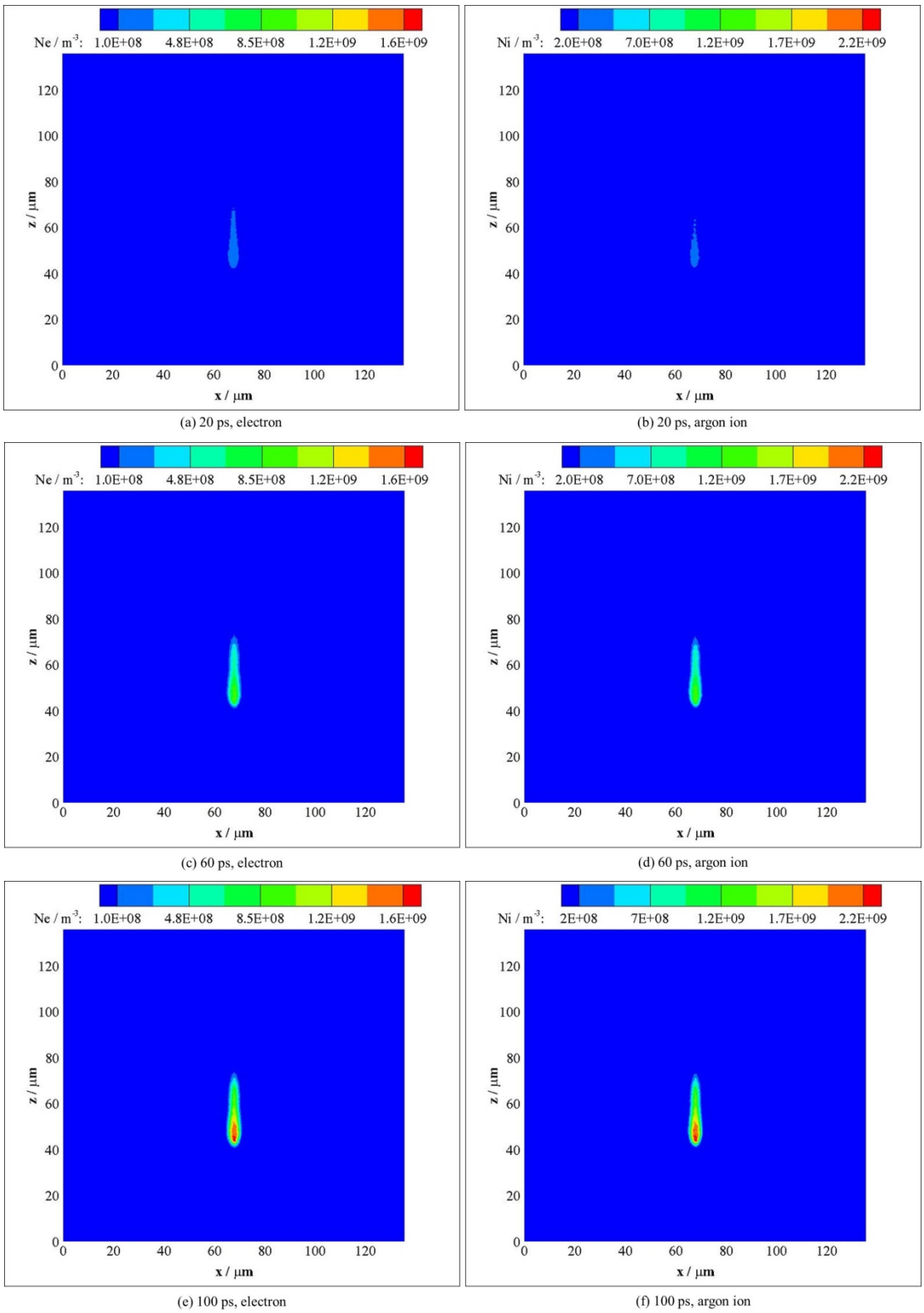

(a) 20 ps, electron (b) 20 ps, argon ion

(c) 60 ps, electron (d) 60 ps, argon ion

(e) 100 ps, electron (f) 100 ps, argon ion

Fig. 6.5 Number densities of electrons and ions at 20 ps, 60 ps and 100 ps.

In generation and development processes of gas plasma induced by laser radiation, there are still complex energy conversion and transformation phenomena. Temperature fields of electrons and

ions at 1 ps and 2 ps are given in Fig. 6.6. From temperature fields of the same particle species, we can see the hot plasma region becomes larger with elapsed time. Because energy absorbed by particles in plasma comes from the laser, temperature of the same particle species along the centerline of laser is higher than the other region. Laser propagates upward from the bottom of the computational region, so charged particles in the lower half of plasma firstly obtain laser energy, then their temperature increases quicker. Comparing Fig. 6.6 (a) and (c), (b) and (d), temperature of electrons is obviously much higher than that of ions at the same nodes and same intermediate times. This phenomenon is another proof of the faster heated process of electrons compared with ions. Accelerated by laser, velocities of electrons and ions increase. The growth of internal energy of charged particles depends on the kinetic energy loss in their collisions with neutrals. Ions are much heavier than electrons, so their accelerated and heated processes are slower.

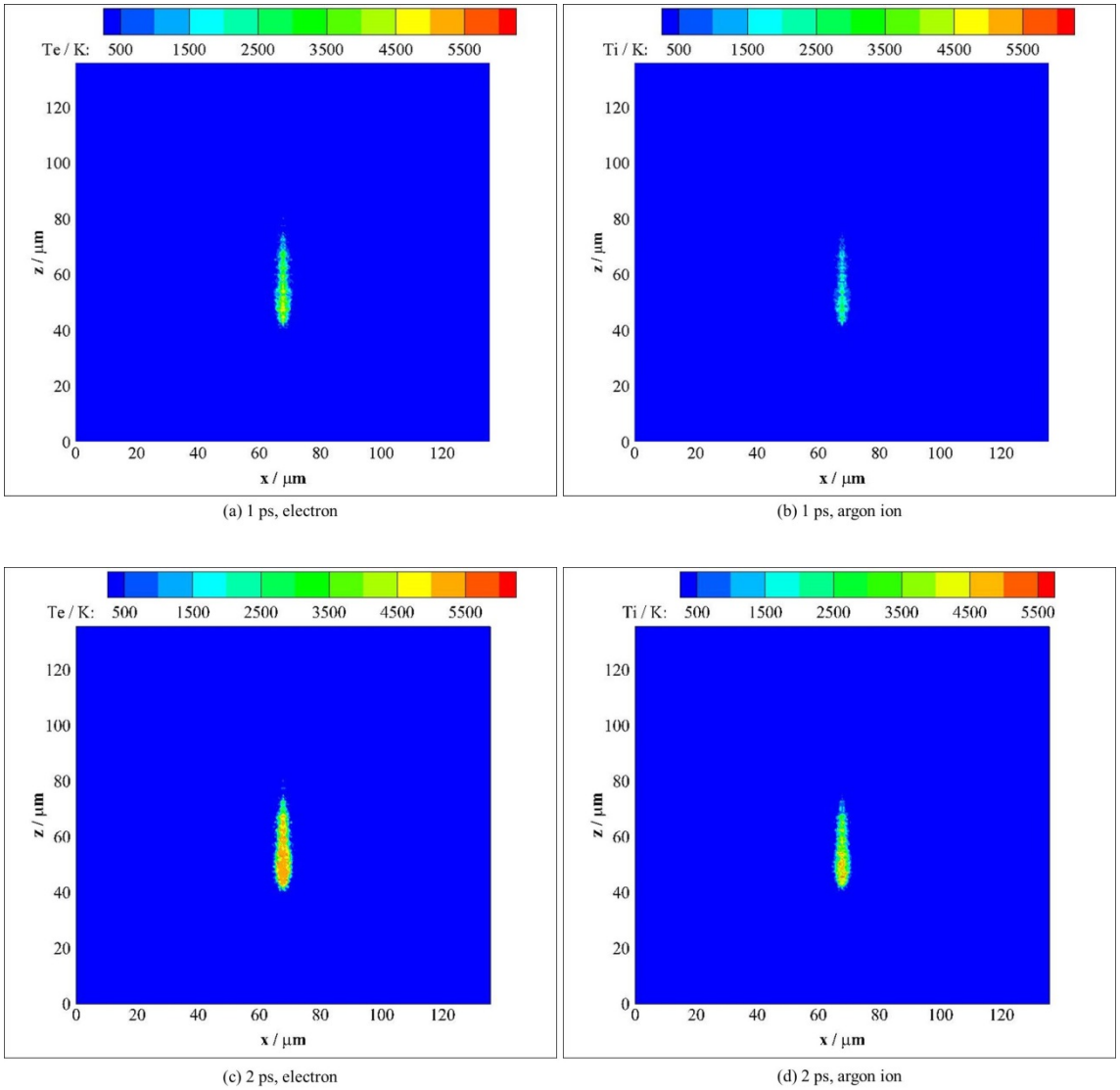

(a) 1 ps, electron

(b) 1 ps, argon ion

(c) 2 ps, electron

(d) 2 ps, argon ion

Fig. 6.6 Electron and ion temperature at 1 ps and 2 ps.

Furthermore, temperature fields of electrons and ions at 4 ps, 8 ps and 20 ps are shown in Fig. 6.7. At 4 ps, similar with the discussion above, temperature of electrons is higher than that of ions at the same nodes. Comparing temperature fields of electrons at the three intermediate times, there are two kinds of trends. Firstly, the area with electrons becomes an isothermal region. Then a small temperature decreasing process exists with matured plasma is obtained. In the generation process of plasma, electrons are firstly produced by multiphoton ionization. Once seed electrons are obtained, they can absorb laser energy intensively and their velocity and temperature increase very sharply. The increase of kinetic and internal energies of electrons will make electron impact ionization occur. In electron impact ionization, with energy being consumed to supply the ionization energy of neutrals, temperature of electrons decreases. Finally, energy absorbed from the laser is equal to that consumed to supply the ionization energy. For ions, isothermal area is also realized, while this trend is mainly because of thermal conduction in ions and their collisions between neutrals. Ions have no temperature dropping trend in the whole process because only energy of electrons is consumed in electron impact ionization.

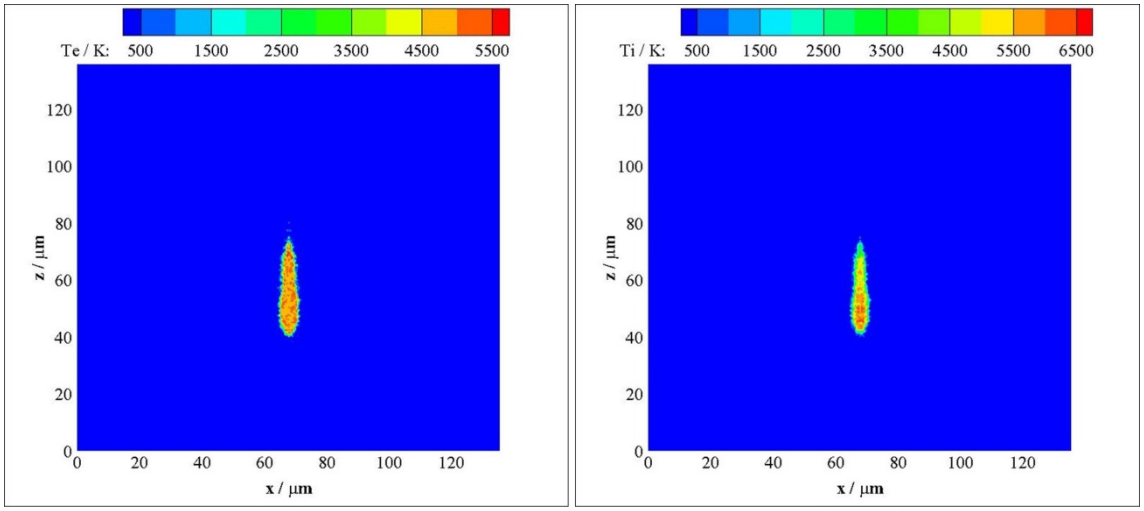

(a) 4 ps, electron

(b) 4 ps, argon ion

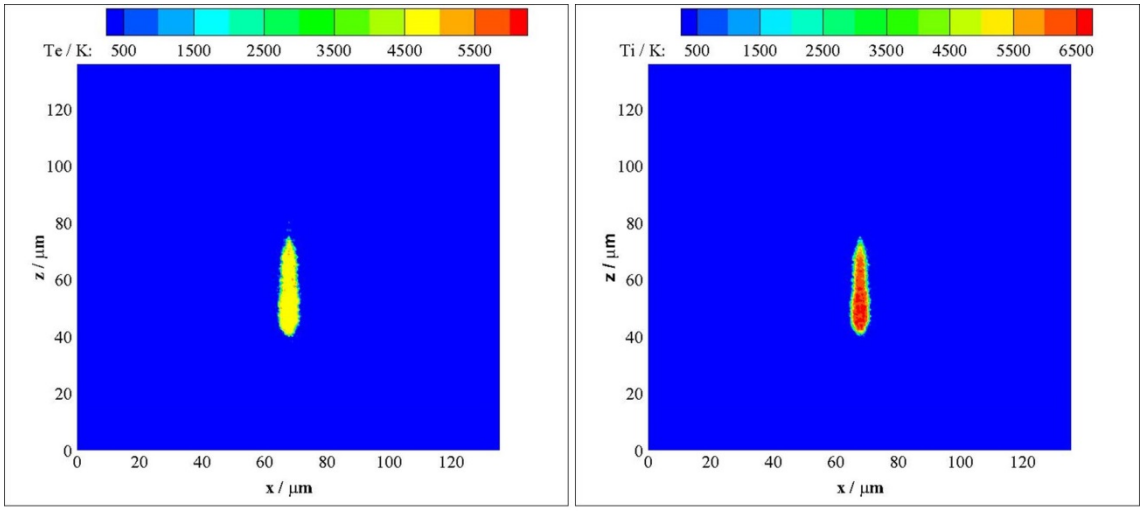

(c) 8 ps, electron (d) 8 ps, argon ion

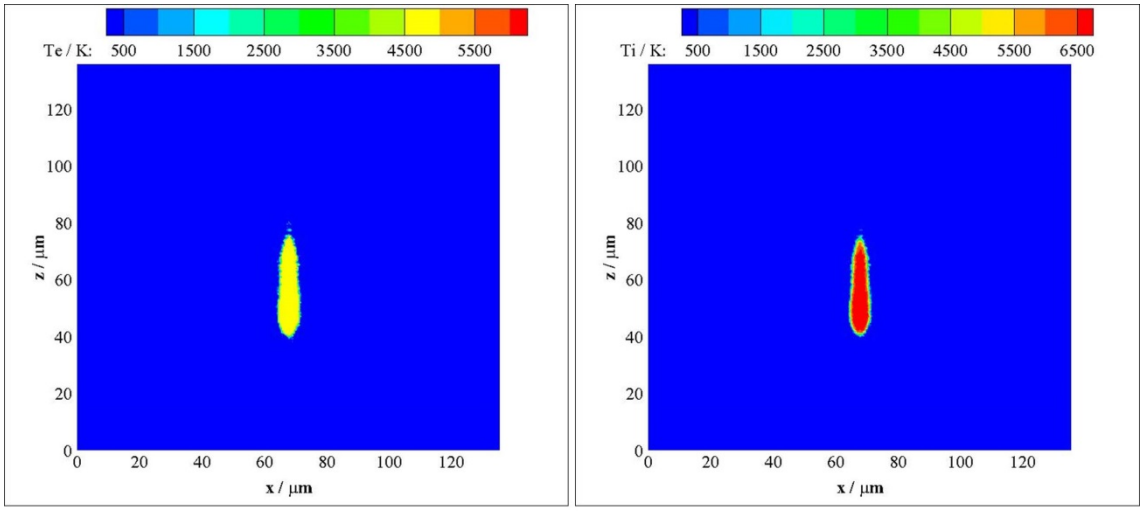

(e) 20 ps, electron (f) 20 ps, argon ion

Fig. 6.7 Electron and ion temperature at 4 ps, 8 ps and 20 ps.

For laser induced gas plasma, a mathematic model combined by Maxwell equations, Boltzmann equations and Navier-stokes equations is introduced. This hybrid model describes generation and development processes of gas plasma induced by laser radiation from multiphoton ionization. Under the same mesh system, FDTD, LBM and FVM, coupled by the smallest time step, can be used to solve the equations in the developed model.

In order to validate the developed model, generation and development processes of helium plasma are simulated. From the simulation results, we can see that because of multiphoton ionization electrons and ions firstly appear at the focus spot of laser. Under Lorentz force of electromagnetic field of the laser, the existing electrons are accelerated sharply and obtain huge kinetic energy in a short time. When kinetic energy of electrons is enough to nourish the ionization potential of

neutrals, there may be new electrons produced in collisions between electrons and neutrals. At the same time, some kinetic energy of electrons loses to be converted into the internal energy in collisions with neutrals, so temperature of electrons increases. For ions, because of the mass is much larger comparing to electrons, their accelerated and heated processes are slower.

The results in this paper show the capabilities of the developed method used to handle the laser induced plasma process from multiphoton ionization. The focus of next stage is to optimize the simulation work by comparing with experimental results.

CHAPTER 7. APPLICATION OF GAS PLASMA BY LASER IRRADIATION FOR IODINE MEASUREMENT

One important industrial application is laser-induced breakdown spectroscopy (LIBS). In the cooling process of plasma by laser irradiation, emission radiation will be exhausted from plasma and its wavelength is related to constitution of plasma. When those emission radiation is collected and analyzed, the plasma constitution will be clarified. Noises of LIBS measurement include continuous blackbody radiation, co-exist molecular emission as well as the build-in emission of instruments. Intensity of continuous blackbody radiation is proportional to biquadrate of plasma temperature, and the increase of plasma temperature is mainly controlled by electron impact ionization. Upon iodine measurement in gas, this chapter studied detection characteristics of low pressure, short pulse LIBS.

7.1 Introduction

Iodine is a necessary element in the environment, contained in most materials, such as soil, rocks, ocean, food, and so on. Iodine is also one of the essential trace elements of the human body, called intellectual element. The total amount of iodine in healthy adult is about 20-50 mg, 70%-80% of which exist in the thyroid gland. The World Health Organization (WHO) recommends the intake of iodine should not exceed 300 μg a day. Nuclear accidents show that the radioactive iodine is the serious influencing factor for human health and environment. For example, in Japan, after the Fukushima nuclear power plant accident, the pollution of the radioactive materials becomes the focal issue and research point. Human and other organisms can take in the radioactive materials, such as iodine, Cs, Sr, Se and so on, which leads to severe disease.

There are several papers proposing various methods for iodine detection in food, brine, air, etc. The technology of Gas Chromatography-Mass Spectrometry (GC-MS) was employed to determinate iodine in various applications [111, 112]. The high mobility of iodine in aquatic systems has led to ^{129}I contamination problems at sites where nuclear fuel has been reprocessed. In order to assess the distribution of ^{129}I and stable ^{127}I in environmental systems, a sensitive and rapid method was developed which enables determination of isotopic ratios of iodine. Iodide concentrations were quantified using Gas Chromatography-Mass Spectrometry (GC-MS) [113]. A new approach of the combination with post derivatization and Gas Chromatography-Mass Spectrometry (GC-MS) for the quantification of gaseous molecular iodine (I_2) was presented for laboratory- and field-based studies and its novel application for the measurement of radioactive molecular iodine [114]. Inductively Coupled Plasma associated with Optical Emission Spectroscopy (ICP-OES) and Mass Spectrometry (ICP-MS) technologies have been successfully applied to analyze iodine in different

kinds of samples [115-117]. Several sample preparation techniques have been evaluated for the determination of iodine using UV-photochemical generation-quadrupole inductively coupled plasma mass spectrometry, which was applied to the analysis of real samples [118]. However, sample preparation was required to utilize these technologies.

As one important use of plasma produced by laser irradiation, Laser-Induced Breakdown Spectroscopy (LIBS) is an appealing detection technique compared with many other methods of elemental analysis because of the fast response, high sensitivity, real-time and non-contact features without any pre-preparation of samples. The technology has been widely used in gas, liquid and solid materials. With the development of the laser technology, short pulse width lasers, such as picosecond laser and femtosecond laser have been employed for LIBS technique. The utilization of short pulse laser for plasma generation has been extensively studied [119, 120]. Short pulse irradiation allowed for a specificity of excitation that could yield LIBS signals more tightly and showed significantly lower background emission.

Laser-induced plasma process in gas phase is different from that in solid phase. One of the challenging targets of LIBS is the enhancement of detection limit of gas phase materials. In this chapter, iodine in buffer gases of N_2 and air was detected by LIBS technology using nanosecond and picosecond breakdowns of CH_3I at reduced pressure. The laser-induced plasma process such as the electron impact ionization process can be controlled by reducing the pressure and employing short pulse laser. The method reported here can improve the detection ability of iodine measurement in practical applications.

7.2 Theory

Plasma generation and evolution in LIBS can be descripted as: the free electron production by multiphoton ionization in the focus spot of the laser beam; via inverse bremsstrahlung absorption the electrons obtain an abundant of laser energy, and when their energy can supply the ionization potential, the molecular or atomic neutrals can be ionized producing new free electrons, this process is named as electron impact ionization. The new produced electrons continuously participate inverse bremsstrahlung absorption and electron impact causing cascade ionization. Within short time intervals, the gas will be breakdown by cascade producing plasma. The plasma can absorb laser energy more intensively and its temperature and pressure increase sharply until the end of the laser pulse. When the laser pulsed is ended, the plasma will be cooled gradually. As shown in Fig.5.1, three-body recombination will happen in abundance with the cooling process and the plasma temperature decreases. The excited ions or neutrals will have de-excitation process exhausting radiation which can be used for gas component measurement after collected and analyzed.

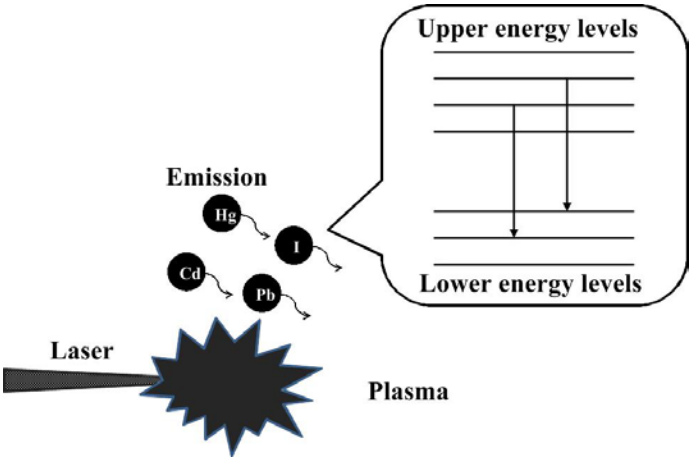

Fig. 7.1 Theory of laser-induced breakdown spectroscopy

As shown in Fig.5.2, plasma emission in LIBS has two stages. In the first stage, it is the continuous radiation. In the plasma cooling process, the electrons will lose their energy in collisions with other particles cause bremsstrahlung emission, and some electrons can be captured by ions release energy. The emission in those two processes are continuous radiation. In the second stage, the line emissions will be generated via de-excitation of existed ions or neutrals. While in the initial phase, there is some continuous radiation. In plasma growth process, the laser energy is absorbed by plasma, the ions or neutrals at the lower energy levels will transit to upper level. In this stage the inverse processes will happen. Because the emission line has related wavelength with the ions or neutrals, so it is named as characteristic radiation spectroscopy. LIBS measurement collects the radiation in this stage to clarify the component of plasma.

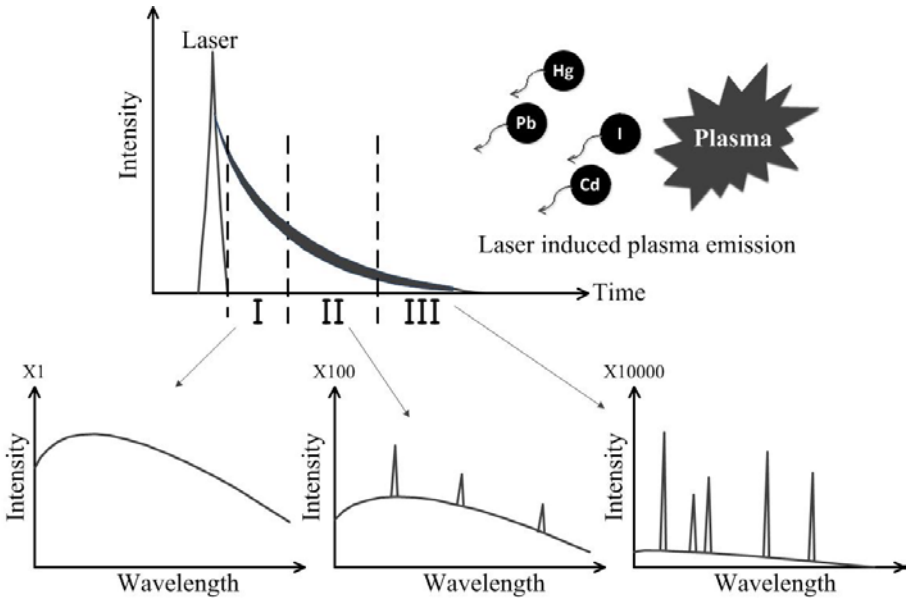

Fig. 7.2 LIBS spectra change with delay time

Despite the fact that the processes involved in LIBS are complex, the emission intensity from the optically thin plasma during the cooling process was mostly examined by the following equation with the assumption of a uniform plasma temperature and no self-absorption:

$$I_{(i)} = n_{(i)} \sum_j \left\{ K_{(i),j} g_{(i),j} \exp\left(-\frac{E_{(i),j}}{k_B T} \right) \right\} \tag{7.1}$$

In the above expression, $I_{(i)}$ is the emission intensity of species i, $n_{(i)}$ is the concentration of species i, $K_{(i),j}$ is a variable that includes the Einstein A coefficient from the upper energy level j, $g_{(i),j}$ is the statistical weight of species i at the upper energy level j, $E_{(i),j}$ is the upper level energy of species i, k_B is the Boltzmann constant and T is the plasma temperature. Eq. (7.1) is applicable under the conditions of local thermodynamic equilibrium (LTE).

For species α, if energies at two level are $\varepsilon_{\alpha,i}$ and $\varepsilon_{\alpha,j}$ respectively, the number of particles at these two levels under the local thermodynamic equilibrium, $n_{\alpha,i}$, $n_{\alpha,j}$, has the following relationship:

$$\frac{n_{\alpha,\mathrm{i}}}{n_{\alpha,\mathrm{j}}} = \frac{g_{\alpha,\mathrm{i}}}{g_{\alpha,\mathrm{j}}} \exp\left(-\frac{\varepsilon_{\alpha,\mathrm{i}} - \varepsilon_{\alpha,\mathrm{j}}}{k_{\mathrm{B}} T} \right) \tag{7.2}$$

From Eq.(7.2), it is can be deduced that where particle species is in local thermodynamic equilibrium, the number of particles at upper energy level is smaller than that at lower energy level. While for the species not in local thermodynamic equilibrium, the number of particle at upper energy level is bigger than that under the local thermodynamic equilibrium.

There are several interferences with the target signals in LIBS process, generally including the continuum emission from plasma itself, coexisting molecular and atomic emissions, noise from detectors, and so on. At high pressure, the main interference is the continuum emission from plasma itself, the intensity of which is proportional to biquadratic temperature. The plasma temperature including the temperatures of electrons, ions and neutrals is also high. The generated plasma is dense and the electrons, ions and neutrals collide frequently with each other. The temperatures of electrons, ions and neutrals become approximately same through violent collision to transfer energy in high pressure plasma, generally called thermal plasma. At low pressure, however, the density of plasma is rather low and few opportunities of the collisions between electrons and other particles cause the large difference of kinetic energy. Once initial electrons and ions are produced, they are accelerated by absorbing laser energy intensely. Because of the mass difference between charged particles, the kinetic energy of electron is much higher. Since the neutrals obtain the energy by the collision of particles, the kinetic energy of neutrals is lower compared with that of the charged particles. In this case these particles are not in LTE condition. T_e, T_i and T_n are defined as the kinetic temperatures of electrons, ions and neutrals respectively and the temperatures are in the order $T_e >> T_i$, $T_e >> T_n$, which is called cold plasma. In this case,

the departure from LTE produces a population of excited levels differing from Boltzmann distribution. Populations of ions and neutrals in upper energy levels are larger than that of the LTE condition [121]. This phenomenon becomes eminent in the low pressure condition in which collisions are reduced and the expansion of plasma becomes faster. The interference of coexisting molecular and atomic emissions appears from the products of plasma generation process. At low pressure, the interference of the continuum emission from plasma itself decreases dramatically. Because the collisional and plasma quenching processes are not significant under the reduced pressure conditions, stable and longer existing plasma is formed through the plasma expansion, which makes the signal detection much easier with low interference.

Another important strategy of this study is the control of the electron impact ionization process by the laser pulse width. Once charged particles are produced by multiphoton ionization, laser energy will be absorbed by the inverse bremsstrahlung intensively and plasma grows rapidly by electron impact ionization. This plasma growth process can be controlled using short pulse width lasers, such as picosecond laser. To investigate the phenomena described above, the theoretical model in chapter 5 using LBM was applied and the gas plasma generation processes were described using the continuous Boltzmann equations. Maxwell equations, which were used to model the propagation of laser, were calculated by the finite difference time domain (FDTD) method. Employing coefficients of distribution functions, processes of inverse bremsstrahlung, multiphoton ionization, electron impact ionization and three-body recombination were included in Boltzmann equations. Creation and evolution processes of particles in plasma were clarified.

LIBS signals arising in plasma cooling period are determined by the initial plasma creation process including multiphoton ionization and electron impact ionization that can be controlled by pressure, laser pulse width, and wavelength. Because the difference of multiphoton ionization rates between N_2 and CH_3I is large and CH_3I is largely dissociated by the laser irradiation [122], the features of emission signal will also change, which is the study in this paper. At high pressure, electron impact ionization is the major source of plasma generation. Multiphoton ionization becomes the dominant process in plasma generation when reducing the pressure. In this study, low pressure and short pulse laser breakdown was employed to the iodine detection of CH_3I in buffer gases of N_2 and air. The upper level energy of detection species is listed in Table 9. Iodine wavelength at 183 nm (I-3) was the representative signal in this study according to the upper level energy. Experimental Apparatus

Fig. 7.3 illustrates the experimental apparatus used in this study. The apparatus fundamentally consisted of lasers, vacuum chamber, lens, detectors and so on. Three different pulse width lasers were employed to measure iodine. Nanosecond laser employed was pulse Nd:YAG laser (Quanta-Ray Pro-230, 6-12 ns, 10 Hz, beam diameter: 9 mm) operated at fundamental radiation 1064 nm and second harmonic 532 nm with different pulse energy, respectively. The output

parameters of picosecond laser 1 (EKSPLA SL312, 150 ps, 10 Hz, beam diameter: 10 mm) were: 1064 nm and 150 mJ/p. The output parameters of picosecond laser 2 (Quantel YG901C-10, 35 ps, 10 Hz, beam diameter: 9.5 mm) were: 1064 nm and 64 mJ/p. The output laser beam was focused into the measurement area using the lens with focal length of 80 mm. The measurement chamber was a vacuum cell with four quartz windows and its internal volume was about 200 cm^3. The path length from the center of chamber to the quartz windows was 65 mm. Perpendicular to laser propagation direction, emission from another window of the chamber was focused onto the spectrometer slit. The focal length of the lens between vacuum chamber and spectrometer was 60 mm. Emission signals were finally detected by combination of a spectrometer (JASCOCT-10S), an ICCD camera (Princeton Instruments Inc., Model ITEA/CCD-576-S/RB-E) and auxiliary equipment. The signal of 100 shots (10 s) was measured three times at each condition. The detection limit was estimated by accumulating signals of 600 shots (1 min). The gate width was set to 30 μs in this study. In the measurement of iodine, the iodine signal was located at vacuum UV region such as 183 nm, in which there was the effect of O_2 absorption. Therefore N_2 was purged along the detection path from the vacuum chamber to the spectrometer, which is shown as the dashed range in Fig. 7.3.

The standard gas of CH_3I in N_2 with concentration of 101 ppm (Taiyo Nippon Sanso) was used and diluted by the buffer gases of N_2 and air to reduce the concentration around few ppm levels due to the high sensitivity of LIBS technology. The pressure was measured by a pressure gauge (Tem-Tech Lab. SE1000-SNV-420T1) installed at the evacuation port of the chamber.

Table 9 Upper level energy of detection species.

Species	Upper energy (cm^{-1})	Lower energy (cm^{-1})	Wavelength (nm)
I-1	56092.88	0	178.3
I-2	63186.76	7602.97	179.9
I-3	54633.46	0	183
I-4	56092.88	7602.97	206.2
C	61981.82	10192.63	193
N-1	86220.51	28839.31	174.3

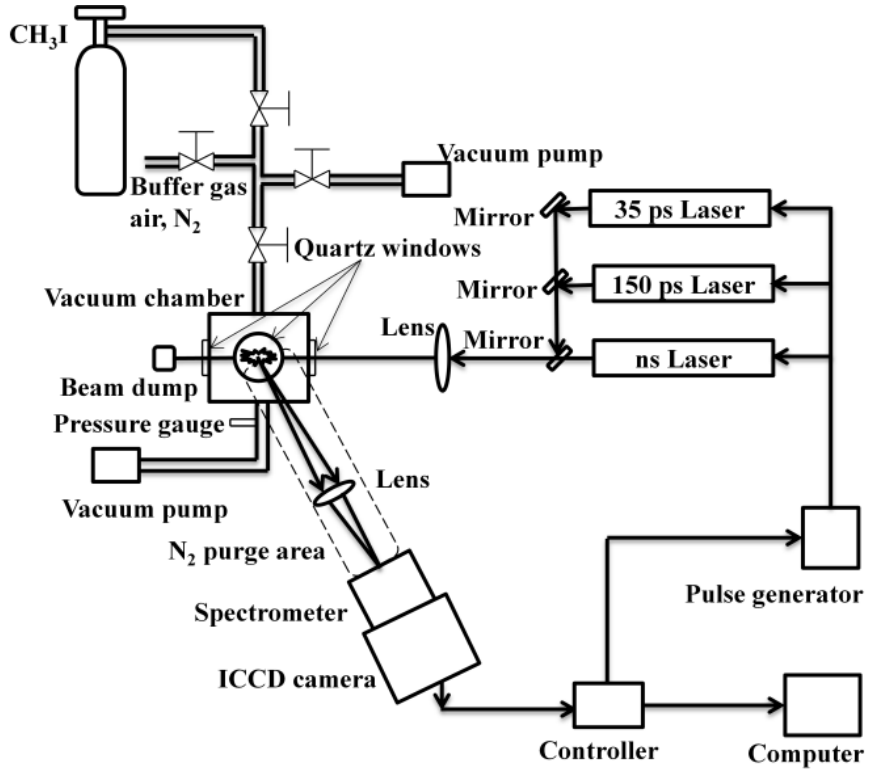

Fig. 7.3 Schematic diagram of the experimental apparatus.

7.3 Results and Discussion

There are several interferences with the target signals in LIBS process, generally including the continuum emission from plasma itself, coexisting molecular and atomic emissions, noise from detectors, and so on. Iodine signal in N_2 was measured at the pressure of 30 kPa using ns 1064 nm breakdown. It was difficult to distinguish the signals of iodine and C in short delay time because of the strong interference of the continuum emission from plasma itself. In long delay time of 30 μs and 50 μs, there were discriminable signals of iodine emission, as shown in Fig. 7.4. In order to confirm the different emission signals, the pure gas of N_2 was also detected under the same conditions, such as N emissions at 174.3 nm (N-1), 184.6 nm, 188.5 nm and 213 nm. The intensity ratio of I-3 to C is much higher in the delay time of 50 μs compared with that in the delay time of 30 μs due to the fact that there is the difference of the upper level energies between C (61981.82 cm^{-1}) and I-3 (54633.46 cm^{-1}). At this range of pressure, the electron impact ionization process becomes the major process to raise the temperature of plasma and the emission signals tended to follow Eq. (7.1) limiting the improvement of signal to noise ratio.

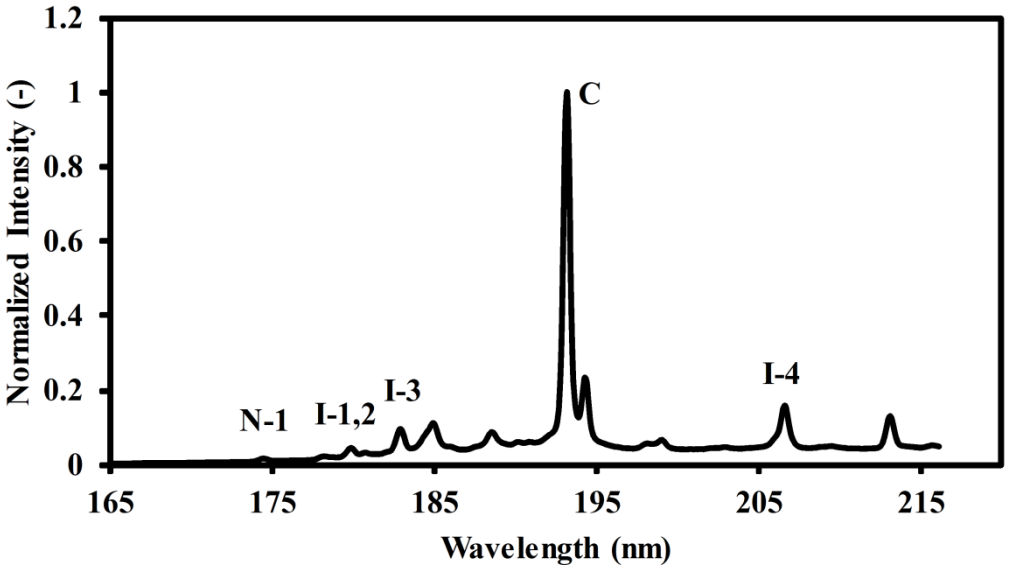

(a) Delay time: 30 μs

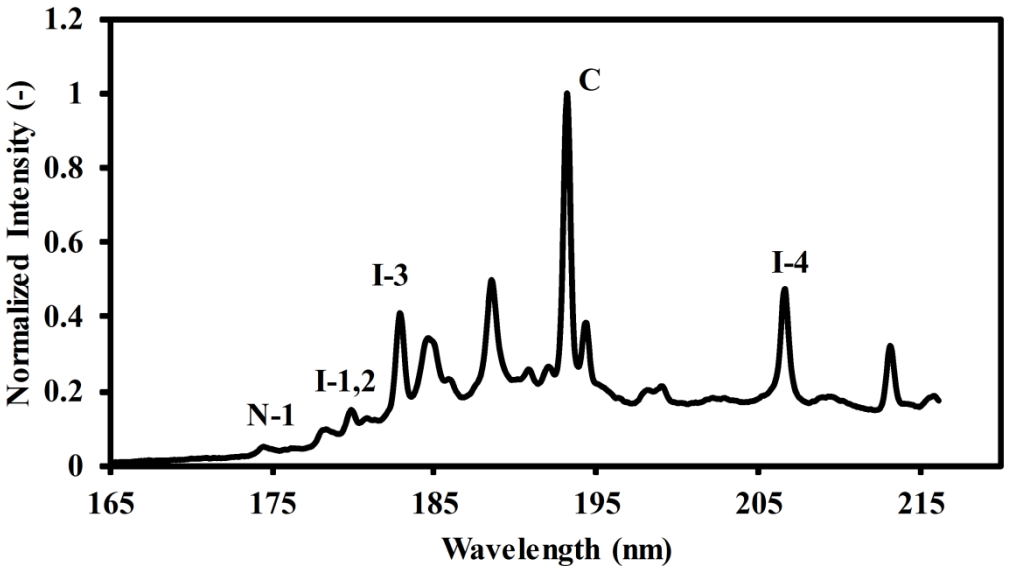

(b) Delay time: 50 μs

Fig. 7.4 LIBS spectra of iodine signal at high pressure. Conditions: ns 1064 nm, power 400 mJ/p, pressure 30 kPa, gate width 30 μs, buffer gas N_2. The signal was normalized by C signal intensity.

7.4.1 Nanosecond breakdown of CH_3I in N_2 under different conditions

Under reduced pressure condition, iodine in buffer gas of N_2 was detected using nanosecond breakdown. Fig. 7.5 shows the measurement results of iodine signal at low pressure of 1300 Pa

using 1064 nm and 532 nm breakdowns with laser power of 400 mJ/p. The obvious iodine signal can be distinguished from the spectra in both cases. These spectra were not detected at 30 kPa by adjusting the delay time. At low pressure, the particles, such as electrons, ions and neutrals, in cold plasma were not in LTE condition. The temperature of plasma mainly referred to the neutrals of excited iodine at low pressure, which was also lower compared with that at higher pressure because of the limited electron impact ionization process. The interference of the continuum emission from plasma itself was reduced when the pressure decreased and iodine emissions became eminent compared with other emission signals. It is also recognized that the iodine emission at 183 nm (I-3) became eminent compared with other emission signals such as N-1 at 174.3 nm using 532 nm breakdown. This effect was also recognized by the laser breakdown time-of-flight mass spectrometry (LB-TOFMS) and it was observed that 532 nm can dissociate CH_3I much more efficiently compared to N_2 [122]. It is also worth noting that the lower electron density produced by 532 nm breakdown reduced the effect of electron impact ionization because of the lower efficiency of inverse bremsstrahlung process, which is approximately proportional to wavelength square [123].

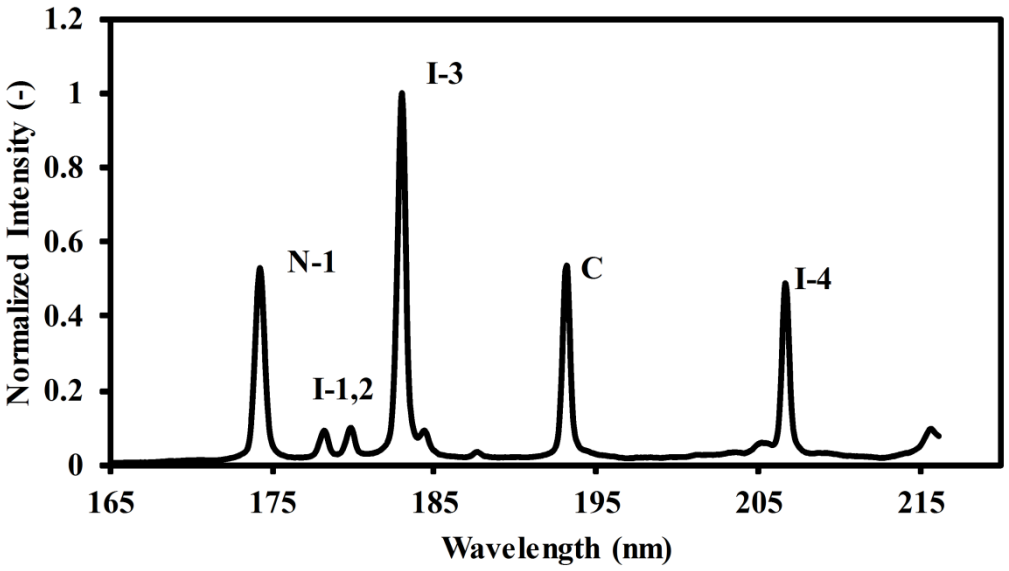

(a) ns 1064 nm breakdown

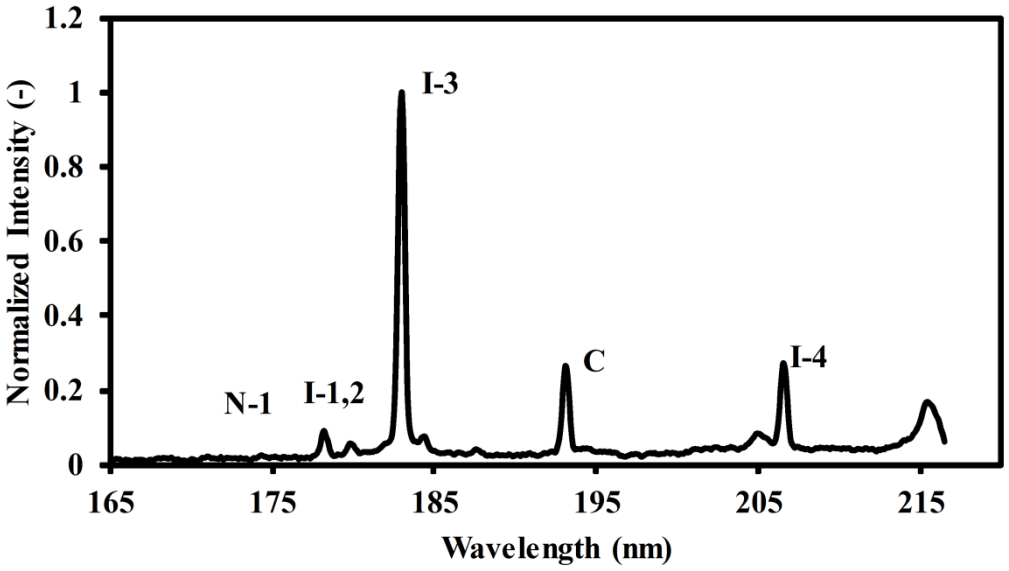

(b) ns 532 nm breakdown

Fig. 7.5 LIBS spectra of iodine signal at low pressure using nanosecond breakdown. Conditions: power 400 mJ/p, pressure 1300 Pa, delay time 1060 ns, gate width 30 μs, buffer gas N_2. The signal was normalized by iodine signal of I-3.

Employing ns 1064 nm breakdown with laser power of 400 mJ/p and 1000 mJ/p, iodine signal was measured under different pressure and delay time conditions. Nanosecond laser operated at 532 nm with power of 400 mJ/p was also employed to measure iodine under different conditions. When the pressure decreased, the effect of electron impact ionization can be reduced. As N_2 was the buffer gas, N emission at 174.3 nm (N-1) was determined as the coexisting atomic emissions to clarify the plasma generation process including the multiphoton ionization and electron impact ionization processes. Iodine emission at 183 nm (I-3) was set as a representative signal. Compared with the iodine signal at 183 nm (I-3), the N signal was mainly produced by the electron impact ionization process due to the higher upper level energy of N-1 emission. The intensity ratio of I-3 at 183 nm to N-1 at 174.3 nm was chosen to compare the breakdown characteristics.

Fig. 7.6 shows the delay time dependence of $I_{I\text{-}3}/I_{N\text{-}1}$ under different conditions. When the pressure reduced at low pressure area (less than 3000 Pa), the intensity ratio of I-3 to N-1 increased, which also demonstrated the satisfied results using low pressure LIBS. The intensity ratio of I-3 to N-1 also increased with an increase in delay time due to the lower upper level energy of iodine compared with that of N, as shown in Table 9.

Comparing the results using 1064 nm breakdown at different power, the intensity ratio of I-3 to N-1 using 400 mJ/p was better than that using 1000 mJ/p, as Fig. 7.6(a) and Fig. 7.6(b) show. The increased laser power strengthened the electron impact ionization process, which resulted in the

significant increase of N signal intensity. In the case of ns 532 nm breakdown, at low pressure of 700 Pa and 900 Pa, there was clear I-3 signal without N-1 signal at 174.3 nm because of the larger ionization and excitation processes. Compared Fig. 7.6(a) with Fig. 7.6(c), the intensity ratio of I-3 to N-1 was much higher in the case of 532 nm breakdown. This was occurred because of the different photon energy leading to the dissociation of CH3I. The photon energy of 532 nm is double compared with that of 1064 nm. Employing 532 nm breakdown, the multiphoton ionization process is much more efficient due to the higher photon energy, leading to the eminent iodine signal intensity at the same condition. Another reason was the efficient electron impact ionization by 1064 nm, resulting in the increase of signal intensity especially the N signal. All these two causes led to the higher intensity ratio of I-3 to N-1 using 532 nm breakdown.

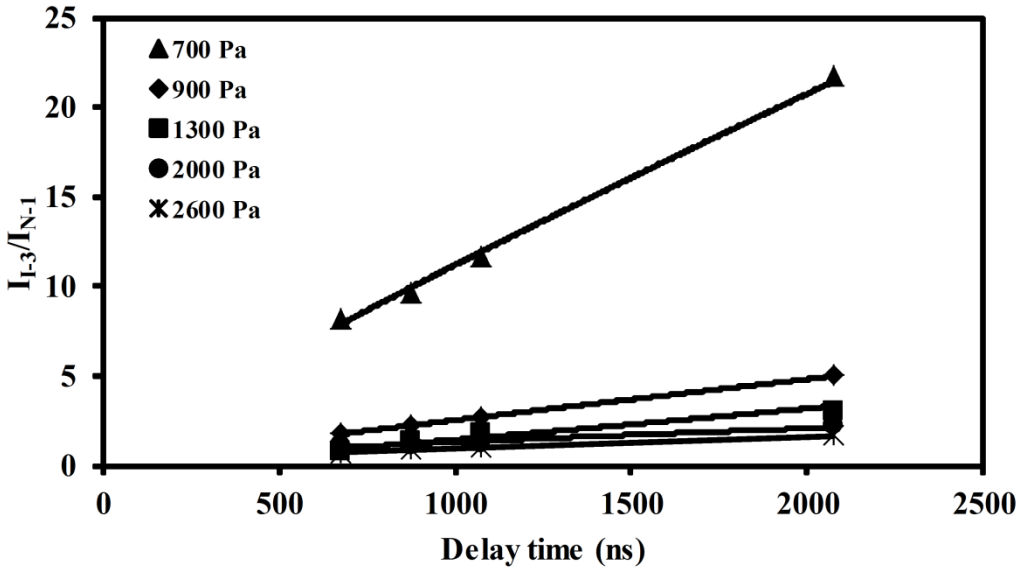

(a) Delay time dependence of I_{I-3}/I_{N-1} using ns 1064 nm breakdown at 400 mJ/p.

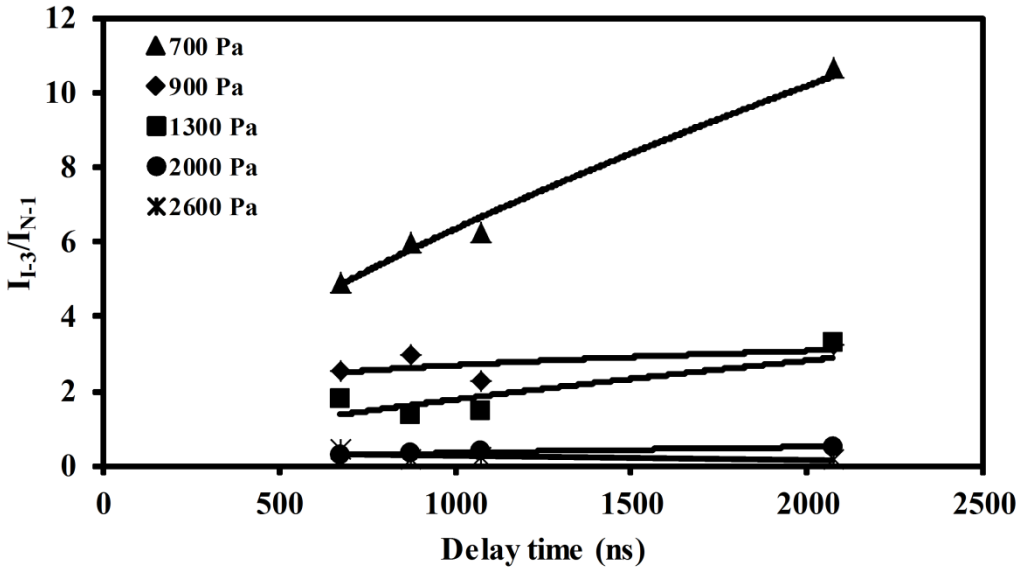

(b) Delay time dependence of I_{I-3}/I_{N-1} using ns 1064 nm breakdown at 1000 mJ/p.

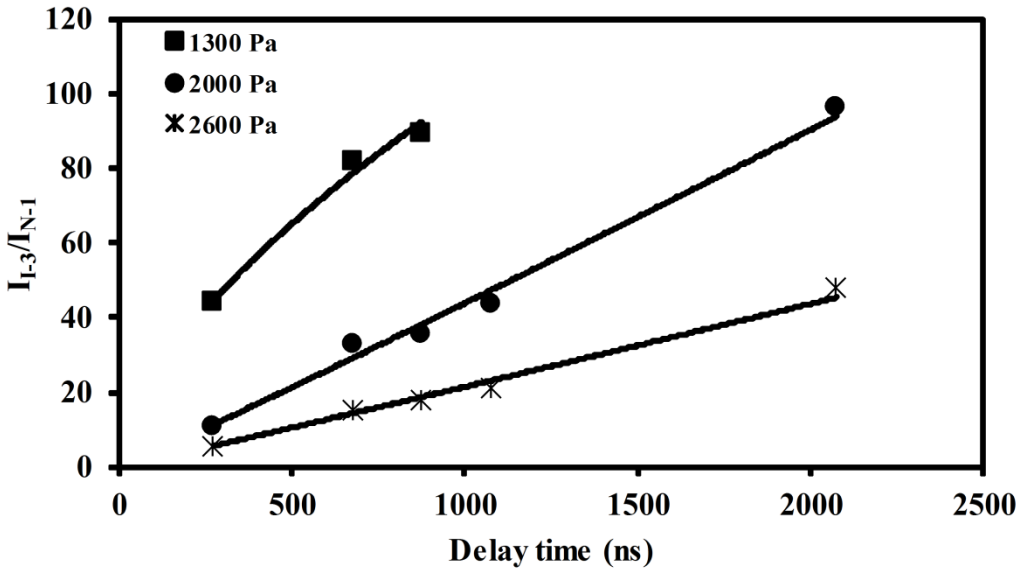

(c) Delay time dependence of I_{I-3}/I_{N-1} using ns 532 nm breakdown at 400 mJ/p.

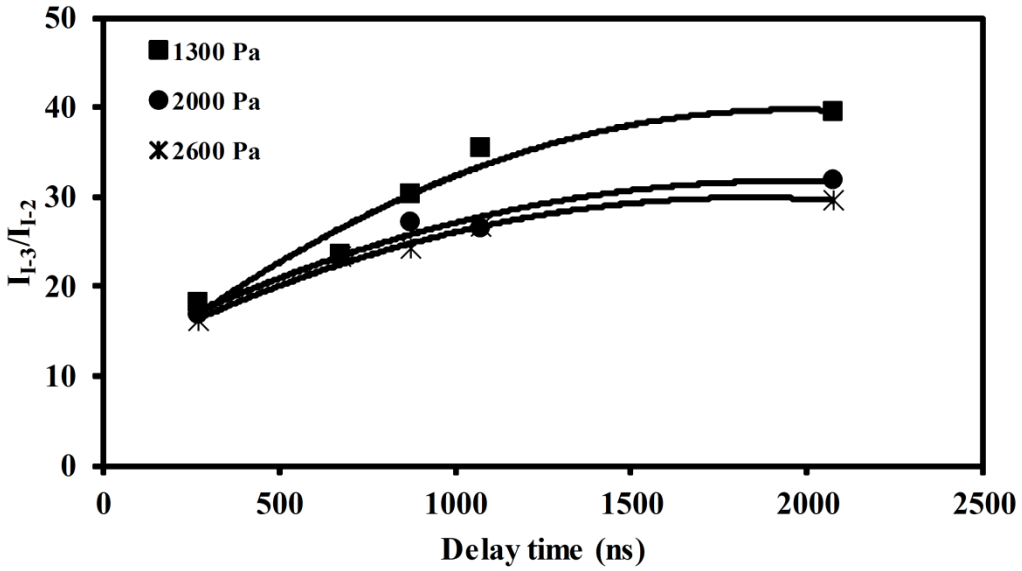

(d) Delay time dependence of I_{I-3}/I_{I-2} using ns 532 nm breakdown at 400 mJ/p.

Fig. 7.6 Delay time dependence of iodine signal at different pressure. Conditions: gate width 30 μs, buffer gas N_2.

As is known from these results, the plasma temperature reduced when the pressure decreased because the effect of electron impact ionization was reduced in these three cases. The intensity ratio of I-3 to N-1 increased at reduced pressure. Especially the large increase appeared at the lower pressure, such as 700 Pa using 1064 nm breakdown and 1300 Pa using 532 nm breakdown. The finding was explained by the comparison of delay time dependence of I_{I-3}/I_{N-1} and I_{I-3}/I_{I-2} at different pressure, as shown in Fig. 7.6(c) and Fig. 7.6(d). The intensity ratio of the emission pair of iodine atom can be used as an indicator of iodine temperature. Among iodine emission lines I_{I-3}/I_{I-2} was used as this indicator in this study, because there is enough difference of the upper level energies between I-2 and I-3. It is also mentioned that despite the upper level energy of I-4, the behavior of I-4 showed almost the same tendency as that of I-2 and I-4 is not suitable as an indicator in this study. We assume that there is a mixing of different emission lines at 206.2 nm or other effects such as resonant phenomena.

The increase of I_{I-3}/I_{I-2} means the decrease of temperature. These results confirmed the decrease of temperature with the increase of delay time and decrease of pressure. The difference of I_{I-3}/I_{I-2} between each pressure in same delay time was not similar to that of I_{I-3}/I_{N-1}. Therefore, the decrease of plasma temperature was not the only cause to increase the intensity ratio of I-3 to N-1 at reduced pressure and the discrepancy from the LTE condition at reduced pressure produced more population of iodine at excited levels. Even more important, the iodine can be ionized and excited largely at low pressure compared with the coexisting atom of N. The consistent results can also be

clarified in the cases of ns 1064 nm breakdown. However, the more significant larger ionization and excitation appeared when using 532 nm breakdown.

7.4.2 Picosecond breakdown of CH_3I in N_2 under different conditions

The laser-induced plasma process can be controlled by pressure and laser pulse width. Short pulse laser irradiation allowed for a specificity of excitation that could yield LIBS signals more tightly correlated to particular chemical species and showed significantly lower background emission. Short pulse lasers with pulse widths of 150 ps and 35 ps were employed to discuss the plasma generation process. Fig. 7.7 shows the measurement results of iodine emissions in N_2 using 150 ps and 35 ps lasers operated at 1064 nm, which indicates that the signal of I-3 was the main spectral line. Compared with Fig. 7.5(a), the iodine signal (I-3) became clearer using short pulse width breakdown. The coexisting atom emissions and the continuum emission from plasma itself were reduced when employing short pulse breakdown, especially 35 ps breakdown.

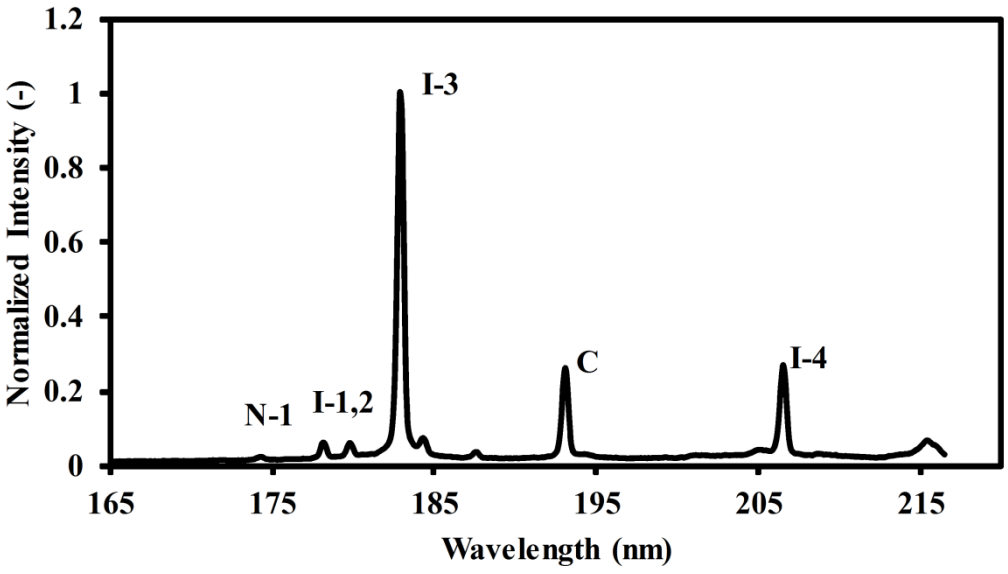

(a) 150 ps 1064 nm breakdown

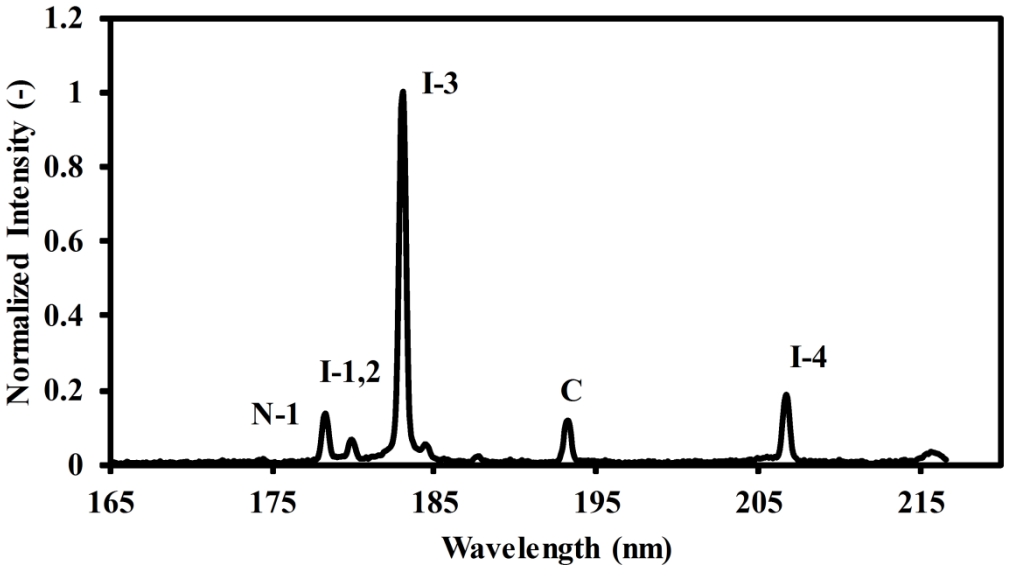

(b) 35 ps 1064 nm breakdown.

Fig. 7.7 LIBS spectra of iodine signal at low pressure using picosecond breakdown. Conditions: 150 ps laser at 1064 nm with power 150 mJ/p, 35 ps laser at 1064 nm with power 64 mJ/p, pressure 1300 Pa, delay time 1060 ns, gate width 30 μs, buffer gas N_2. The signal was normalized by iodine signal of I-3.

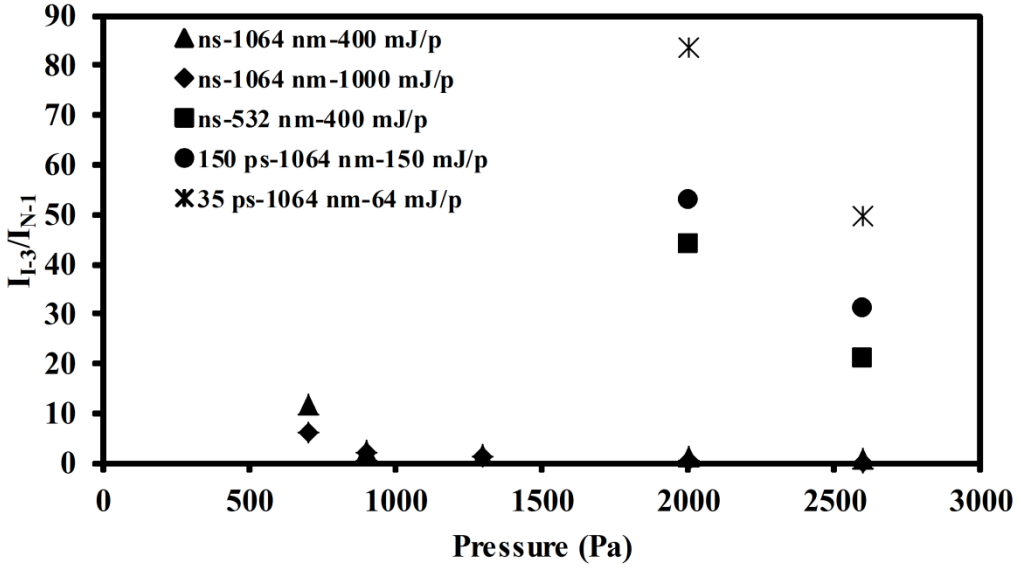

Fig. 7.8 Pressure dependence of I_{I-3}/I_{N-1} in N_2. Conditions: delay time 1060 ns, gate width 30 μs.

Under different pressure and delay time conditions, iodine signal was detected using these two

short pulse width lasers. Fig. 7.8 shows the pressure dependence of I_{I-3}/I_{N-1} under different breakdown conditions. When reducing the pressure, the intensity ratio of I-3 to N-1 increased in all cases. Short pulse width and short wavelength breakdown performed the improved intensity ratio of I-3 to N-1. Nanosecond breakdown at different power and wavelength has been already discussed in the previous section. Taking all the conditions into consideration, the reasons for the improved results were the control of the laser-induced plasma process, especially electron impact ionization process, and the larger ionization and excitation of iodine. The coexisting molecular and atomic emissions usually appear during the electron impact ionization process. The interference of coexisting atomic emission, i.e. N emission, was diminished employing short pulse width and short wavelength breakdown.

7.4.3 Detection limit of iodine in buffer gases of N_2 and air

Fig. 7.9 shows the concentration dependence of iodine signal intensity in buffer gas of N_2 using ns 1064 nm, ns 532 nm and 35 ps 1064 nm breakdowns. The results suggest the linear growth of the intensity of I-3 signal.

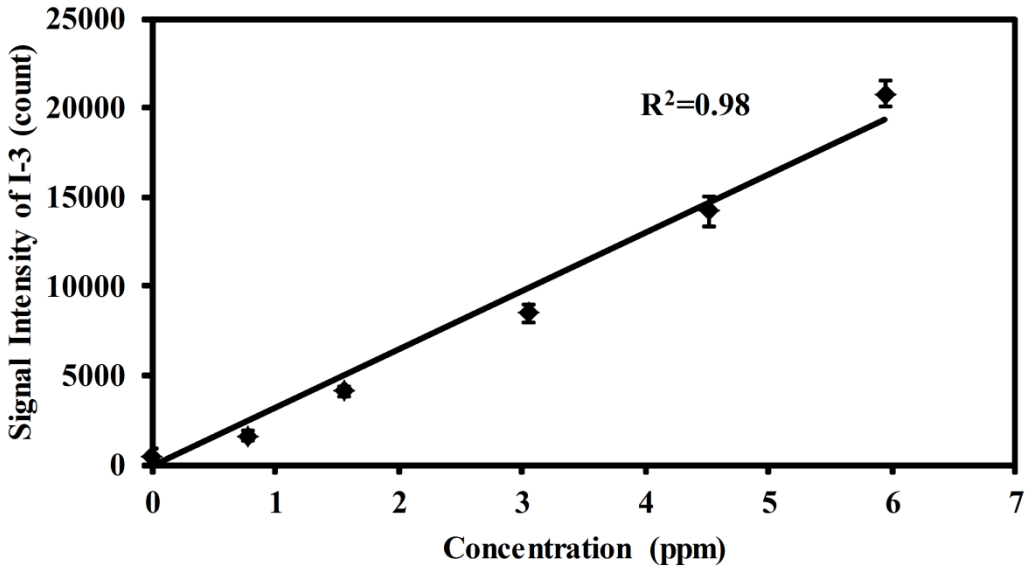

(a) ns 1064 nm breakdown. Conditions: power 400 mJ/p, pressure 700 Pa, delay time 1060 ns.

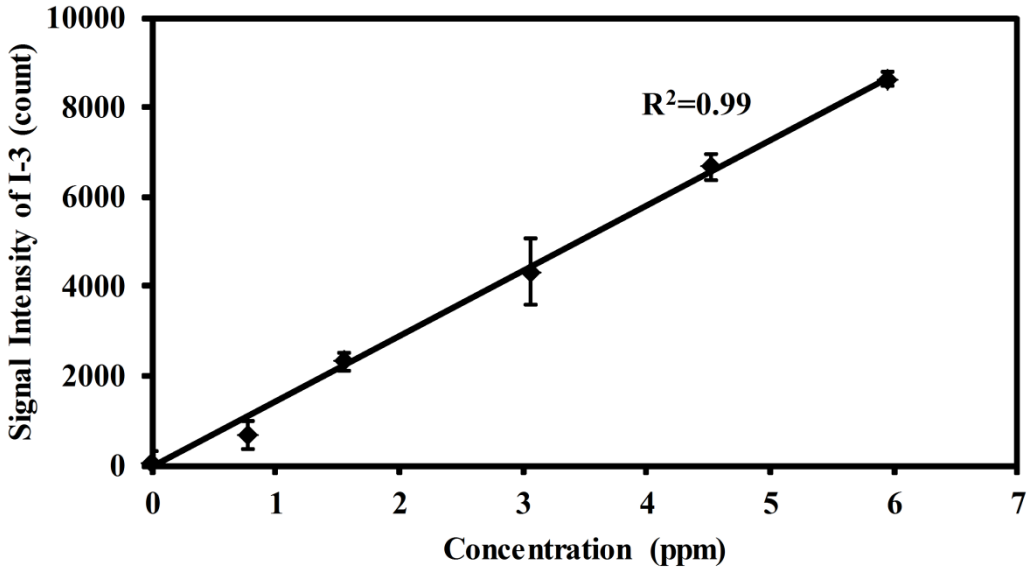

(b) ns 532 nm breakdown. Conditions: power 400 mJ/p, pressure 1300 Pa, delay time 260 ns.

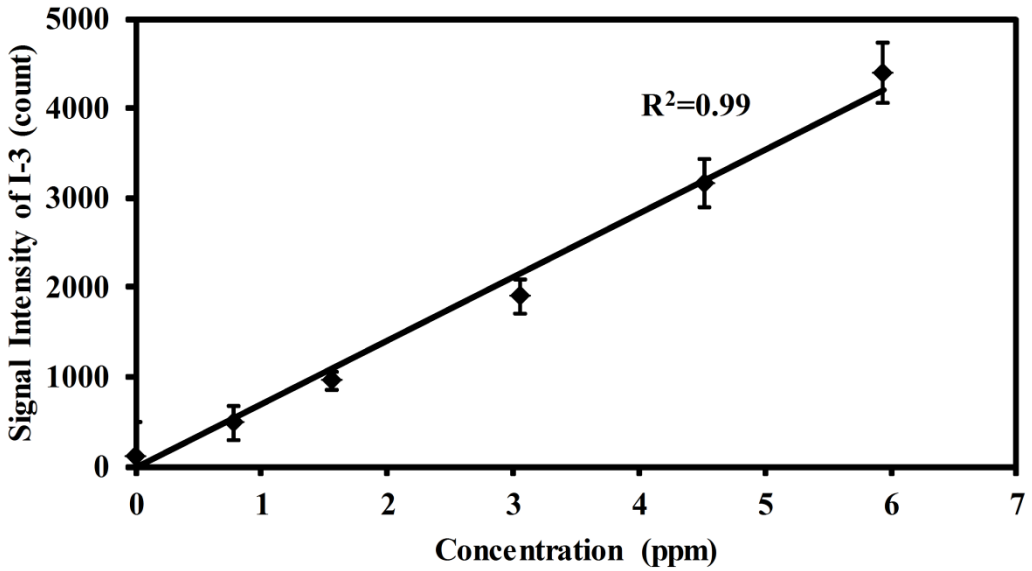

(c) 35 ps 1064 nm breakdown. Conditions: power 64 mJ/p, pressure 1300 Pa, delay time 260 ns.

Fig. 7.9 Concentration dependence of iodine signal intensity in N_2. Gate width 30 μs, buffer gas N_2. The error bar was denoted using the standard deviation of three times measurements.

Iodine was also measured in buffer gas of air to evaluate the buffer gas effect at reduced pressure conditions. O_2 absorption around 183 nm was not significant at such low pressure of 700 Pa inside the chamber because the absorption cross section of O_2 at 183 nm is around 10^{-21} cm^2 [112] and its effect is less than 1% according to the Beer-Lambert law. The LIBS spectra in buffer gas of air

were different from that in buffer gas of N_2 because of the reduction of iodine signal by the effect of oxygen. The iodine signal (I-3) at 183 nm was reduced markedly due to the high quenching rate of excited iodine in buffer gas of air. According to the results of 150 ps breakdown and 35 ps breakdown, the continuum emission from plasma itself was reduced when employing 35 ps breakdown, which led to the increase of signal to background ratio in the case of short pulse laser breakdown. These measurement results were consistent with those in buffer gas of N_2.

According the measurement results, the detection limit can be enhanced using low pressure LIBS. As for the measurement of iodine in N_2 at low pressure, the iodine detection limit of 600 shots (1 min) in buffer gas of N_2 was estimated by evaluating the ratio of the slope of the iodine signal calibration curve (m_s) to the background noise (standard deviation: σ). The iodine detection limit was 60 ppb ($3\sigma/m_s$) in nanosecond breakdown at pressure of 700 Pa. The background emission around I-3 at 183 nm was not eminent and the iodine detection limit was mainly determined by the detector noise in buffer gas of N_2. Therefore, there was not evident enhancement of iodine detection limit employing short pulse width breakdowns. The detection limit of iodine in air became worse due to the high quenching rate of excited iodine in buffer gas of air.

7.4 Summary

This study focused on the trace species of iodine measurement. Iodine in buffer gases of N_2 and air was measured using low pressure LIBS under different experimental conditions, i.e. pressure, delay time, pulse width, buffer gas etc. when employing standard gas of CH_3I to detect iodine signal.

1) Under low pressure conditions, the iodine signals, especially I-3 at 183 nm, were distinguished compared with that at higher pressure. The interference of the continuum emission from plasma itself reduced when the pressure decreased.

2) Nanosecond laser was employed to measure iodine signal under different pressure and delay time conditions. The intensity ratio of I-3 to N-1 was improved when reducing the pressure and increasing the delay time. Low laser power at 1064 nm breakdown and short wavelength of 532 nm breakdown performed the improved intensity ratio of I-3 to N-1 due to the control of the electron impact ionization process and the efficiently larger ionization and excitation of iodine.

3) The plasma generation process was controlled by the pulse width except for the pressure. Short pulse width lasers including 150 ps and 35 ps lasers were employed to measure iodine signal. The intensity ratio of I-3 to N-1 was enhanced using short pulse width lasers, especially 35 ps laser.

4) The spectra in air were different from that in N_2 due to the high quenching rate of excited iodine in buffer gas of air. Using low pressure LIBS, it is feasible to measure iodine in air, especially short pulse laser breakdown. The detection limit of iodine in N_2 was 60 ppb (3σ/ms) in nanosecond breakdown at pressure of 700 Pa.

CHAPTER 8. CONCLUSIONS AND SUGGESTIONS

8.1. Conclusions

As presented in previous chapters, the laser-induced gas plasma generation, interaction between laser and weakly ionized plasma, the resultant energy spot as well as the application of gas plasma in LIBS for iodine measurement are investigated. In this chapter, a brief summary of the whole research and major conclusions obtained in the study are given.

Propagation of laser beam can be modeled by Maxwell equation and then solved by FDTD method. Usually the laser beam can be simplified as a Gaussian beam. To eliminate the false numerical reflection in FDTD, the perfectly matched absorbing boundary condition should be adopted in the computational region. The pulse width of the numerical laser beam can be numerical control a Gaussian function in time domain.

The gas plasma generation as well as interaction between laser and plasma can be modeled by the proposed hybrid model, in which laser is modeled by Maxwell equation, particle evolution by continuous Boltzmann equations and energy transition and transformation by Navier-Stokes. The solution of the hybrid model can be solved by combination of FDTD, LBM and FNM. When compared with the molecular dynamic numerical method, the proposed model can save computational cost because it does not need to solve mechanical equation for every particle. When compared with the macroscopic methods, the continuum assumption is truncated that leads the more refine solution of plasma chemistry.

In the generation of plasma spark, free electrons are usually produced by MPI in the focal spot laser beam. Under Lorentz force of electromagnetic field of the laser, the existing electrons are accelerated sharply and obtain huge kinetic energy in a short time. When kinetic energy of electrons is enough to nourish the ionization potential of neutrals, there may be new electrons produced in collisions between electrons and neutrals. At the same time, some kinetic energy of electrons loses to be converted into the internal energy in collisions with neutrals, so temperature of electrons increases. For ions, because of the mass is much larger comparing to electrons, their accelerated and heated processes are slower. In interaction between laser and weakly ionized plasma, the physical heating patters of the particles in the plasma due to the laser energy deposition. The ionization and recombination dynamics and its effects on the heating and generation of free electrons are also il1ustrated from the simulation results.

In evolution of energy spot, the shape is firstly as ellipsoid and then as sphere. In the initial phase of spot evolution, the high pressure and high temperature are coincident. The propagation of shock wave is much faster than diffusion of high temperature spot. This makes the dislocation of high

pressure and high temperature areas. Besides because of the propagation of the shock wave, excessive expansion happens for fluid in the core of spark. This will lead the negative pressure of the spot core when compared with the ambient gas. The cold ambient can thus inject into the core of plasma, which leads the formation of a ring form of high temperature unit.

Because of the reduced particle collisions, multiphoton ionization is the main source for gas breakdown in low ambient pressure. The subdued electron impact ionization can weaken absorption of laser energy by plasma, which can reduce the continuum plasma emission interference for iodine measurement in LIBS. Compared with 1064 nm Nd:YAG laser beam, the photon energy of 532 nm laser is doubled. The multiphoton ionization process is thus much more efficient, which lead to the improved iodine signal intensity at the same condition. Laser pulse width can also control the laser breakdown process. Short pulse laser irradiation allows for a specificity of excitation that can yield LIBS signal more tightly correlated to particular chemical species and shows significantly lower background emission.

8.2. Suggestions

Modeling laser-induced gas spark formation and evolution is a challenging problem since it involves a number of physical processes including air breakdown chemistry, interaction between particles and electromagnetic waves, interaction between laser and plasma, propagation of strong shock waves. However the hybrid model proposed in this dissertation is valuable attempt to handle these complex processes. The following measures may be feasible for progressive simulation of laser spark.

The beam waist is roughly several millimeters in size for frequently-used Nd:YAG laser system in laser-induced spark generation. And the wavelength of the laser beam is 1064 nm or 532 nm. The stability of FDTD requires that the space step cannot be larger than one tenth of the wavelength. The rough mesh number of is thus more than 3 billion for simplified two-dimensional simulation of real-time laser beam, which will bring oppressive computation cost. To solve this problem, some memory saving numerical schemes derived from the standard FDTD method, such as the alternating direction implicit finite difference time domain (ADI-FDTD) method, should be adopted into the hybrid model.

Laser-induced gas spark generation as well as the resultant fluid dynamic evolution is compressible process in which the gas compression ratio can reach to 100. The model in charge of plasma should be capable to handle compressible fluid flows with high compression ratio. Thus the compressible LB models should be used. Mostly the compressible LB models also can handle the energy transition and transformation processes of fluids, so their adoption can further saving the computational cost. Complex non-local-thermodynamic-equilibrium conditions exist in plasma generation and growth processes, the appropriate measures for non-equilibrium effects should be

also considered.

As presented in chapter 7, utilization of low ambient pressure as well as shortly laser pulse in LIBS technology can improve the measurement limit of iodine. While the background spectroscopy interferences are very complex in real air, the LIBS technology used for iodine measurement in real air should be studied in more detailed.

REFERENCES

[1] E. W. Davis and F. B. Mead, "Review Of Laser Lightcraft Propulsion System," in AIP Conference Proceedings, 2007, pp. 283-294.

[2] T.-S. Wang, et al., "Advanced Performance Modeling of Experimental Laser Lightcraft," Journal of propulsion and power, vol. 18, pp. 1129-1138, 2002.

[3] L. Chen, et al., Laser Supported Detonation Wave. Beijing: National defense industrial press, 2011.

[4] R. Kandala and G. Candler, "Numerical Studies of Laser-Induced Energy Deposition for Supersonic Flow Control," AIAA Journal, vol. 42, pp. 2266-2275, 2004.

[5] D. Riggins, et al., "Blunt-Body Wave Drag Reduction Using Focused Energy Deposition," AIAA Journal, vol. 37, pp. 460-467, 1999.

[6] T. X. Phuoc, "Laser-induced spark ignition fundamental and applications," Optics and Lasers in Engineering, vol. 44, pp. 351-397, 2006.

[7] Y. Deguchi, Industrial applications of laser diagnostics. Florida: CRC Press, Taylor & Francis Group, 2011.

[8] X. Wang, et al., "Observation of Raman scattering and hard X-rays in short pulse laser interaction with high density hydrogen gas," Optics communications, vol. 146, pp. 363-370, 1998.

[9] A. N. Pirri, et al., "Momentum transfer and plasma formation above a surface with a high-power CO_2 laser," Applied Physics Letters, vol. 21, pp. 79-81, 1972.

[10] K. D. Song and D. R. Alexander, "Propagation velocities of laser-produced plasmas from copper wire targets and water droplets," Journal of Applied Physics, vol. 76, pp. 3302-3312, 1994.

[11] S. S. Harilal and B. Harilal, "Diagnostics of laser induced spark in air using fast ICCD photography," Laser Plasma and Laser Matter Interactions Laboratory, University of California, San Diego2002.

[12] C. V. Bindhu, et al., "Laser propagation and energy absorption by an argon spark," Journal of Applied Physics, vol. 94, pp. 7402-7407, 2003.

[13] C. V. Bindhu, et al., "Energy absorption and propagation in laser-created sparks," Applied Spectroscopy, vol. 58, pp. 719-726, 2004.

[14] D. Nassif and L. Huwel, "Appearance of toroidal structure in dissipating laser-generated sparks," Journal of Applied Physics, vol. 87, pp. 2127-2130, 2000.

[15] M. Longenecker, et al., "Laser-generated spark morphology and temperature records from emission and Rayleigh scattering studies," Applied Optics, vol. 42, pp. 990-996, 2003.

[16] N. Glumac, et al., "Temporal and spatial evolution of a laser spark in air," AIAA Journal, vol. 42, pp. 1984-1994, 2005.

[17] Y. L. Chen and J. Lewis, "Visualization of laser-induced breakdown and ignition," Optics Express, vol. 9, pp. 360-372, 2001.

[18] D. R. Keefer, et al., "Experimental study of a stationary laser−sustained air plasma," Journal of Applied Physics, vol. 46, pp. 1080-1083, 1975.

[19] S. Yalcin, et al., "Influence of ambient conditions on the laser air spark," Applied Physics B: Lasers and Optics, vol. 68, pp. 121-130, 1999.

[20] S. S. Harilal, "Spatial and temporal evolution of argon sparks," Applied Optics, vol. 43, pp. 3931-3937, 2004.

[21] S. Joshi, et al., "Temperature and electron density measurements of laser-induced plasmas in air at elevated pressures," Spectroscopy Letters, vol. 44, pp. 103-112, 2011.

[22] D. C. Smith, "Gas breakdown with 10.6 μm wavelength CO_2 laser radiation," Journal of Applied Physics, vol. 41, pp. 4501-4505, 1970.

[23] K. Takahashi, et al., "Study on laser plasma generation by high-speed photography," Kyushu University2001.

[24] V. D. Zvorykin, "Comparative analysis of gas dynamic regimes of high-power UV and IR gas laser interactions with solids in the atmosphere," in Proc. SPIE,High-Power Laser Ablation III

4065, 2000, pp. 128-139.
[25] K. Mori, et al., "Influence of the focusing f number on the heating regime transition in laser absorption waves," Journal of Applied Physics, vol. 92, pp. 5663-5667, 2002.
[26] Z. Sun, "The Application of Direct Simulation Monte-Carlo Method for Solving Multiscale Problems," PhD, Powere Engineering and Engineering Thermophysics, Xi'an Jiaotong University, Xi'an, 2011.
[27] C. K. Aidun and J. R. Clausen, "Lattice-Boltzmann method for complex flows," Annual Review of Fluid Mechanics, vol. 42, pp. 439-472, 2010.
[28] T. E. Itina, Tokarev, V. N., Marine, W., & Autric, M. , "Monte Carlo simulation study of the effects of nonequilibrium chemical reactions during pulsed laser desorption," Journal of Chemical Physics, vol. 106, pp. 8905-8912, 1997.
[29] S. O'Connell and P. Thompson, "Molecular dynamics–continuum hybrid computations: A tool for studying complex fluid flows," Physical Review E, vol. 52, pp. R5792-R5795, 1995.
[30] P. E. Nielsen, "Hydrodynamic calculations of surface response in the presence of laser-supported detonation waves," Journal of Applied Physics, vol. 46, p. 4501, 1975.
[31] N. Ferriter, et al., "Laser-beam optimization for momentum transfer by laser-supported detonation waves," AIAA Journal, vol. 15, pp. 1597-1603, 1977.
[32] T. Oshima and T. Fujiwara, "A Numerical Study on the Characters of Laser-Supported Detonation Wave," SAE Technical Paper 912082, 1991.
[33] P. M. Morales, et al., "CFD simulation of 2 kw class laser thruster," AIAA 2001-0650, 2001.
[34] R. C. Kandala, GV, "Numerical Studies of Laser-Induced Energy Deposition for Supersonic Flow Control," AIAA Journal, vol. 42, pp. 2266-2275, 2003.
[35] Z. Duan, et al., "Theoretical modeling and trans-scale simulation of coupling fields generated by the explosion of a focused high power laser beam," Advances in Mechanics, vol. 39, pp. 467-479, 2009.
[36] R. Akarapu, et al., "Numerical model of a laser-sustained argon plasma," Journal of laser applications, vol. 21, 2009.
[37] I. G. Dors and C. G. Parigger, "Computational Fluid-Dynamic Model of Laser-Induced Breakdown in Air," Applied Optics, vol. 42, pp. 5978-5985, 2003.
[38] H. Yan, et al., "Laser energy deposition in quiescent air," AIAA Journal, vol. 41, pp. 1988-1995, 2003.
[39] K. Mori, "Energy transfer from a laser pulse to a blast wave in reduced-pressure air atmospheres," Journal of Applied Physics, vol. 95, p. 5979, 2004.
[40] H. Shiraishi, "Fundamental Properties of Non-equilibrium Laser-Supported Detonation Wave," vol. 702, pp. 68-79, 2004.
[41] S. Ghosh and K. Mahesh, "Numerical simulation of the fluid dynamic effects of laser energy deposition in air," Journal of Fluid Mechanics, vol. 605, 2008.
[42] S. Longo, "Monte Carlo models of electron and ion transport in non-equilibrium plasmas," Plasma Sources Science and Technology, vol. 9, pp. 468-476, 2000.
[43] A. Müsing, et al., "Laser-induced breakdown in air and behind droplets: A detailed Monte-Carlo simulation," Proceedings of the Combustion Institute, vol. 31, pp. 3007-3014, 2007.
[44] G. Tartar, et al., "Simulation of optical breakdown in nitrogen by focused short laser pulses of 1064 nm wavelength," Laser and Particle Beams, vol. 26, p. 567, 2008.
[45] H. Li and H. Ki, "Lattice Boltzmann method for weakly ionized isothermal plasmas," Physical Review E, vol. 76, 2007.
[46] H. Li and H. Ki, "Lattice Boltzmann simulation of weakly ionized plasmas and fluid flows using physical properties of fluids," Journal of Physics A: Mathematical and Theoretical, vol. 42, p. 155501, 2009.
[47] H. Li and H. Ki, "Simulation of MHD flows using a hybrid lattice-Boltzmann finite-difference method," Communications in computational physics, vol. 4, pp. 337-349, 2008.
[48] H. Li and H. Ki, "Lattice-Boltzmann simulation of laser interaction with weakly ionized helium plasmas," Physical Review E, vol. 82, p. 016703, 2010.
[49] P. Lambropoulos, "Topics on multiphoton processes in atoms," Advances in Atomic and

Molecular Physics, vol. 12, pp. 87-164, 1976.
[50] S. L. Chin, "Multiphoton ionization of atoms," Univ. Laval, Quebec1984.
[51] T. X. Phuoc, "Laser spark ignition: experimental determination of laser-induced breakdown thresholds of combustion gases," Optics Communications, vol. 175, pp. 419-423, 2000.
[52] C. G. Morgan, "Laser-induced breakdown of gases," Reports on Progress in Physics, vol. 38, p. 621, 1975.
[53] Y. B. Zel'dovich and Y. P. Raizer, Eds., Physics of Shock Waves and High-Temperature Hydrodynamic Phenomena: Volume I. New York: Academic Press, 1966, p.^pp. Pages.
[54] V. Granovskii, "Electric Current in a Gas," Vol. 1. General Problems of the Electrodynamics of Gases, 1971.
[55] A. Gurevich and L. Pitaevskii, "Recombination coefficient in a dense low temperature plasma," Zh. Eksperim. i Teor. Fiz., vol. 46, 1964.
[56] G. Taylor, "The formation of a blast wave by a very intense explosion. I. Theoretical discussion," Proceedings of the Royal Society of London. Series A, Mathematical and Physical Sciences, vol. 201, pp. 159-174, 1950.
[57] T.-S. Wang, et al., "Advanced performance modeling of experimental laser lightcraft," Journal of Propulsion and Power, vol. 18, pp. 1129-1138, 2002.
[58] Y. Deguchi, Industrial applications of laser diagnostics. New York: CRC Press, 2011.
[59] D. Riggins, et al., "Blunt-body wave drag reduction using focused energy deposition," AIAA Journal, vol. 37, pp. 460-467, 1999.
[60] C. Bindhu, et al., "Energy absorption and propagation in laser-created sparks," Applied Spectroscopy, vol. 58, pp. 719-726, 2004.
[61] C. Bindhu, et al., "Laser propagation and energy absorption by an argon spark," Journal of Applied Physics, vol. 94, pp. 7402-7407, 2003.
[62] D. Nassif and L. Hüwel, "Appearance of toroidal structure in dissipating laser-generated sparks," Journal of Applied Physics, vol. 87, pp. 2127-2130, 2000.
[63] M. Longenecker, et al., "Laser-generated spark morphology and temperature records from emission and Rayleigh scattering studies," Applied Optics, vol. 42, pp. 990-996, 2003.
[64] N. Glumac and G. Elliott, "The effect of ambient pressure on laser-induced plasmas in air," Optics and Lasers in Engineering, vol. 45, pp. 27-35, 2007.
[65] Y.-L. Chen and J. Lewis, "Visualization of laser-induced breakdown and ignition," Optics Express, vol. 9, pp. 360-372, 2001.
[66] E. Schwarz, et al., "Laser-induced optical breakdown applied for laser spark ignition," Laser and Particle Beams, vol. 28, pp. 109-119, 2010.
[67] S. Yalcin, et al., "Influence of ambient conditions on the laser air spark," Applied Physics B: Lasers and Optics, vol. 68, pp. 121-130, 1999.
[68] N. G. Glumac, et al., "Temporal and spatial evolution of a laser spark in air," AIAA Journal, vol. 43, pp. 1984-1994, 2005.
[69] R. Kandala and G. Candler, "Numerical studies of laser-induced energy deposition for supersonic flow control," AIAA Journal, vol. 42, pp. 2266-2275, 2003.
[70] H. Metghalchi, et al., "A thermodynamic model for argon plasma kernel formation," International Journal of Thermodynamics, vol. 13, pp. 119-125, 2010.
[71] R. Akarapu, et al., "Numerical model of a laser-sustained argon plasma," Journal of Laser Applications, vol. 21, pp. 169-175, 2010.
[72] W. Chen, et al., "Critical analysis of viscosity data of thermal argon plasmas at atmospheric pressure," Plasma chemistry and plasma processing, vol. 16, pp. 635-650, 1996.
[73] A. Murphy and C. Arundelli, "Transport coefficients of argon, nitrogen, oxygen, argon-nitrogen, and argon-oxygen plasmas," Plasma chemistry and plasma processing, vol. 14, pp. 451-490, 1994.
[74] R. Devoto, "Transport coefficients of ionized argon," Physics of Fluids (1958-1988), vol. 16, pp. 616-623, 2003.
[75] K. S. Drellishak, et al., "Partition functions and thermodynamic properties of argon plasma," Physics of Fluids (1958-1988), vol. 6, pp. 1280-1288, 2004.
[76] B. J. McBride and S. Gordon, Computer program for calculating and fitting thermodynamic

functions vol. 1271: National Aeronautics and Space Administration, Office of Management, Scientific and Technical Information Program, 1992.
[77] M. I. Hoffert and H. Lien, "Quasi-One-Dimensional, Nonequilibrium Gas Dynamics of Partially Ionized Two-Temperature Argon," Physics of Fluids (1958-1988), vol. 10, pp. 1769-1777, 2004.
[78] T. Owano, et al., "Electron-ion three-body recombination coefficient of argon," AIAA journal, vol. 31, pp. 75-82, 1993.
[79] A. Kramida, et al. NIST Atomic Spectra Database(ver. 5.1), [Online]. [Online].
[80] K. Eisazadeh-Far, et al., "Thermodynamic Properties of Ionized Gases at High Temperatures," Journal of Energy Resources Technology, vol. 133, p. 022201, 2011.
[81] K. Yee, "Numerical solution of initial boundary value problems involving Maxwell's equations in isotropic media," Antennas and Propagation, IEEE Transactions on, vol. 14, pp. 302-307, 1966.
[82] J.-P. Berenger, "A perfectly matched layer for the absorption of electromagnetic waves," Journal of computational physics, vol. 114, pp. 185-200, 1994.
[83] J. A. Bittencourt, Fundamentals of plasma physics: Springer, 2004.
[84] T. I. Gombosi, Gaskinetic theory: Cambridge University Press, 1994.
[85] Y.-L. He, et al., Lattice Boltzmann Method: Theory and Application. Beijing: Science Press, 2009.
[86] P. L. Bhatnagar, et al., "A model for collision processes in gases. I. Small amplitude processes in charged and neutral one-component systems," Physical review, vol. 94, p. 511, 1954.
[87] G. R. McNamara and G. Zanetti, "Use of the Boltzmann equation to simulate lattice-gas automata," Physical Review Letters, vol. 61, pp. 2332-2335, 1988.
[88] X. He and L.-S. Luo, "Theory of the lattice Boltzmann method From the Boltzmann equation to the lattice Boltzmann equation," Physical Review E vol. 56, pp. 6811-6817, 1997.
[89] X. He and L.-S. Luo, "A priori derivation of the lattice Boltzmann equation," Physical Review E, vol. 55, pp. 6333-6336, 1997.
[90] Y. Qian, et al., "Lattice BGK models for Navier-Stokes equation," EPL (Europhysics Letters), vol. 17, p. 479, 2007.
[91] X. Shan and H. Chen, "Lattice Boltzmann model for simulating flows with multiple phases and components," Physical Review E, vol. 47, p. 1815, 1993.
[92] X. Shan and G. Doolen, "Multicomponent lattice-Boltzmann model with interparticle interaction," Journal of Statistical Physics, vol. 81, pp. 379-393, 1995.
[93] Z.-L. Guo and C.-G Zheng, Theory and Applications of Lattice Boltzmann Method. Beijing: Science Press, 2009.
[94] X. He, et al., "Analytic solutions of simple flows and analysis of nonslip boundary conditions for the lattice Boltzmann BGK model," Journal of Statistical Physics, vol. 87, pp. 115-136, 1997.
[95] X. He, et al., "Discrete Boltzmann equation model for nonideal gases," Physical Review E, vol. 57, pp. 13-16, 1998.
[96] L.-S. Luo, "Unified Theory of Lattice Boltzmann Models for Nonideal Gases," Phys. Rev. Lett. , vol. 81, pp. 1618-1621, 1998.
[97] Z. Guo, et al., "Discrete lattice effects on the forcing term in the lattice Boltzmann method," Physical Review E, vol. 65, 2002.
[98] Q. Chen and B. Chen, "Hybrid electrodynamics and kinetics simulation for electromagnetic wave propagation in weakly ionized hydrogen plasmas," Physical Review E, vol. 86, p. 046704, 2012.
[99] N. Cao, et al., "Physical symmetry and lattice symmetry in the lattice Boltzmann method," Physical Review E, vol. 55, pp. R21-R24, 1997.
[100] R. Mei and W. Shyy, "On the finite difference-based lattice Boltzmann method in curvilinear coordinates," Journal of Computational Physics, vol. 143, pp. 426-448, 1998.
[101] Z. Guo and T. S. Zhao, "Explicit finite-difference lattice Boltzmann method for curvilinear coordinates," Physical Review E, vol. 67, p. 066709, 2003.
[102] Y. Wang, et al., "Implicit-explicit finite-difference lattice Boltzmann method for

compressible flows," International Journal of Modern Physics C, vol. 18, pp. 1961-1983, 2007.
[103] T. Kataoka and M. Tsutahara, "Lattice Boltzmann method for the compressible Euler equations," Physical Review E, vol. 69, 2004.
[104] B. Van Leer, "Towards the ultimate conservative difference scheme. V. A second-order sequel to Godunov's method," Journal of Computational Physics, vol. 32, pp. 101-136, 1979.
[105] G.-S. Jiang and C.-W. Shu, "Efficient implementation of weighted ENO schemes," DTIC Document1995.
[106] S. Hou, et al., "Simulation of cavity flow by the lattice Boltzmann method," Journal of Computational Physics, vol. 118, pp. 329-347, 1995.
[107] T. Makabe and Z. Petrovic, Plasma electronics: applications in microelectronic device fabrication: Taylor & Francis, 2006.
[108] W.-Q Tao, Numerical Heat Transfer, 2nd ed. Xi'an: Xi'an Jiaotong University Press, 2001.
[109] A. Taflove and S. C. Hagness, Computational electrodynamics vol. 160: Artech house BostonLondon, 2000.
[110] G.-W Yan, D.-B Ge, Finite Difference Time Domain Method, 3rd ed. Xi'an: Xidian University Press, 2011.
[111] S. Mishra, et al., "Determination of iodide by derivatization to 4-iodo-N, N-dimethylaniline and gas chromatography–mass spectrometry," Analyst, vol. 125, pp. 459-464, 2000.
[112] M. Ogawa, "Absorption Cross Sections of O_2 and CO_2 Continua in the Schumann and Far UV Regions," The Journal of Chemical Physics, vol. 54, pp. 2550-2556, 2003.
[113] S. Zhang, et al., "A Novel Approach for the Simultaneous Determination of Iodide, Iodate and Organo-Iodide for 127I and 129I in Environmental Samples Using Gas Chromatography− Mass Spectrometry," Environmental science & technology, vol. 44, pp. 9042-9048, 2010.
[114] R.-J. Huang, et al., "Extensive evaluation of a diffusion denuder technique for the quantification of atmospheric stable and radioactive molecular iodine," Environmental science & technology, vol. 44, pp. 5061-5066, 2010.
[115] P. Bienvenu, et al., "Determination of iodine 129 by ICP-QMS in environmental samples," Canadian journal of analytical sciences and spectroscopy, vol. 49, pp. 423-428, 2004.
[116] T. Nakahara and T. Mori, "Analyte volatilization procedure for the determination of low concentrations of iodine by inductively coupled plasma atomic emission spectrometry. Invited lecture," J. Anal. At. Spectrom., vol. 9, pp. 159-165, 1994.
[117] A. A. Oliveira, et al., "Review: iodine determination by inductively coupled plasma spectrometry," Applied Spectroscopy Reviews, vol. 45, pp. 447-473, 2010.
[118] P. Grinberg and R. E. Sturgeon, "Ultra-trace determination of iodine in sediments and biological material using UV photochemical generation-inductively coupled plasma mass spectrometry," Spectrochimica Acta Part B: Atomic Spectroscopy, vol. 64, pp. 235-241, 2009.
[119] M. R. Leahy-Hoppa, et al., "Ultrafast laser-based spectroscopy and sensing: applications in LIBS, CARS, and THz spectroscopy," Sensors, vol. 10, pp. 4342-4372, 2010.
[120] K. L. Eland, et al., "Some comparisons of LIBS measurements using nanosecond and picosecond laser pulses," Applied Spectroscopy, vol. 55, pp. 279-285, 2001.
[121] G. Cristoforetti, et al., "Thermodynamic equilibrium states in laser-induced plasmas: From the general case to laser-induced breakdown spectroscopy plasmas," Spectrochimica Acta Part B: Atomic Spectroscopy, vol. 90, pp. 1-22, 2013.
[122] Z. Z. Wang, et al., "Rapid Detection of Mercury and Iodine Using Laser Breakdown Time-Of-flight Mass Spectrometry," Spectroscopy Letters, 2014.
[123] L. Cabalin and J. Laserna, "Experimental determination of laser induced breakdown thresholds of metals under nanosecond Q-switched laser operation," Spectrochimica Acta Part B: Atomic Spectroscopy, vol. 53, pp. 723-730, 1998.

ACKNOWLEDGEMENTS

I especially would like to express my sincerest gratitude to Prof. Yoshihiro Deguchi from the University of Tokushima and Prof. Jiping Liu from Xi'an Jiaotong University for giving me a chance to study as a Ph.D. student in their laboratories, and for their guidance, support and encouragement. Their advice and suggestions have been invaluable to my study.

Secondly, I would like to thank the Double Degree Program between Xi'an Jiaotong University and the University of Tokushima. It provides a good chance for me to study abroad and offers a financial support for my study. I would like to thank Assistant Prof. Koji for his guidance and helpful suggestion in my research. Thanks all the members in CICEE, Dr. Pankaj Koinka, Dr. Walter Carpenter, Dr. Pangpang Wang, Dr. Dongyan Zhang and Mrs. Asada.

Then, I would like to thank all the members in the research group. Thanks Dr. Zhenzhen Wang, M.E. Shinichirou Konishi, M.E. Masakazu Kuwahara, M.E. Koichi Imanaka and M.E. Keqiang Chen.

Finally, on a more personal note, I wish to express my deepest appreciation to my family for their endless support, encouragement sacrifice and love. Especially, thanks my wife for her love and accompanying.

LIST OF PUBLICATIONS

Journals:

1. Xiaobo Zhang, Jiping Liu, Kai Wang, Junjie Yan and Danghui Hu: "Experimental study on singular temperature profiles in a tube to periodical heating at end", *Journal of Engineering Thermophysics*, Vol.32: 281-283, 2011. (in Chinese)
2. Xiaobo Zhang, Yoshihiro Deguchi, and Jiping Liu: "Numerical simulation of laser induced weakly ionized Helium plasma process by lattice Boltzmann method", *Japanese Journal of Applied Physics*, Vol.51: 01AA04, 2012.
3. Xiaobo Zhang, Yoshihiro Deguchi, Zhenzhen Wang, Junjie Yan and Jiping Liu: 2014 "Sensitive detection of iodine by low pressure and short pulse laser-induced breakdown spectroscopy (LIBS)", *Journal of Analytical Atomic Spectrometry*, Vol.29:1082, 2014.
4. Zhenzhen Wang, Yoshihiro Deguchi, Masakazu Kuwahara, Takuya Taira, Xiaobo Zhang, Junjie Yan, Jiping Liu, Hiroaki Watanabe, and Ryoichi Kurose: "Quantitative elemental detection of size-segregated particles using laser-induced breakdown spectroscopy", *Spectrochimica Acta Part B: Atomic Spectroscopy*, Vol.87: 130, 2013.
5. Zhenzhen Wang, Yoshihiro Deguchi, Masakazu Kuwahara, Xiaobo Zhang, Junjie Yan, and Jiping Liu: "Sensitive measurement of trace mercury using low pressure laser-induced plasma", *Japanese Journal of Applied Physics*, Vol.52: 11NC05, 2013.
6. Keqiang Chen, Jiping Liu, Xiaobo Zhang, Renwei Liu, Junjie Yan, Yoshihiro Deguchi. Numerical simulation on the laser induced oxygen spark under different ambient conditions[J]. *Applied Thermal Engineering*, 2014. (under review)

International Conferences:

1. Jiping Liu, Xiaobo Zhang, Junjie Yan and Zhijie Zhou: "Numerical simulation of one dimensional thermal acoustic wave induced by rapid heated wall with simple algorithm", 2nd Asian Symposium on Computational Heat Transfer and Fluid Flow, Jeju (Korea), October, 2009.
2. Xiaobo Zhang, Yoshihiro Deguchi, Masakazu Kuwahara and Jiping Liu: "Numerical simulation of laser induced plasma process using lattice Boltzmann method", 15th Asian Conference on Electrical Discharge, Xi'an (China), November, 2010.
3. Xiaobo Zhang, Yoshihiro Deguchi, and Jiping Liu: "Numerical simulation of laser induced weakly ionized Helium plasma process by lattice Boltzmann method", 3rd international symposium on advanced plasma science and its supplication for nitrides and nanomaterials, Nagoya (Japan), March, 2011.
4. Xiaobo Zhang, Yoshihiro Deguchi, Jiping Liu: "Simulation of Weakly Ionized Laser Gas

Plasma Generation Using Lattice Boltzmann Method", 3rd Asian Symposium on Computational Heat Transfer and Fluid Flow, Kyoto (Japan), September, 2011.

5. Xiaobo Zhang, Yoshihiro Deguchi, and Jiping Liu: "Simulation of H2 breakdown process produced by laser irradiation", 4th international symposium on advanced plasma science and its supplication for nitrides and nanomaterials, Nagoya (Japan), March, 2012.